Title

The mechanisms of plastic strain accommodation and post critical behavior of heterogeneous reactive composites subject to dynamic loading

Permalink

https://escholarship.org/uc/item/1d70w291

Author

Olney, Karl L.

Publication Date

2014

Peer reviewed|Thesis/dissertation

UNIVERSITY OF CALIFORNIA, SAN DIEGO

The mechanisms of plastic strain accommodation and post critical behavior of heterogeneous

reactive composites subject to dynamic loading

A dissertation submitted in partial satisfaction of the requirements for the degree Doctor of

Philosophy

in

Engineering Sciences with a specialization in Computational Science

by

Karl L. Olney

Committee in charge:

Professor Vitali F. Nesterenko, Co-Chair
Professor David J. Benson, Co-Chair
Professor Prabhakar Bandaru
Professor Farhat Beg
Professor Hyonny Kim

2014

This dissertation of Karl L. Olney is approved, and it is acceptable in quality and form for publication on microfilm and electronically:

_____

_____

_____

_____

Co-Chair

_____

Co-Chair

University of California, San Diego

2014

TABLE OF CONTENTS

LIST OF FIGURES

LIST OF TABLES

ACKNOWLEDGEMENTS

I would like to express my gratitude and appreciation to Professor Vitali Nesterenko and Professor David Benson for their guidance and understanding that has allowed me to grow as a student, researcher, and person during my time under their tutelage. I am also grateful to Professor Prabhakar Bandaru, Professor Farhat Beg, and Professor Hyonny Kim for serving on my committee.

I wish to thank my friends and family for their support and encouragement while pursuing my PhD. I would especially like to thank my parents for their support. Finally I would like to thank Diana Krivosheya for her continuous understanding, limitless patience, incredible

strength, and fiercely positive attitude that has encouraged and inspired me in all aspects of my

life.

VITA

2008	B.S., Mechanical Engineering, University of California, San Diego
2009-2014	Teaching Assistant, University of California, San Diego
2010	M.S., Mechanical Engineering, University of California, San Diego
2010-2013	Graduate student researcher, Los Alamos National Laboratory
2009-2014	Graduate student research assistant, University of California, San Diego
2014	Mechanical Engineer, Medtronic Inc., Santa Anna, California
2014	Ph.D., Engineering Sciences with a specialization in Computational Science, University of California, San Diego

REFEREED PUBLICATIONS

K.L. Olney, P.H. Chiu, C.W. Lee, V.F. Nesterenko and D.J. Benson, Role of material properties and mesostructure on dynamic deformation and shear instability in Al-W granular composites, Journal of Applied Physics, Volume 110, Page 114908 (2011).

K.L. Olney, V.F. Nesterenko, and D.J. Benson, Mechanisms of fragmentation of aluminum-tungsten granular composites under dynamic loading, Applied Physics Letters, Volume 100, Page 191910 (2012).

P.H. Chiu, K.L. Olney, A. Higgins, M. Serge, D.J. Benson, and V.F. Nesterenko, The mechanism of instability and localized reaction in the explosively driven collapse of thick walled Ni-Al laminate cylinders, Applied Physics Letters, Volume 102, Page 241912 (2013).

K.L. Olney, P.H. Chiu, A. Higgins, M. Serge, T. P. Weihs, G. M. Fritz, A. K. Stover, D.J. Benson, and V.F. Nesterenko, The mechanisms of plastic strain accommodation during the high strain rate collapse of corrugated Ni-Al laminate cylinders, Philosophical Magazine (In Press 2014).

K.L. Olney, C.J. Ruestes, J.F. Rodriguez Nieva, D.J. Benson, and E.M. Bringa, Finite element modeling of the high strain/strain-rate collapse of gold nanofoam using constitutive model parameters based on molecular dynamics simulations, (Submitted 2014).

K.L. Olney, P.H. Chiu, D.J. Benson, A. Higgins, M. Serge, and V.F. Nesterenko, Localized microjetting in the collapse of surface macrocavities, Phys. Rev. Letters (Submitted 2104).

CONFERENCE PAPERS

K.L. Olney, D.J. Benson, and V.F. Nesterenko, An overview of mesoscale material modeling with Eulerian hydrocodes, Journal of Physics: Conference Series, Volume 500, Page 152002 (2014).

K.L. Olney, P.H. Chiu, A. Higgins, M. Serge, T.P. Weihs, G. Fritz, A. Stover, D.J. Benson, and V.F. Nesterenko, Mechanisms of large strain, high strain rate plastic flow in the explosively driven collapse of Ni-Al laminate cylinders, Journal of Physics: Conference Series, Volume 500, Page 132002 (2014).

P.H. Chiu, K.L. Olney, C. Braithwaite, A. Jardine, A. Collins, D.J. Benson, and V.F. Nesterenko, Mechanisms of fragmentation and microstructure of debris generated during explosive testing of Al-W granular composite rings, Journal of Physics: Conference Series, Volume 500, Page 112017 (2014).

K.L. Olney, P.H. Chiu, V.F. Nesterenko, D.J. Benson, C. Braithwaite, A. Collins, D. Williamson, and F. McKenzie, The Fragmentation of Al-W Granular Composites under Explosive Loading, MRS Conference Proceedings, Volume 1521 (2012).

K.L. Olney, D.J. Benson, V.F. Nesterenko, Modeling shear instability and fracture in dynamically deformed Al/W granular composites, AIP Conference Proceedings, Volume 1426, Page 729 (2012).

V.F. Nesterenko, P.H. Chiu, C. Braithwaite, A. Collins, D. Williamson, K.L. Olney, D.J Benson,, and F. McKenzie, Dynamic Behavior of Particulate/Porous Energetic Materials, AIP Conference Proceedings 1426, Page 533 (2012).

ABSTRACT OF THE DISSERTATION

The mechanisms of plastic strain accommodation and post critical behavior of heterogeneous

reactive composites subject to dynamic loading

by

Karl L. Olney

Doctor of Philosophy in Engineering Sciences with a specialization in Computational Sciences

University of California, San Diego 2014

Professor Vitali F. Nesterenko, Co-Chair

Professor David J. Benson, Co-Chair

The dynamic behavior of granular/porous and laminate reactive materials is of interest due to their practical applications; reactive structural components, reactive fragments, etc. The mesostructural properties control meso- and macro-scale dynamic behavior of these heterogeneous composites including the behavior during the post-critical stage of deformation.

They heavily influence mechanisms of fragment generation and the *in situ* development of local hot spots, which act as sites of ignition in these materials.

This dissertation concentrates on understanding the mechanisms of plastic strain accommodation in two representative reactive material systems with different heterogeneous mesostructrues: Aluminum-Tungsten granular/porous and Nickel-Aluminum laminate composites.

The main focus is on the interpretation of results of the following dynamic experiments conducted at different strain and strain rates: drop weight tests, explosively expanded ring experiments, and explosively collapsed thick walled cylinder experiments. Due to the natural limitations in the evaluation of the mesoscale behavior of these materials experimentally and the large variation in the size scales between the mesostructural level and the sample, it is extremely difficult, if not impossible, to examine the mesoscale behavior *in situ*. Therefore, numerical simulations of the corresponding experiments are used as the main tool to explore material behavior at the mesoscale.

Numerical models were developed to elucidate the mechanisms of plastic strain accommodation and post critical behavior in these heterogeneous composites subjected to dynamic loading. These simulations were able to reproduce the qualitative and quantitative features that were observable in the experiments and provided insight into the evolution of the mechanisms of plastic strain accommodation and post critical behavior in these materials with complex mesotructure. Additionally, these simulations provided a framework to examine the influence of various mesoscale properties such as the bonding of interfaces, the role of material properties, and the influence of mesoscale geometry. The results of this research are helpful in the design of material mesotructures conducive to the desirable behavior under dynamic loading.

Chapter 1

Introduction

1.1 Motivation

The dynamic behavior of granular/porous [1-3] and laminate [4-9] reactive materials has attracted significant attention due to their possible practical applications: reactive structural components, reactive fragments, etc. The performance requirements introduce challenging fundamental problems such as combining high strength with ability to undergo controlled bulk disintegration producing small-sized reactive fragments unattainable for traditional materials.

The material structure that can meet this and other requirements should be tailored and optimized at the mesoscale to produce the desirable mechanical properties while still facilitating the release of chemical energy. Mesostructural parameters such as particle size and morphology can affect the strength and shock-sensitivity. This can be seen in pressed explosives [10, 11] and in reactive materials like Al-PTFE composites [12].

The ignition of a reactive material may be initiated via traditional methods, e.g. spark ignition or exposure to high temperatures from a flame. In some instances, these materials may be ignited due to the elevated temperatures associated with shock loading and post-shock dynamics [1-9]. Additionally, mesoscale features like force-chains in granular energetic materials may also serve as ignition sites [13-15]. It has also been observed that localized plastic flow of reactive materials may generate conditions suitable for the formation of "hot spots" which can lead to reaction [16-18]. In these cases, it is important to understand the mechanisms involved in the plastic deformation and how they relate to the generation of hot spots. Two reactive material

systems, Al-W granular mixtures and Ni-Al laminates, have been shown to be candidates as reactive material systems. These characteristic material systems will be used in this dissertation to examine the mechanisms of plastic strain accommodation during dynamic loading related to the formation of these "hot spots".

In the case of Al granular mixtures the goal is to have the Al oxidize with the free oxygen in air resulting in an exothermic reaction. Despite the large combustion energy (7422 cal/g) to attain achieve oxidization on a timescale of approximately 1 millisecond (appropriate for blast loading events in munitions), Al needs to be pulverized into particles with sizes less than 20 μm [19]. The size scale (S) of the fragmentation of homogeneous materials may be characterized by the Grady-Kipp [20] criteria

$$S = \left(\frac{24\Gamma}{\rho\dot{\varepsilon}^2}\right)^{1/3} \tag{1.1}$$

where Γ is the fragmentation energy, ρ is the material density, and $\dot{\varepsilon}$ is the strain rate. For the case of Al 6061-T6 alloy (K_c= 33MPa/m1/2, E= 70 GPa, $\Gamma = K_c/2E$ = 8000 J/m2) and at strain rates typical for dynamic processes of interest (104 s-1), the typical fragment size is approximately 9mm. A possible method for reducing this size scale, which is the objective for the Al-W granular mixtures examined in this dissertation, is to create a heterogeneous mesostructure that assists in reduction of fragmentation size scales. Tungsten has been identified for two main reasons. First is that it has a large strength and may be used to assist in the structural integrity of the material system. Second is that the W is significantly denser then the Al (density W = 19.25 g/cc, density Al = 2.7 g/cc) which results in a significantly different shock impedance (i.e. ability to be moved by a shock wave), meaning that if a shock were to pass through a heterogeneous material of Al and W, then it is possible that velocity gradients would form and fragments may be generated on the size scale of the spacing of the W components.

In the case of Ni-Al laminates, the intermetallic reaction between Al and Ni is exothermic and shown to be self-sustaining [21-25]. It has been shown that these materials are able to react under shock loading [4-9] for mesostructures with nanometer sized layers. It has not been studied however, if mechanical loading, e.g. pure shear, can generate conditions such as shear banding to generate hot spots in cases where the layers of the laminate have layer thicknesses on the order of micrometers.

1.2 Bridging simulations with experiments

In the reactive materials of interest, there are two initial main size scales of importance; the global sample size (~1-10cm) and the size of the mesostructural features (~1-500 μm). Additional multiple size scales (i.e. thickness of shear bands, spacing between them, scale of microcracks patterning, size of fragments, etc.) can be generated *in situ*. Since the purpose of this research is to examine the dynamic response of these materials, the time scales associated with the experiments are very short (on the order of 10 μs to 100 ms). To complicate matters, many of these experiments are explosively driven and some are in a closed experimental apparatus. These complexities hinder the ability to capture the evolution of the mesostructures during these experiments as current high speed cameras do not have the required resolution to capture the material behavior at the required size and time scales. The best *in situ* data we can obtain is either general global properties of the process (e.g. free surface velocity of explosively expanded ring), or we have to rely on the pre- and post-experiment imaging and attempt to interpret the results.

As such, numerical simulations of these experiments are developed to probe the evolution of the mesoscale mechanisms of plastic strain accommodation. The Finite Element Method (FEM) was selected as the numerical method to perform these simulations as it has been shown to provide solutions to problems involving extremely complex geometries and complex loading condition where analytical solutions are not available.

1.3 Modeling of heterogeneous materials

There are two main strategies for modeling heterogeneous materials; a homogenization approach or a discrete modeling approach where each component is modelled separately. Homogenization approaches make an assumption that, at the scale of interest, the heterogeneity of the sample is at a much smaller scale and therefore can be represented using a single set of bulk properties. This approach generally gives good results when the sample is subjected to small strains or when the sample remains undamaged. However, this approach generally breaks down when the sample is subjected to large strains where plasticity and fracture is involved as this methodology does not provide the detail needed to distinguish between materials at the component level. In these situations where the behavior of the mesoscale dominates the material response, discretely modeling the components is advantageous. However, in many circumstances where the size scales of the mesoscale and the global sample vary by many orders of magnitudes. As such, the use of a representative element is generally used as modeling the entire sample is not possible with current computational capabilities.

The size scale of the mesoscale components associated with the Al-W and Ni-Al heterogeneous materials examined in this dissertation are of the order of tens to hundreds of micrometers while the global samples are generally in the ones to tens of centimeters. Additionally, the focus of this research is on the behavior of these materials when they are subjected to large global strains that induce localized plastic strains and generate complex behavior of these materials on the post critical stage of their deformation. Therefore, the simulations conducted for this dissertation all utilize the representative element approach.

1.4 Objectives

The work performed for this dissertation utilizes numerical simulations in conjunction with experiments to elucidate the mechanisms of plastic strain accommodation and fragmentation

in granular/porous Al-W and Al-Ni laminate reactive material systems. Chapter 2 provides a background on the details of the three experimental setups where the dynamic experiments on the heterogeneous materials were conducted. Chapter 3 provides a brief overview and background of the numerical tools to model these problems. Chapter 4 examines the results of the experiments and simulations related to the drop weight tests to examine the post-critical material response of Al-W granular/porous materials. Chapter 5 examines the experimental and simulation results of the explosively loaded Al-W granular rings. Chapter 6 uses simulations to examine the effects of loading on the various mechanisms of fragmentation in explosively loaded Al-W rings. Chapter 7 and 8 examine the results from the Thick Walled Cylinder (TWC) tests and simulations of the Al-Ni laminates. Finally, Chapter 9 will provide the summary and conclusions of the research.

1.5 Chapter references

[1] R. Ames, Multi-functional Energetic Materials, *MRS Proc*. **896**, 123 (2006).

[2] J. J. Davis, A. J. Lindfors, P. J. Miller, S. Finnegan, and D. L. Woody, *11th Det. Symp. (Int.)* 1007 (1998).

[3] W. Holt, W. Mock, Jr., and F. Santiago, *J. Appl. Phys*. **88**, 5485 (2000).

[4] N. N. Thadhani, *Prog. Mat. Sci.* **37**, 117 (1993).

[5] I. Song and N. N. Thadhani, *Metall. Trans*. A **23**, 41 (1992).

[6] D. Eakins and N. N. Thadhani, *J. Appl. Phys*. **101**,043508 (2007).

[7] Y. Horie, R. A. Graham, and I. K. Simonsen, *Mater. Lett*. **3**, 354 (1985).

[8] I. K. Simonsen, Y. Horie, R. A. Graham, and M. Carr, *Mater. Lett*. **5**, 75 (1987).

[9] F. X. Jette, A. J. Higgins, S. Goroshin, D. L. Frost, Y. Charron-Tousignant, M. I. Radulescu, and J. J. Lee, *J. Appl. Phys*. **109**, 084905 (2011).

[10] C. R. Siviour, M. J. Gifford, S. M. Walley, W. G. Proud, and J. E. Field, *J. Mater. Sci.* **39**, 1255 (2004).

[11] J. E. Balzer, C. .R Siviour, S. M. Walley, W. G. Proud, and J. E. Field, *Proc. R. Soc. London* **781**, 460 (2004).

[12] J. W. Mock and J. Drotar, *AIP Conf. Proc*. **955**, 871 (2007).

[13] J.C. Foster Jr., J. Glenn, and M. Gunger, *AIP Conf. Proc*. **505**, 703 (2000).

[14] S. Bardenhagen and J. Brackbill, *J. of Appl. Phys*. **83**, 5732 (1998).

[15] K. Roessig, J. J.C. Foster, and S. Bardenhagen, *Exp. Mech*. **42**, 329 (2002).

[16] V.F. Nesterenko, M.A. Meyers, H.C. Chen and J.C. Lasalvia, *Appl. Phys. Lett.* **65**, 3069 (1994).

[17] V.F. Nesterenko, M.A. Meyers, H.C. Chen and J.C. Lasalvia, *Metall. Mater. Trans. A* **26**, 2511 (1995).

[18] H.C. Chen, V.F. Nesterenko, and M.A. Meyers, *J. Appl. Phys.* **84**, 3098 (1998).

[19] M.W. Beckstead, *Comb. Exp. and Shock Waves*, **41**, 533 (2005).

[20] D.E. Grady, *Fragmentation of Rings and Shells: The Legacy of N.F. Mott*. Springer, New York (2007).

[21] E. Ma, C. V. Thompson, and L. A. Clevenger, *J. Appl. Phys*. **69**, 2211 (1991).

[22] K. Barmak, C. Michaelsen, and G. Lucadamo, *J. Mater. Res*. **12**, 133 (1997).

[23] L. Battezzati, P. Pappalepore, F. Durbiano, and I. Gallino, *Acta Mater*. **47**, 1901 (1999).

[24] J. Wang, E. Besnoin, A. Duckham, S. J. Spey, M. E. Reiss, O. M. Knio, M. Powers, M. Whitener, and T. P. Weihs, *Appl. Phys. Lett*. **83**, 3987 (2003).

[25] J. Wang, E. Besnoin, O. M. Knio, and T. P. Weihs, *J. Appl. Phys*. **97**, 114307 (2005).

Chapter 2

Experimental techniques

The experimental results numerically analyzed in this dissertation were conducted in a one of three experimental setups; drop weight tests with large global sample deformation with acquired data using strain gauges and high speed camera, explosively driven fragmentation of expanded rings examined using PDV technique, and the Thick Walled Cylinder method (TWC) with controlled detonation speed and analysis of post critical features like shear banding and fragmentation. This chapter outlines set ups of these three testing methods. It provides an insight how these tests were used to gain understanding of the dynamic response of materials and help elucidate the mechanism of accommodation of high strain rate, large plastic strains.

2.1 Drop weight tests

The drop weight tests modeled in this dissertation were all conducted using a high velocity DYNATUP model 9250HV with an in-house modified anvil for sample support. A photograph of the experimental setup is presented in Figure 2.1. The drop weight can be adjusted from 2.7 kg to 28.9 kg and the maximum free fall height of drop tower is 1.25m. To perform a drop weight test on a sample of interest, the sample is first placed on the anvil. The drop weight is then lifted to a desired height. In some instances, a spring can be used to increase the nominal velocity of impact above the nominal drop velocity to a maximum of 20 m/s. High speed cameras are used in conjunction with accelerometers on dropped weight and strain gauges on the bottom of the sample to gather strain, strain rate, and stress information. Scanning electron microscopy

(SEM) is utilized to view the mesostructure of the pre- and post-experiment samples. Stoppers may be used to directly control the maximum strain in the sample. The strain rates involved in this test $O(10^2 - 10^3 \text{ s}^{-1})$ are comparable to the strain rates in Hopkinson-bar experiments [1], however, unlike the Hopkinson-bar test, these experiments allow for the examination of the post critical behavior of the material at some controlled conditions as the deformation is not limited by a short duration of the loading pulse as in Hopkinson bar and it does not stop once the first shear band or crack appears.

In the context of this dissertation, these experiments provided a framework that was used to examine the large strain deformation (0.50 sample strain and above) of Al-W granular materials at strain rates of $O(10^2 - 10^3 \text{ s}^{-1})$ to examine the influence of mesostructural properties on the mechanisms of plastic deformation and post critical material response under these conditions.
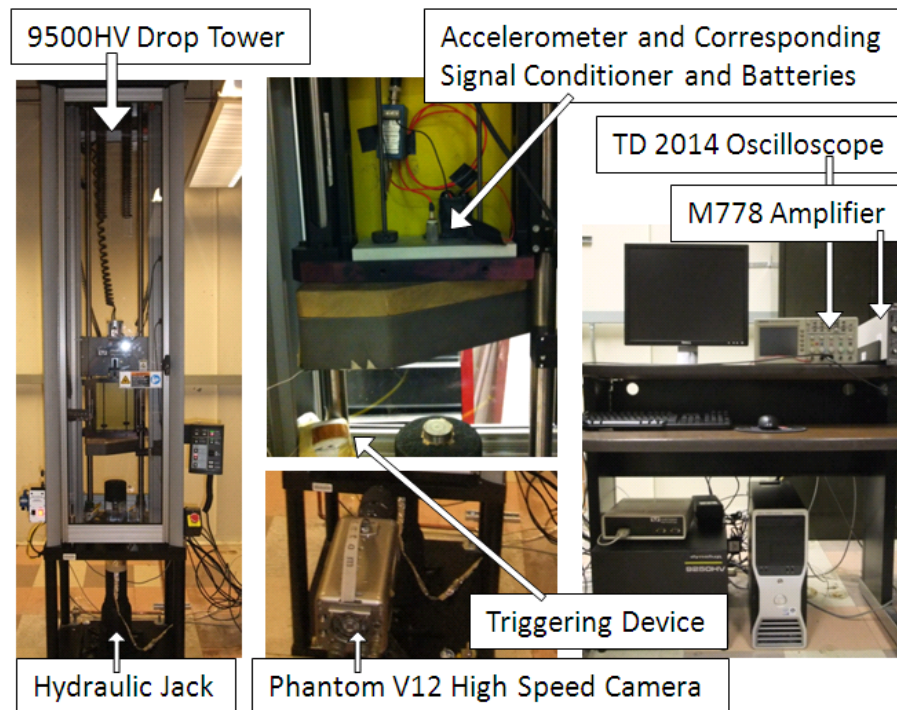
Figure 2.1 - The DYNATUP model 9250HV with the in-house modified anvil used in the drop weight tests. [2]

2.2 Explosively expanded rings

This class of experiments is commonly used to study the high strain rate behavior (10^3-10^4 s^{-1}) of materials. In this experimental setup, samples are formed into a ring or tube which is placed around a copper driver tube. Explosive material is placed inside this copper tube and detonated. A schematic of the experimental setup is presented in Figure 2.2. Photon Doppler Velocimetry (PDV) is used to examine the free surface velocity of a spot of the expanding sample. Figure 2.3 (a) presents an example PDV trace of an explosively expanded ring. In addition to the PDV records, a high speed camera is utilized to view the fragmentation process (see Figure 2.3 (b)). However, it is clear from the high speed video images that it is impossible to see the mesoscale material response. The experiment was performed in a stainless steel blast

chamber coated with wax. This wax acted as a "soft catch" barrier to ensure that additional fragmentation did not occur on impact [3-5]. After the experiments, the fragments were collected by melting the wax and sifting through various sized filters such that only the fragments remained [3-5]. These fragments could then be analyzed using laser diffraction to obtain the fragment size distributions [5].

In the context of this dissertation, these experiments were conducted on Al-W (granular/porous, granular/wires, and solid/granular) composites to examine the high strain-rate behavior resulting in the pulverization of the sample. Specifically, the mechanisms of fragmentation of these composites at strain rates on the order 10^3-10^4 s^{-1}.
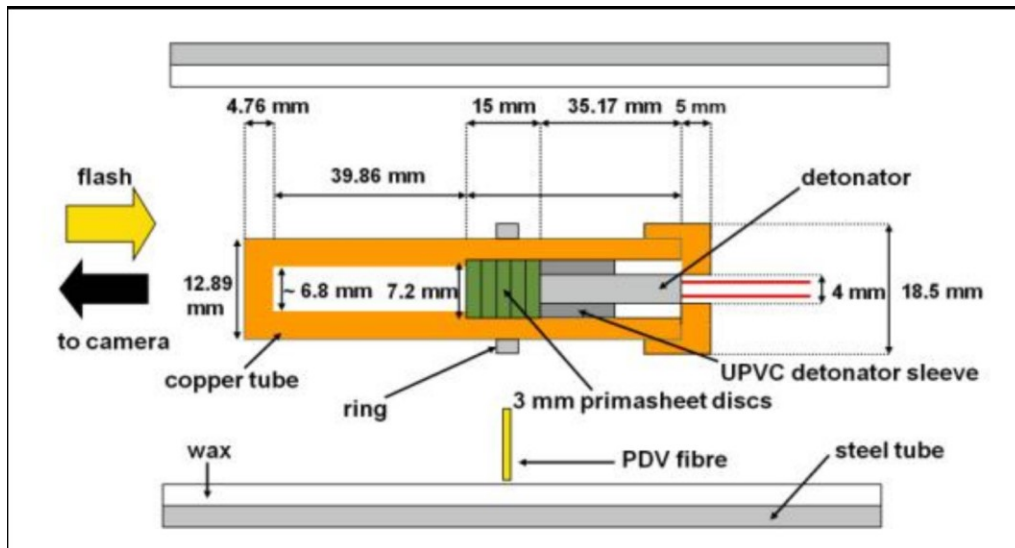
Figure 2.2 - Experimental setup of the explosively expanding ring setup. Testing was conducted in Cavendish Labs in Cambridge, UK.
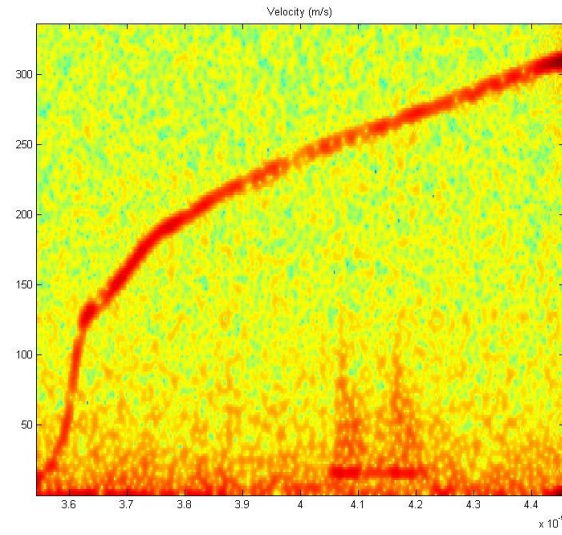
(a)
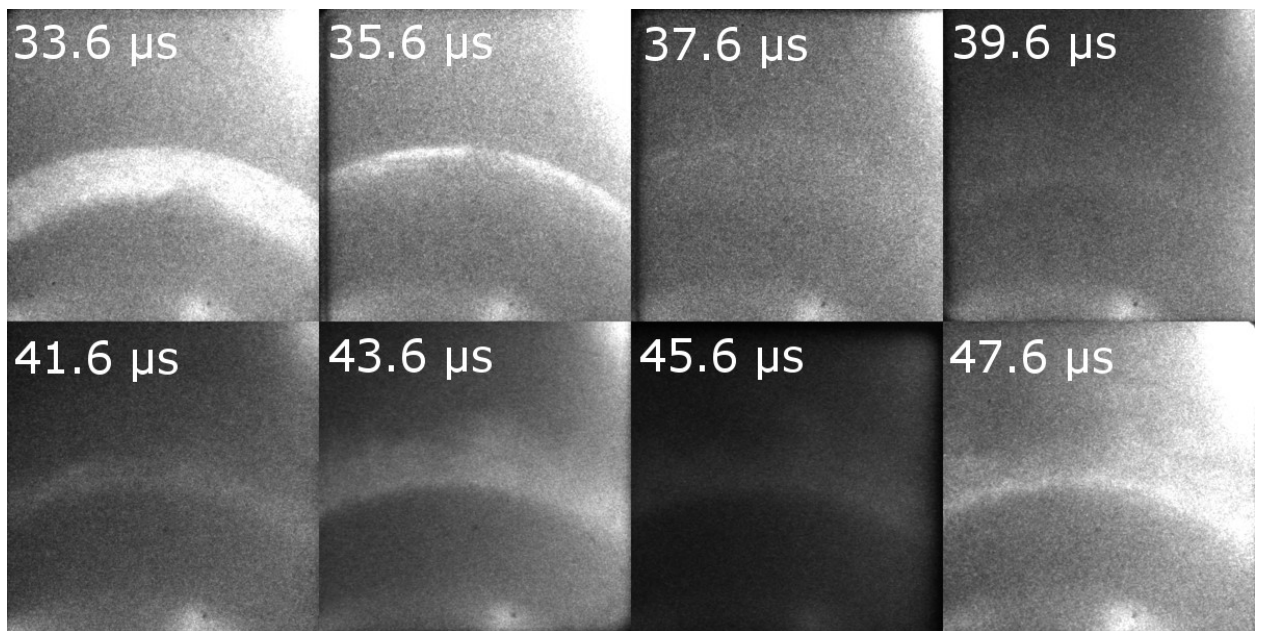
(b)

Figure 2.3 – An example PDV trace of an explosively expanded ring (a) and the corresponding high speed image captures (b).

2.3 The Thick Walled Cylinder method

The Thick Walled Cylinder (TWC) method was developed to study the large strain, high strain rate effects in plane strain conditions [6]. The collapse of the TWC can be driven either by explosive [6] or magnetic [7, 8] loading. In this work, a modified nitromethane explosive [9] were used to drive the collapse. A photograph and a schematic of the experimental setup are presented in Figure 2.4 [9]. The TWC assembly is composed of 4 main components: the top and bottom steel plugs, the copper stopper tube, the copper driver tube, and the sample with steel inserts on the bottom and the top. The plugs have grooves allowing for the self-sealing of the assembly preventing detonation products from interacting with the sample and encapsulating the sample for post mortem analysis. The inner copper "stopper" tube is used to control the final strain of the sample. The outer copper "drive" tube is significantly thicker then all of the other components in the system and therefore determines the kinetics and symmetry of the collapse process. Tuning the explosive driver allows variations of strain rates.

All previously investigated materials in the thick-walled cylindrical geometry: solid monocrystalline and polycrystalline metals; polymers [6, 10-13]; solid and granular ceramics (SiC and Al_2O_3) [14-16]; and reactive granular materials [17-19], accommodate the high strain/strain-rate global plane strain deformation by developing self-organized patterns of multiple shear bands. In some cases, these shear bands can number in the hundreds as in SS T-304L [13]. The mechanisms of plastic flow instability triggering the spontaneous shear localization and subsequent pattern of shear bands are different for various classes of materials. For example, in solid homogeneous metals, the thermal softening triggers the shear instability at a very modest increase in the uniform temperature caused by plastic deformation (~30 K) [13]. In the case of granular materials, it is microfracture of grains due to the high stresses localized at the contact interfaces [14-16]. In the context of this dissertation, the TWC method is used to examine

the mechanisms of plastic strain accommodation of Ni-Al laminate materials in strain rates of 10^3-10^4 s^{-1}.
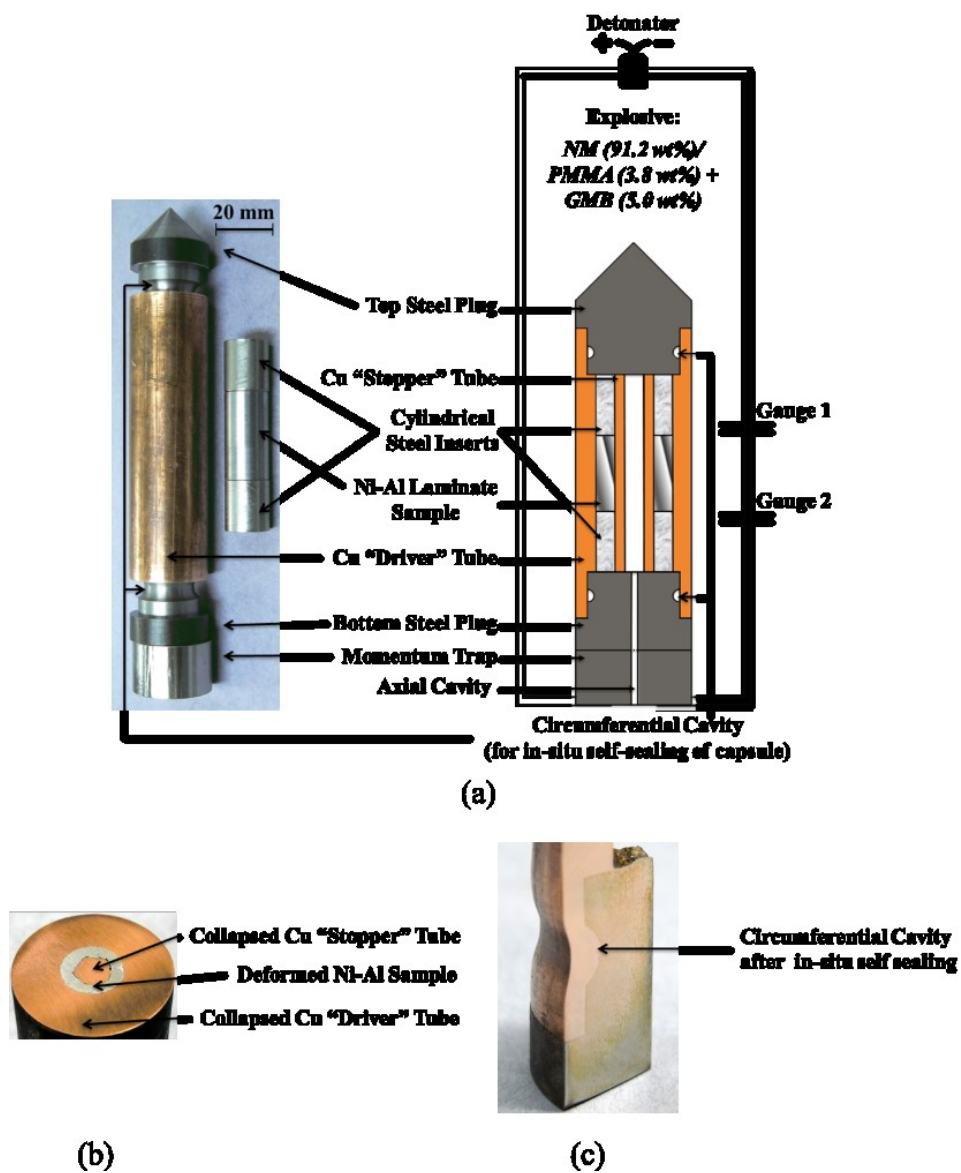
Figure 2.4 - Experimental setup for the Thick Walled Cylinder (TWC) method (a) and an example of the collapsed sample (b) and self-sealing mechanism (c) [9].

2.4 Chapter references

[1] B. Hopkinson, Philos. Trans. R. Soc. (London) A, 213, 437 (1914).

[2] K.L. Olney, P.-H. Chiu, C.-W. Lee, V.F. Nesterenko, and D.J. Benson, J. Appl. Phys. 110, 114908 (2011).

[3] V.F. Nesterenko, P.H. Chiu, C. Braithwaite, A. Collins, D. Williamson, K.L. Olney, D.J Benson,, and F. McKenzie, AIP Conf. Proc. 1426, 533 (2012).

[4] K.L. Olney, P.H. Chiu, V.F. Nesterenko, D.J. Benson, C. Braithwaite, A. Collins, D. Williamson, and F. McKenzie, MRS Conf. Proc., 1521 (2012).

[5] P.-H. Chiu, K.L. Olney, C. Braithwaite, A. Jardine, A. Collins, D.J. Benson and V.F. Nesterenko, J. Phys.: Conf. Ser. 500, 112017 (2014)

[6] V.F. Nesterenko, Dynamics of Heterogeneous Materials (Springer, New York, 2001) p.307.

[7] J.L. Stokes, V.F. Nesterenko, J.S. Shlachter, R.D. Fulton, S.S. Indrakanti, and Ya Bei Gu, in Proceedings of International Conference on Fundamental Issues and Applications of Shock-Wave and High-Strain-Rate Phenomena, edited by K.P. Staudhammer, L.E. Murr, and M.A. Meyers, (2001, Elsevier, Amsterdam, 2011), pp. 585-592.

[8] Z. Lovinger, A. Rikanati, Z. Rosenberg, and D. Rittel, Int. J. Impact Eng. 38, 918 (2011).

[9] P.H. Chiu, K.L. Olney, A. Higgins, M. Sege, D.J. Benson and V.F. Nesterenko, Appl. Phys. Lett. 102, 241912 (2013).

[10] Y. J. Chen, M. A. Meyers, and V. F. Nesterenko, Mat. Sci. Eng. A-Struct. 268, 70 (1999).

[11] V. F. Nesterenko, M. A. Meyers, and T. W. Wright, Acta Mater 46, 327 (1998).

[12] M. A. Meyers, V. F. Nesterenko, J. C. LaSalvia, and Q. Xue, Mat. Sci. Eng. A-Struct. 317, 204 (2001).

[13] Q. Xue, V. F. Nesterenko, and M. A. Meyers, Int. J. Impact Eng. 28, 257 (2003).

[14] C. J. Shih, V. F. Nesterenko, and M. A. Meyers, J. Appl. Phys. 83, 4660 (1998).

[15] C. J. Shih, M. A. Meyers, and V. F. Nesterenko, Acta. Mater. 46, 4037 (1998).

[16] V. F. Nesterenko, M. A. Meyers, and H. C. Chen, Acta. Mater. 44, 2017 (1996).

[17] V. F. Nesterenko, M. A. Meyers, H. C. Chen, and J. C. Lasalvia, Appl. Phys. Lett. 65, 3069 (1994).

[18] V. F. Nesterenko, M. A. Meyers, H. C. Chen, and J. C. Lasalvia, Metall. Mater. Trans. A 26, 2511 (1995).

Chapter 3

Background on the Finite element method

This section provides a brief overview of the Finite Element Analysis (FEA) numerical method that used to conduct the simulations performed in this dissertation. First a general overview of the FEA framework for explicit dynamic continuum mechanics problems will be presented. Second, a brief discussion of the material/constitutive models that were used for this work will be presented. Finally, the Multi-Material Eulerian finite element method will be discussed.

3.1 A brief overview of the finite element method for explicit dynamic continuum mechanics problems

Determining and solving analytical solutions of boundary value problems (such as structural/continuum mechanics problems) for complex geometries on domains of interest can be very difficult. Finite Element Analysis (FEA) is a numerical method in which the complex geometrical domain is discretized into a set of smaller, simple shapes (elements). The collection of elements that discretize the domain is referred to as the mesh. The discretization scheme used in FEA assumes that the solution in a single element is only influenced by the nodes defining the element.

For problems involving the deformation of materials, the governing equation of interest is

$$\sigma_{ij,j} + \rho f_i = \rho \ddot{x}_i \qquad (3.1)$$

with traction boundary conditions of boundary b_1 defined by

$$\sigma_{ij} n_j = T_i(t) \qquad (3.2)$$

and the displacement boundary conditions of boundary b_2 defined by

$$x_i(x_0, t) = u_i(t) \qquad (3.3)$$

where σ is the Cauchy stress, ρ is the current density, f is the body force, $\ddot{x}$ is the acceleration, n is the unit outward normal direction, $T(t)$ is the time dependent traction, x_0 is the initial coordinate, and $u(t)$ is the time dependent displacement. The principle of virtual work is utilized and the governing equation becomes

$$\delta U = \int_v \rho \ddot{x}_i \delta x_i dv + \int_v \sigma_{ij} \delta x_{i,j} dv + \int_v \rho f_i \delta x_i dv$$

$$+ \int_{b_1} T_i \delta x_i ds = 0 \qquad (3.4)$$

where δU is the virtual work, δx_i is the variations of x. When applied to the finite element framework, these equations are discretized for each element and assembled into a global formulation. These assembled sets of elemental equations take the form

$$\sum_{k=1}^{nelements} \left\{ \int_{v_k} \rho N_k^T N_k \ddot{x} dv + \int_{v_k} B_k^T \sigma dv - \int_{v_k} \rho N_k^T f dv \right.$$

$$\left. - \int_{b_1} N_k^T T ds \right\} = 0 \qquad (3.5)$$

where **N** is the interpolation matrix and **B** is the strain-displacement matrix, both of which are dependent on the type of element formulation used. It should be noted that σ is the vector of stresses in Voigt notation. The first integral of Eqn. (3.5) forms the "mass matrix" and, in general,

is simplified via row summing to generate a diagonal matrix. Additionally, the evaluations of the interpolation functions are calculated in an isoparametric domain and integrated using Gaussian quadrature.

3.2 Material / constitutive modeling

The relationship between the stress ($\boldsymbol{\sigma}$) and the field variables (i.e. strain, strain rates, temperature, etc.) is referred to as the constitutive model. In situations where materials undergo small deformations (i.e. in the elastic regime of the material behavior), a simple linear elastic constitutive model (based on Hooke's Law) can describe the resulting stresses generated due to deformation with the following form,

$$\boldsymbol{\sigma}(\boldsymbol{\varepsilon}) = E \cdot \boldsymbol{\varepsilon} \tag{3.6}$$

where E is the Young's modulus. However, in situations where the material undergoes plastic deformation, this simple model does not capture the inelastic portion of the loading and a more complex constitutive model is required.

Ductile isotropic metals may be modeled using a Von Mises plasticity theory. This theory states that the yield stress (σ_y) is related to the second deviatoric stress invariant (J_2) through the relation

$$\sigma_y = \sqrt{3J_2} = \sqrt{\frac{3}{2}\sigma'_{ij}\sigma'_{ij}} \tag{3.7}$$

where σ'_{ij} is the deviatoric stress tensor. The deviatoric stress originates from the the full stress tensor which can be split into the hydrostatic and deviatoric tensors by

$$\sigma_{ij} = \sigma'_{ij} + \frac{\sigma_{kk}}{3}\delta_{ij} = \sigma'_{ij} - P\delta_{ij} \tag{3.8}$$

where σ_{ij} is the Cauchy stress tensor, δ_{ij} is the Kroniker delta function, and P is the pressure. The hydrostatic, or pressure, portion of the stress tensor can be obtained using and equation of state. A popular method for integrating these plasticity equations is using the Radial Return algorithm [1, 2]. The following sections will describe the constitutive models that were used in the modeling performed for this dissertation.

3.2.1 The Johnson-Cook plasticity model

The Johnson-Cook plasticity model [3] was developed to model the behavior of isotropic ductile metals. The model is empirically based and the material parameters are readily available for a large selection of metals in the literature. This constitutive model was selected for the work conducted in this dissertation due to its ability to capture the influence of strain hardening, strain rate, and temperature on material behavior. In addition, the Johnson-Cook model is able to capture the failing of material through a damage evolution model [4]. The model is based on J2 plasticity theory and the implementation in LS-DYNA [5] utilizes the radial return algorithm [1, 2] to integrate the plasticity equations. The yield strength of this constitutive model has the form

$$\sigma_y = \left(A + B\bar{\varepsilon}_p^n\right)\left(1 + C\ln\frac{\dot{\varepsilon}}{\dot{\varepsilon}_0}\right)\left(1 + \frac{T - T_{room}}{T_{melt} - T_{room}}\right) \tag{3.9}$$

where $\bar{\varepsilon}_p$ is the effective plastic strain, $\dot{\varepsilon}$ is the strain rate, $\dot{\varepsilon}_0$ is the strain rate at which rate effects become important, T_{melt} and T_{room} are the melt and room temperatures respectively. The constants A, B, n, C, and m are the material parameters obtained from experimental data. To account for the material failure, the Johnson-Cook constitutive model tracks the damage evolution in the element and scales the yield stress. This damage model scales the yield stress as

$$\sigma_y = \sigma_y(1 - D) \tag{3.10}$$

where the damage (D) is defined as

$$D = \sum \frac{\Delta \bar{\varepsilon}_p}{\varepsilon_f} \tag{3.11}$$

with the failure strain (ε_f) defined as

$$\varepsilon_f = \left(D_1 + D_2 \exp\left(D_3 \frac{P}{\sigma_{vms}}\right)\right)\left(1 + D_4 \ln \frac{\dot{\varepsilon}}{\dot{\varepsilon}_0}\right)\left(1 + D_5 \frac{T - T_{room}}{T_{melt} - T_{room}}\right) \tag{3.12}$$

where σ_{vms} is the von mises stress, and D_1-D_5 are the damage parameters obtained via experiments. It should be noted that these parameters are usually obtained by fracturing materials in pure tension or under pure torsion [4].

3.2.2 The Mie-Grünieson equation of state

As mentioned in in Section 3.2, an equation of state is used to calculate the hydrostatic response of the material. The Mie-Grüneison equation of state was developed to examine the behavior or materials under shock loading [6], and has a general form of

$$P = C_1 + C_2 E \tag{3.13}$$

For the work performed in this dissertation, the form of the Mie-Grunieson equation of state used two separate forms; in compression the equation of state takes the form,

$$P = \frac{\rho_0 C^2 \mu \left[1 + \left(1 - \frac{\gamma_0}{2}\right)\mu - \frac{a}{2}\mu^2\right]}{\left[1 - (S_1 - 1)\mu - S_1 \frac{\mu^2}{\mu + 1} - S_3 \frac{\mu^3}{(\mu + 1)^2}\right]^2} + (\gamma_0 + a\mu)E \tag{3.14}$$

and in tension it takes the form

$$P = \rho_0 C^2 \mu + (\gamma_0 + a\mu)E \tag{3.15}$$

where ρ_0 is the density of the unloaded material, C is the sound speed in the material, S_1-S_3 are constants that fit the particle velocity vs shock velocity (u_s-u_p) relations of the material, γ_0 is the Grunieson parameter, a is the linear volume correction factor, and μ is the compression ratio defined by

$$\mu = \frac{\rho}{\rho_0} - 1. \qquad (3.16)$$

3.2.3 Material models for explosives

Some of the tests examined in this dissertation involved the use of explosives to drive the dynamic collapse/expansion of the test samples. In all of these cases, the main goal of the explosive driver is to act solely as a driver and the details of the explosion were not the focus of the research. As such, the microscopic details of explosive are of little importance, i.e. heterogeneities, defects, localized phenomena, detonation details, etc. When simulating these explosives, two different material models were used, selected based on the availability of the material parameters. In all cases, it was assumed that the explosives and the detonation products did not have any shear strength and therefore the material response behavior is dependent only on the pressure.

3.2.3.1 Modeling the detonation products as a gamma law gas

In cases where the diameter or thickness of explosive charge is close to critical size, i.e. near the size/thickness where detonation will not propagate, then it may be assumed that during an explosive event, the detonation products exist at the Chapmann-Jourget (C-J) point [7, 8]. Furthermore, if it is assume that the detonation event occurs simultaneously in the entire charge, then the explosive may be modeled as its detonation products and behaves according to the gamma law gas

$$P = (\gamma - 1)\frac{\rho}{\rho_0}E \tag{3.17}$$

where γ is the ratio of the specific heats c_p/c_v, ρ is the density, $\rho0$ is the initial density, and E is the internal energy. At the C-J point the initial parameters for γ, ρ_0, and E_0 can be found using the C-J relations

$$\gamma = \gamma_{CJ} = \frac{\rho_{exp}D^2}{P_{CJ}} - 1 \tag{3.18}$$

$$\rho_0 = \rho_{CJ} = \rho_{exp}\frac{\gamma_{CJ} + 1}{\gamma_{CJ}} \tag{3.19}$$

$$E_0 = \frac{P_{CJ}}{\rho_{CJ}(\gamma_{CJ}-1)}. \tag{3.20}$$

3.2.3.2 The Jones-Wilkins-Lee (JWL) equation of state

The Jones-Wilkins-Lee (JWL) equation of state [9] is an empirical equation of state mainly used to model the pressure response of detonation products of explosive materials as a function of the relative volume, V, and the internal energy per initial volume, E. This equation of state has the form

$$P = A\left(1 - \frac{\omega}{R_1V}\right)e^{-R_1V} + B\left(1 - \frac{\omega}{R_2V}\right)e^{-R_2V} + \frac{\omega E}{V} \tag{3.21}$$

where A, B, ω, R_1, and R_2 are material parameters.

3.3 Contact

In the work performed in this dissertation, the simulations involve many different materials interacting with each other. In many of these cases, the different materials are composed of different meshes and in many instances; it is possible for the exterior elements of a single mesh

may come into contact with itself. To account for these possibilities, contact between different meshes and a self-contact algorithm are utilized.

There are a variety of methods that have been developed to simulate the contact and interaction of two or more elements/meshes that do not share the same nodes. These methods mainly fall under one of two main categories; Lagrange multiplier method (constraint based) or penalty methods. For problems involving explicit simulations with slip and separation of the interfaces, the penalty methods are favorable.

One surface is designated the master surface and the other, the slave surface. As the solution advances, if a slave node crosses the master interface a force normal to the penetration direction is applied to the slave node and the master surface nodes. The contact force due to the penalty method is analogous to the force generated by a spring

$$F_{penalty} = k\delta \tag{3.21}$$

where δ is the penetration depth and the value of k is the stiffness factor which is defined for solid elements as

$$k = \frac{f_{sf}KA^2}{V} \tag{3.22}$$

and for shell elements as

$$k = \frac{f_{sf}KA}{\max(diagonal)} \tag{3.23}$$

where K is the bulk modulus, f_{sf} is a scale factor for the interface stiffness, V is the volume , and A is the area of the contact face in solid elements and the element area for shell elements.

To handle the contact of interfaces belonging to the same mesh, a single-surface algorithm is used [10]. This algorithm breaks the global domain into "buckets" and assumes that any free surface in the same or adjacent buckets may be potential contact interfaces. Friction

between interfaces is handled via the contact algorithm based on a Coulomb friction formulation [11].

3.4 Brief overview of the Multi-Material Eulerian finite element methods

When modeling problems where materials undergo very large plastic deformation or fragmentation, numerical instabilities and degradation of the solution quality may arise as the mesh becomes highly distorted or in the case of fragmentation, removed/eroded from the simulation. Many methods have been developed to model situations where these problems occur. These methods include, smooth particle hydrodynamics (SPH) [12, 13], automatic remeshing/rezoning, mesh free methods [14], and Multi-material Arbitrary Lagrangian Eulerian Finite Element method (MMALE) [15]. The MMALE method was selected as it has shown to provide good results in problems similar to the work performed in this dissertation [16]. This provides a brief overview of this method, a more detailed presentation of the theory used in the MMALE methods can be found in [15].

The MMALE methods are characterized by a background mesh in which each element contains one or more materials defined by the volume fractions. Each time step is broken into two sub-steps, the Lagrangian step and the Eulierain step. The conservation equations for mass, momentum, and energy

$$\frac{\partial \rho}{\partial t} + \nabla \cdot (\rho \boldsymbol{u}) = 0 \tag{3.24}$$

$$\frac{\partial \rho \boldsymbol{u}}{\partial t} + \nabla \cdot (\rho \boldsymbol{u} \otimes \boldsymbol{u}) = \nabla \cdot \boldsymbol{\sigma} + \rho \mathbf{b} \tag{3.25}$$

$$\frac{\partial \rho e}{\partial t} + \nabla \cdot (\rho e \boldsymbol{u}) = \boldsymbol{\sigma} : \dot{\boldsymbol{\varepsilon}} + \rho \mathbf{b} \cdot \boldsymbol{u} \tag{3.26}$$

are split amongst the two steps via operator splitting. The resulting conservation equations take the form

$$\frac{\partial \rho}{\partial t} = 0 \tag{3.27}$$

$$\frac{\partial \rho \boldsymbol{u}}{\partial t} = \nabla \cdot \boldsymbol{\sigma} + \rho \mathbf{b} \tag{3.28}$$

$$\frac{\partial \rho e}{\partial t} = \boldsymbol{\sigma} : \dot{\boldsymbol{\varepsilon}} + \rho \mathbf{b} \cdot \boldsymbol{u} \tag{3.29}$$

for the Lagrangian step and

$$\frac{\partial \rho}{\partial t} + \nabla \cdot (\rho \boldsymbol{u}) = 0 \tag{3.30}$$

$$\frac{\partial \rho \boldsymbol{u}}{\partial t} + \nabla \cdot (\rho \boldsymbol{u} \otimes \boldsymbol{u}) = 0 \tag{3.31}$$

$$\frac{\partial \rho e}{\partial t} + \nabla \cdot (\rho e \boldsymbol{u}) = 0 \tag{3.32}$$

for the Eulerian step. During the Lagrangian step, the solution variables are updated in time, similar to the standard finite element procedure. These solution variables are then advected back onto the background mesh during the Eulerian step. Additionally, during the Eulerian step, the nodes on the interior of the background mesh may be moved to ensure a relatively smooth/regular mesh. A subset of these MMALE methods is the Multi-Material Eulerian method (MME). These MME methods are a special case of the MMALE methods where the background mesh is fixed in space. In general, the background mesh for the MME problems is constructed in a regular grid (i.e. rectangular elements with 90 degree angles).

In the elements containing multiple materials (mixed elements), a mixture theory is used to describe the element level material response based on the interactions between the individual

materials. In all mixture theories, two assumptions are made [17]. First, the mean strain rate of a

mixed element ($\dot{\bar{\boldsymbol{\varepsilon}}}_{Element}$) is the volume weighted average of the strain rate in the materials

$$\dot{\bar{\boldsymbol{\varepsilon}}}_{Element} = \sum_{m=1}^{nmat} \dot{\boldsymbol{\varepsilon}}_m \frac{V_m}{V_{Element}} \tag{3.33}$$

and second, the mean stress ($\bar{\boldsymbol{\sigma}}_{element}$) of a mixed element is the of the volume weighted average

of the stress in each of the materials

$$\bar{\boldsymbol{\sigma}}_{element} = \sum_{m=1}^{nmat} \boldsymbol{\sigma}_m \frac{V_m}{V_{Element}} \tag{3.34}$$

Mixture theories deviate in their underlying assumptions that stem from the MMALE

formulation. One such approach is to assume that the mean strain rates in all of the materials are

the same. A second approach is to assume that the elements are small enough that the materials

are all in pressure equilibration. In both of these cases, the resulting assumptions act to fully bond

the interfaces of the materials in the mixed elements. A third formulation which allows for the

slip and separation of the materials in mixed elements is called the contact mixture theory [17,

18]. This approach applies the constraints

$$[\boldsymbol{\sigma}] \cdot \boldsymbol{n} = 0 \tag{3.35}$$

$$[\nabla \boldsymbol{u}] \cdot \boldsymbol{t} = 0 \tag{3.36}$$

are enforced between each material interface [17]. The notation $[a]$ refers to a jump in a across

the material interface, $\boldsymbol{n}$ is the interface normal vector, $\boldsymbol{u}$ is the material velocity, and $\boldsymbol{t}$ is the

interface tangent vector. This constraint requires the knowledge of the individual material

velocities is required to generate a unique solution using

$$\sum_{m=1}^{nmat} \nabla \boldsymbol{u}_m \frac{V_m}{V_{Element}} = \overline{\nabla \boldsymbol{u}}. \tag{3.37}$$

As the standard MMALE methods do not track individual material velocities, an extended finite element approach is required to resolve this issue. The details of this implementation can be found in Ref. [18].

3.5 Chapter references

[1] M.L. Wilkins, *Methods Comput. Phys*. **3**, (1964).

[2] R.D. Krieg, D.B. Krieg, *J. Press. Vessel Tech*., **99**, 510 (1977).

[3] G.R. Johnson and W.H. Cook, *Eng. Fract. Mech.* **21**, 31 (1985).

[4] G.R. Johnson and W.H. Cook, *Proc. 7th Int. Symp. on Ballistics* 541 (1983).

[5] Livermore Software Technology Corperation, *LS-DYNA User's Manual, Volume I Revision 7* Livermore Software Technology Corperation, Livermore, 2013.

[6] E. Grüneisen, *Annalen der Physik*, **344**, 257 (1912).

[7] D.L. Chapman, *Phil. Mag. Series 5*, **47**, 90 (1899).

[8] Y.B. Zel'dovich, Zhurnal Eksperimental'noi i Teoreticheskoi Fiziki [*Journal of Experimental and Theoretical Physics, JETP*], **10**, 542 (1940). Translated into English in National Advisory Committee for Aeronautics Technical Memorandum No. 1261 (1950).

[9] E.H. Lee, H.C. Hornig, J.W. Kury, *Adiabatic expansion of high explosive detonation products*. Report UCRL-50422. Livermore, CA: Lawrence Livermore National Laboratory: 1968.

[10] D.J. Benson, J.O. Hallquist, Comput. Methods Appl. Mech. Eng., **78**, 141 (1990).

[11] Livermore Software Technology Corperation, *LS-DYNA Theory Manual* (revision 4778), Livermore Software Technology Corperation, Livermore, 2014.

[12] R.A. Gingold, J.J. Monaghan, Mon. Not. R. *Astron. Soc*. **181**, 375 (1977).

[13] J.J. Monaghan, Annu. Rev. Astron. Astrophys., **30**, 543 (1992).

[14] T. Belytschko, Y.Y. Lu, and L.Gu, *Int. J. Numer. Methods Eng*., **37**, 229 (1994).

[15] D.J. Benson, *Comput. Methods Appl. Mech. Eng*., **99**, 235 (1992).

[16] E. Herbold, V. Nesterenko, D. Benson, J. Cai, K. Vecchio, F. Jiang, J. W. Addiss, S. M. Walley, and W. G. Proud, J. Appl. Phys. **104**, 103903 (2008).

[17] D.J. Benson, *Comput. Methods Appl. Mech. Eng.,* **140**, 59 (1997).

[18] E. Vitali, D.J. Benson, *Int. J. Numer. Methods Eng.,* **67**, 1420 (2006).

Chapter 4

Drop Weight Experiments and

Simulations

4.1 Chapter introduction

The dynamic behavior of granular/porous reactive materials has attracted significant attention due to its possible practical applications: reactive structural components, reactive fragments, etc. [1-3] The performance requirements introduce challenging fundamental problems such as combining high strength with ability to undergo controlled bulk disintegration producing small-sized reactive fragments.

The material structure which can meet this and other requirements should be tailored and optimized at the mesoscale to produce the desirable mechanical properties while still facilitating the release of chemical energy. Mesostructural parameters like particle size and morphology can affect the strength and shock-sensitivity. This can be seen in pressed explosives [4, 5] and in reactive materials like Al-PTFE composites [6]. Additionally, mesoscale features like force-chains in granular energetic materials may also serve as ignition sites [7-9].

Quasi-static, Hopkinson bar, and drop-weight experiments were performed for PTFE-Al-W and for Al-W composites [10-18] with different particle sizes of W, porosity, and morphology. W particles were used to increase sample density and generate the desirable mode of disintegration of the sample into small-sized debris. Multi-material Eulerian hydrocode

simulations of the dynamic tests for the various types of samples were used to elucidate the observed experimental results [11, 16, 18].

The complexity of the dynamic behavior of granular/porous materials is caused by the significant role of the mesoscale parameters including the particle sizes of components, the formation of force chains, the morphology of particles, and the bonding between particles. In these materials, shear localization and fracture can be delayed by strain hardening mechanisms such as compaction which results in porosity reduction [17, 18]. Usually, in solid metals, shear localization under high strain rate loading is due to thermal softening [19] though shear localization may also occur due to other softening mechanisms when thermal effects are negligible [20]. Shear localization in plane strain conditions similar to those used in this paper for the numerical modeling was observed in fcc metals such as Al 7075-T6 [21] and stainless steel 304L [22, 23]. Strain controlled mesoscale fracture of brittle particles can act as a "softening" mechanism (qualitatively different then the softening mechanism due to adiabatic heating) increasing the propensy of macroshear instability [24, 25].

In this chapter, the dynamic behavior of Al-W granular/porous composites, their susceptibility to shear localization, and their subsequent fracture at large strains was investigated using drop weight experiments and representative numerical simulations. Specifically, the bonding between the Al particles, the initial porosity, the relative particle sizes of Al and W, the arrangements of the W particles, and the constitutive behavior of Al was examined in Al-W granular/porous composites.

4.2 Preparation of Al-W granular porous composites

High density Al-W granular/porous composites were prepared from an elemental powder of Al (Alfa Aesar, -325 mesh), and W wires (A-M System, diameter of 200 μm and length of 4 mm) using (a) cold isostatic pressing (CIPing) and (b) CIPing followed by vacuum encapsulation

and subsequent hot isostatic pressing (HIPing) to create metal bonding between Al particles. All samples had the same mass ratios of the Al and W components (23.8% Al and 76.2% W, by weight, corresponding to a volume ratio of 69.0% Al and 31.0% W) with a theoretical solid density of 7.8 g/cm^3. Mixtures of Al powders and W wires were placed in a cylindrical stainless steel mandrel with moving pistons and encapsulated in a rubber jacket providing axial loading during pressurization in the CIP chamber. This allowed the preparation of samples with the exact sizes and cylindrical shape that were necessary for the strength measurements. All samples were CIPed at 345 MPa under room temperature for 5 min. Subsequent HIPing for some samples were carried out at 200 MPa at a temperature of 500 degree Celsius with a soaking time 20 min. The density of the samples was measured by the hydrostatic method. The samples had an average density of 6.8 g/cm^3 after CIPing and 7.5 g/cm^3 after CIPing and HIPing. Examples of the processed CIPed samples are presented in Figure 4.1.

| (a) | (b) | (c) |
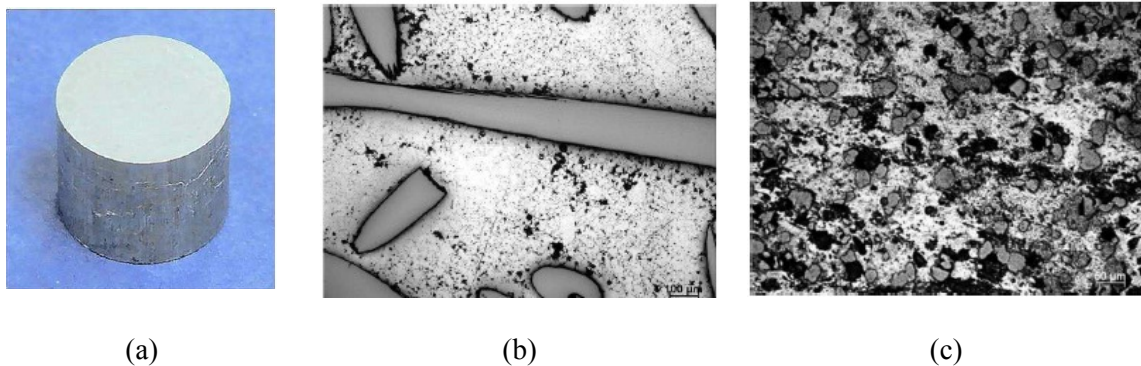
Figure 4.1 - Example of CIPed Al-W sample (a) and examples of the mesostructures with Al powders W rods (b) and Al powder/ W powder (c).

4.3 Experimental details and results of the drop weight experiments

The dynamic behavior and fracture of the CIPed and CIPed+HIPed samples were investigated at a strain rate of 1000 s^{-1} using drop weight tests (nominal velocity of the drop

weight was 10 m/s) using the high velocity DYNATUP model 9250HV with an in-house modified anvil supporting the sample detailed in Section 2.1. The undeformed CIPed only, CIPed+HIPed, and solid Al6061-T6 samples are presented in Figure 4.2. After the dynamic tests, shear macrocracks were well developed in the CIPed+HIPed samples Figure 4.3 (b), while no shear macrocracks were observed in the CIPed only samples (see Figure 4.3 (a)) at similar global strains. In the CIPed only sample, Al particles were ejected from the outer regions of samples leaving areas of interconnected and mechanically locked W wires (see Figure 4.3 (a) and (e)). The microscopic images of the deformed samples representing areas at the vicinity of macroscopic shear localization, plastic flow and deformation of W and Al particles are presented in Figure 4.4. It is evident that the bonding between the "soft" Al particles facilitated shear localization in CIPed+HIPed samples. As a result of localized plastic flow in the matrix of Al particles we have observed regions of heavily deformed and practically undeformed Al particles.

For comparison, dynamic tests were performed with as is Al 6061-T6 and annealed Al 6061-T6 (temperature 425C, 2.5 hours in vacuum) cylindrical samples under similar conditions of impact and similar or larger final global strains in comparison with CIPed or CIPed+HIPed samples (see Figure 4.3 (c) and (d)). The as is Al 6061-T6 and annealed Al 6061-T6 samples did not exhibit signs of shear localization at this level of strains.

Table 4.1 –The description of the particle sizes of the Al and W powders used in the experimental granular porous granular composites.

	Particle diameter (μm)	% of Material
-325 Mesh	31.9	50
	15	40
	4	10
Fine	40	-
Coarse	200	-

Table 4.2 - Initial dimensions of the experimental samples used in the drop weight tests.

Sample	Height [cm]	Diameter [cm]
CIPed only	1.45	1.58
CIPed +HIPed	1.39	1.54
Solid Al 6061-T6	1.25	1.18
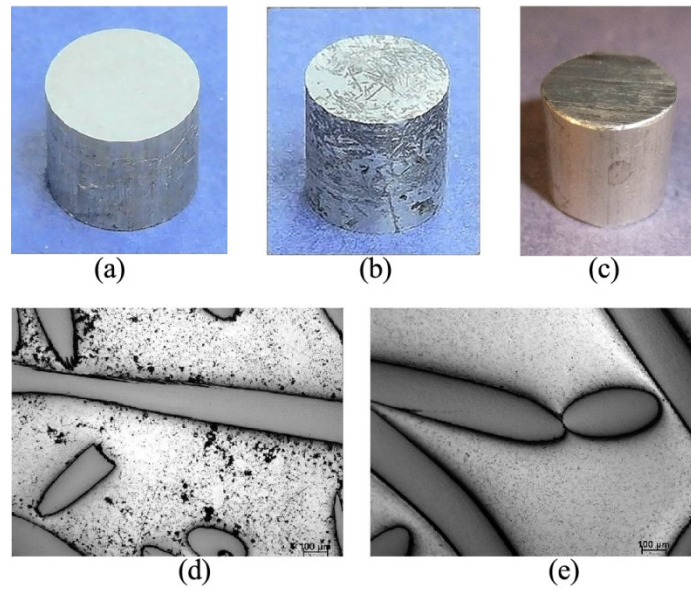
Figure 4.2 - Initial CIPed (a) and CIPed+HIPed Al-W samples (b) and a sample of solid Al 6061-T6 (c). Sample diameters and heights are given in Table 4.2. Mesostructures of CIPed and CIPed+HIPed samples before dynamic deformation are presented in (d) and (e) respectively.
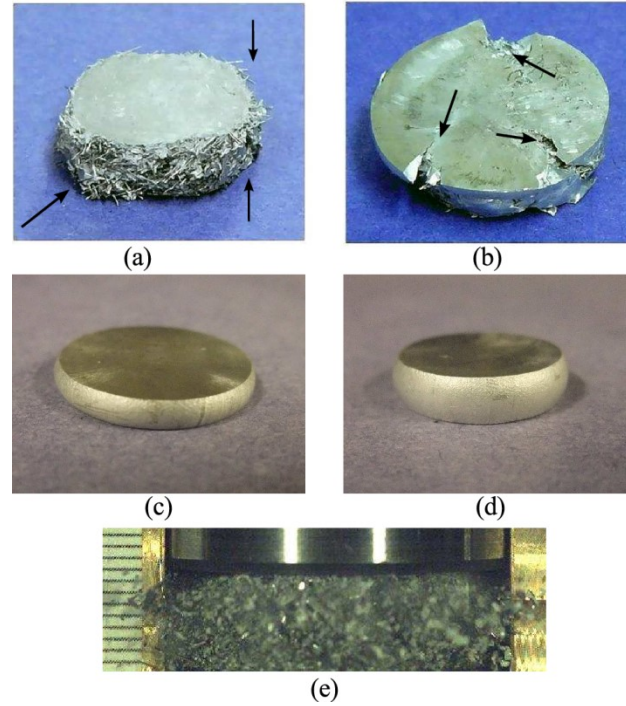
Figure 4.3 - Deformed shapes of the CIPed (a) and CIPed+HIPed samples (b). For comparison, the deformed annealed Al 6061-T6 samples and Al 6061-T6 are presented correspondingly in (c) and (d). A high speed camera photo (e) captures the behavior of Al fragments as they are ejected from the CIPed sample during a dynamic test. Arrows are added to show areas where the Al particles on the outer area of the CIPed sample have been ejected (a) and the shear bands that form in the CIPed + HIPed samples (b).
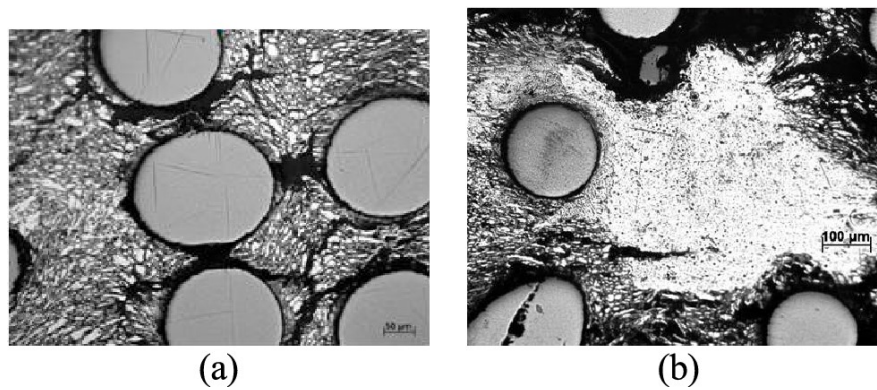
Figure 4.4 - Microstructure of deformed CIPed+HIPed samples (a) and (b) illustrating a region of largely undeformed Al particles neighboring heavily deformed and fractured areas of Al particles with different arrangements of less deformed W rods.

4.4 Numerical modeling

4.4.1 Simulation of CIPing process

Due to the large differences in the size scales between the global sample size O(cm) and the size scale of the mesostructural components O(μm), a representative volume element (RVE) was considered for the modelling of the dynamic experiments. The simulations using the CIPed mesostructures examined two different cases; the first is examination of Al and W powders that both have the -325 mesh particle distribution and the second was the examination of mesostructures with the -325 mesh Al powder and W rods with 200 μm diameter. In both situations, the mesostructure was generated using the same procedure which is outlined in the following paragraphs.

A number of assumptions were made to simplify the mesostructure of the Al-W granular composites such that it would be possible to perform and the analysis in a reasonable amount of time, while still being able to capture the major details of the experiment. First, it was assumed that the since the powders of the Al and W before CIPing were more or less spherical (spherical polyhedral) and therefore could be represented in two dimensions as circular discs. Secondly, it was assumed that the distribution of the initial particle sizes of the -325 mesh could be characterized by a combination of three discrete particle sizes of 32, 15, and 4 μm with a volume percentage of 50%, 40%, and 10% respectively. Thirdly, it was assumed that the material properties in each of the particles were identical, i.e. there were no initial defects or inhomogeneties in the particles themselves. Finally, it was assumed that prior to CIPing, the Al and W particles were thoroughly mixed and did not exhibit any self-organization into clusters or gradients in the local particle distribution.

With these assumptions in mind, the rectangular domain with a size 10 times the size of the largest particle size was populated with particles in the following procedure. First, the desired

post CIPed volume fractions of the Al and W (70% Al, 30% W) and the size of the RVE were used to calculate the number of each particle size was needed to populate the domain by

$$N_i = \frac{vf_i \, vf_{mat} \, V_{total}(1 - vf_{porosity})}{r_i^2 \pi} \qquad (4.1)$$

where N_i is the number of particles for a particular particle size, vf_i is the desired volume fraction of the particular particle size, vf_{mat} is the volume fraction of the material (either Al or W), v_{total} is the total volume of the desired simulation domain after the CIPing simulation, $vf_{porosity}$ is the volume fraction of the desired porosity after CIPing.

Once the number of particles was determined, the total number of each particle size was combined and the algorithm began placing particles one by one from largest to smallest. The algorithm placed the *i*th particle in the following manner. The *i*th particle was randomly placed in the domain such that it is at least 1 radius distance from the boundary. Then the distance between the placed particle and all previously placed particles is checked against the sum of the two particle radii. If there is overlap, the ith particle is once again randomly placed in the domain and the process is repeated. If there is no overlap between the ith particle and all previously placed particles, then the particle is placed and the next and the ith+1 particle is then placed in the same manner. This process proceeds until all particles are placed with no overlap. Since the theoretical packing density of randomly distributed discs is significantly less than the organized, optimal packing density, the height of the computational domain was increased such that the initial porosity would be equal to 20%. This allowed for a rapid placement of all particles in the domain.

After all of the particles have been placed, each of the particles is randomly assigned a material based on the number of predetermined particles calculated above. A final step must be taken due to the nature of the Eulerian formulation which has the concept of material entities. In the Eulerian formulation, components are defined as materials and stored as volume fractions in the background elements. If two of these entities of the same material contact each other, the

entities would merge into a single entity completely removing the interface. Since it is expected that there may be large plastic strain and/or movement of particles from their original location, each of the particles was assigned a material number such that there was not a similar material number used within a region with a width equal to four times the largest particle radius.

Since the CIPing process is assumed to be quasi-static and adiabatic the strain rate and temperature dependencies of the material models may be neglected. Furthermore, since the CIPing pressure (345 MPa) is significantly under the yield strength of the W (770-1200 MPa) and there was no observed fracture or deformation of W particles in the CIPed samples, the W material was assumed to be in the elastic regime and therefore could be modeled as a linear elastic material. The Aluminum was modeled using the Johnson-Cook constitutive model in conjunction with the Gruniesen equation of state. However, the parameters associated with the temperature and strain rate were chosen such that the material response was insensitive to the strain rate or temperature effects. The parameters used for the W and Al are presented in Table 4.3.

The mesh density of the background Eulerian mesh was chosen such that 5 elements spanned the diameter of the smallest component in the sample. This provided an adequate balance between speed and ability to capture the stresses in the smallest components.

The CIPing process was simulated by imposing zero normal velocity boundary conditions on the sides and bottom of the domain. A thin rigid strip of material was added to the top boundary and a constant normal velocity of 1 m/s on the top boundary to simulate the uniaxial compression of the sample. Since the process of CIPing involves high pressures relative to the yield stress of the Al particles, it is assumed that there is little to no slipping of Al boundaries. As such, a simple mixture theory to handle the mixed elements was used. This mixture theory maintains a constant pressure in mixed elements.

The resulting CIPed simulated mesostructures are presented in Figure 4.5. This mesostructure shows similar qualitative features as the CIPed mesostructre presented in Figure 4.1 (c).

(a)   (b)
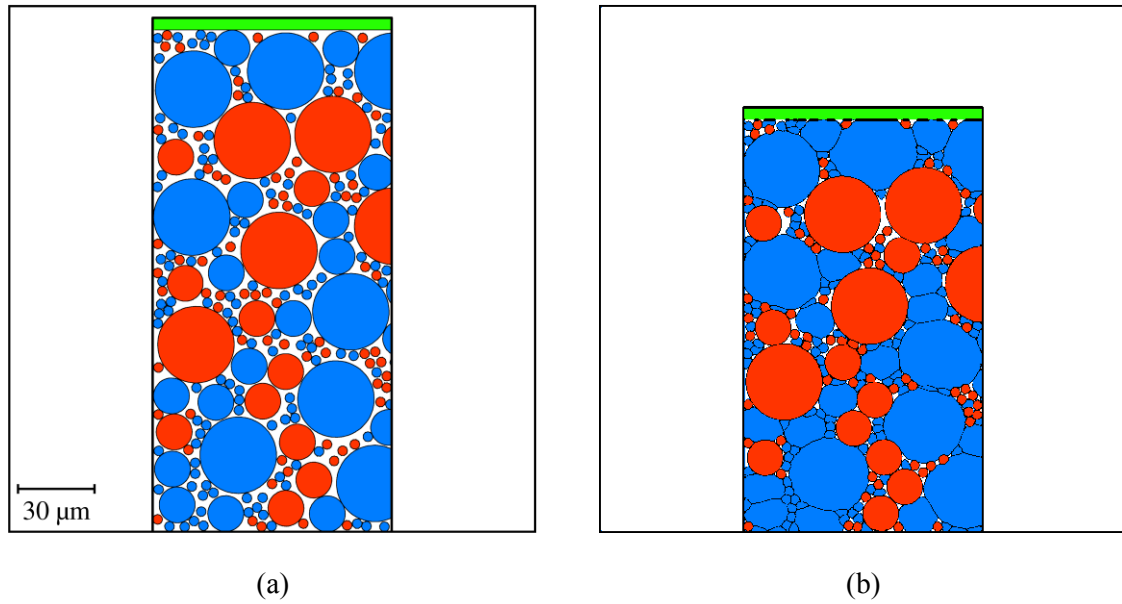
Figure 4.5 - An example of the simulation mesostructure (a) before the simulated CIPing and (b) after simulated CIPing.

Table 4.3 - Constitutive model and equation of state material properties used in the numerical simulations for the Al and W components

Material parameter	Al 6061-T6 [24, 25]	W[24, 26]
Johnson-Cook		
ρ_0 [gm cm^{-1}]	2.7	16.98
G [Mbar]	26.0	1.24
A [Mbar]	224.0	1506
B [Mbar]	111.4	176.5
n	0.42	0.12
C	0.002	0.0016
m	1.34	1.0
C_p [J kg-1 K-1]	890	130
T_{melt} [K]	930	1728
T_{room} [K]	300	300
D1	-0.77	0
D2	1.45	0.33
D3	-0.47	-1.5
D4	0	0
D5	1.6	0
Mie-Grüneisen		
C_0 [cm µs^{-1}]	0.52	0.40
s_1	1.4	1.24
s_2	0	0
s_3	0	0
γ_0	1.97	1.67

4.4.2 Simulations related to the drop weight tests

A number of sample properties were examined to explore their influenced shear instability and localization during a dynamic test. The role of the metallic bonding was examined in an attempt to understand a difference between dynamic behavior of CIPed samples (no metallic bonding between Al particles) and CIPed+HIPed samples (metallic bonding between Al particles). The roles of the initial porosity, the relative particle size of Al and W, the initial

arrangement of the W particles, the confinement, and the constitutive behavior of the Al were also explored to see their effect on the shear instability in the sample. A two-dimensional Eulerian hydocode [26] was used to simulate the behavior of the samples during the drop weight tests. Due to the smallness of the particles relative to the global sample size, small representative elements of the microstructure were used in all the simulations. Metallic bonding between the particles was enforced through the contact conditions. For the CIPed only simulations, particles were allowed to slide and separate with frictionless contact. For simulations of the CIPed+HIPed samples, particles were not allowed to slip or separate effectively bonding the particles together. Details of the algorithm can be found in [27].

4.4.2.1 The initial particle arrangements, the constitutive model, and the boundary conditions

The initial particle arrangements of W and Al used in the numerical simulations are shown in Figure 4.6, Figure 4.7, and Figure 4.8. The description of the particles sizes and volume fractions for both the Al, W, and porosity are presented in Table 4.2 and Table 4.1. The samples in Figure 4.6 (a) and (b) were used to investigate the role of porosity and metallic bonding on the shear instability and formation of the shear bands in both the bonded (CIP+HIP) and non-bonded (CIP only) samples with similar sized Al and W particles. The sample in Figure 4.7 was used to investigate how relative sizes of W and Al affected the shear instability in both the bonded and non-bonded samples. Additionally, the sample in Figure 4.7 was used to examine cases with confinement boundary conditions as well as the variations for simulations looking at the role of constitutive behavior in the Al. Samples in Figure 4.8 were used to investigate the role of initial mesostructure on the shear instability in the bonded case. Numerical calculations were made in plane strain conditions effectively considering particles as the rods used in experiments.

Table 4.4 - Material volume fractions and porosity in each of the simulated samples.

Sample	Volume fraction Al	Volume Fraction W	% Initial Porosity
Figure 4.6 (a)	0.72	0.28	8.3
Figure 4.6 (b)	0.74	0.26	0
Figure 4.7 (a)	0.67	0.33	8.5

(a)   (b)
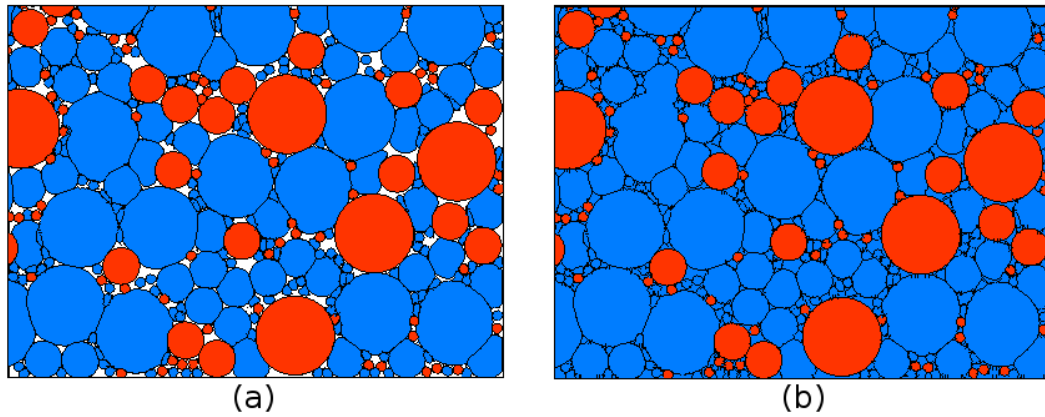
Figure 4.6 - Initial arrangements of the Al (blue) and the W (red) particles in the Al-W granular/porous representative samples with similar sized Al and W particles corresponding to -325 mesh (see Table 4.1 and Table 4.2) with an initial porosity of 8.3% (a) and with the initial porosity filled with Al (b). These simulated mesostructures have a width of 0.02 cm and a height of 0.015 cm. This mesostructure was used for the simulations where Al-Al interfaces were bonded and non-bonded. In all simulations, the W-Al and W-W interfaces were not bonded.
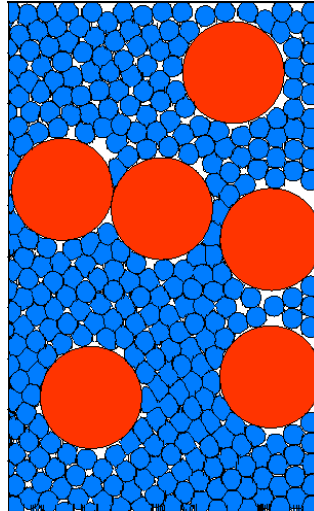
Figure 4.7 –The initial mesostructure used for the simulations with 40μm and 200μm diameter Al (blue) and W (red) respectively and an initial porosity of 8.5%. The simulated sample size was 625 μm in width and 1000 μm in height.
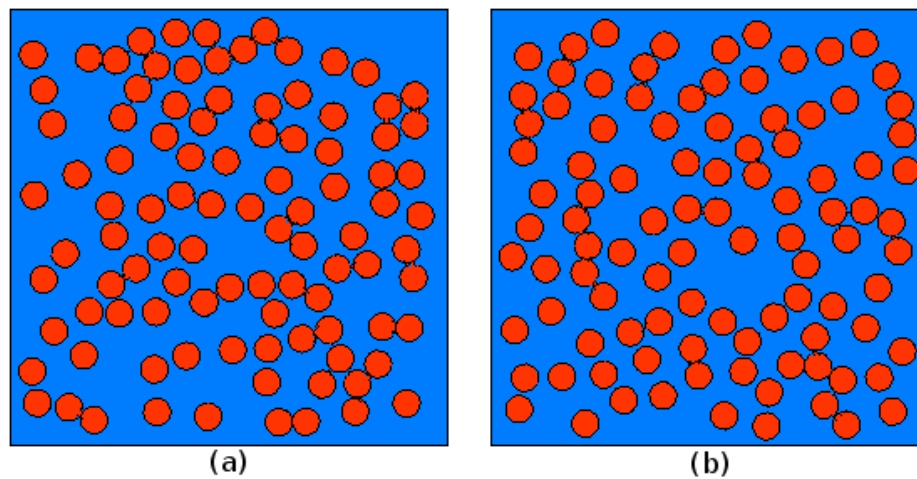
Figure 4.8 – Examples of initial mesostructures with randomly placed 200 μm diameter W (red) particles embedded in a fully dense (0% porosity) Al (blue) matrix. These simulated samples have a height and width equal to 3000 μm. In all simulations examining these type of mesostructrures, the volume fraction of the W particles was held at 0.30.

A standard Johnson-Cook with failure [28] material model and the Mie-Grüneisen equation of state used for both the Al and the W in the simulations. Failure in the material is determined through the equivalent plastic strain as shown in [28]. The material constants used in this paper are presented in Table 4.3. We did not take into account the heat conductivity implying that the conditions of deformation occurred under adiabatic conditions.

To simulate the drop weight test, a kinematic boundary condition with constant downward velocity was imposed on the top boundary corresponding to the impact speed of the falling weight in the experiment (10 m/s). For the cases where the small representative element is near the outer edge of the large cylinder, the side wall boundary conditions shown in Figure 4.9 (a) were used. In cases where the small representative element is near the middle of the large cylinder, the side wall boundary conditions shown in Figure 4.9 (b) were used to account for the confinement. A variety of confinement conditions were considered in this paper and will be detailed during the discussion of Figure 4.15. With the confinement boundary conditions, the main concern is keeping the correct description of the global deformation of the sample, but due to the artificial conditions, the agreement with global stresses is sacrificed. This confined geometry produces compressive stresses in particles leading to elevated pressures in the sample.
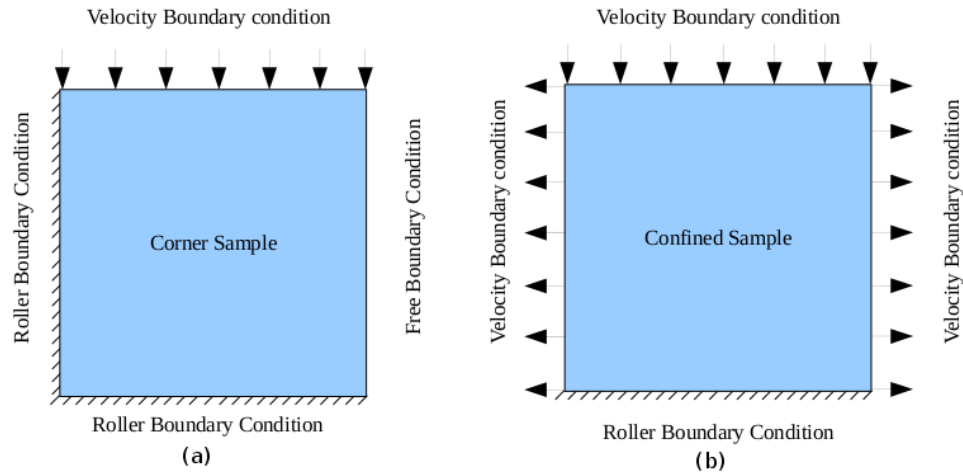
Figure 4.9 - Boundary conditions imposed on (a) corner samples and (b) internal confined samples.

4.4.2.2 The role of bonding and initial porosity in samples with similar sized Al and W particles (-325 mesh)

The results of the numerical simulations corresponding to the initial mesostructures shown in Figure 4.6 are presented in Figure 4.10 corresponding to the deformed sample with a global strain of 0.45. The sample with the bonded particles and initial porosity of 8.3% began developing shear instabilities at the mesoscale once the *in situ* densification that occurred at the early stages of deformation removed a majority of the porosity from the sample (the initial average porosity was 8.3\% and the porosity when shear instability started was 3.2%). The bonded sample with zero initial porosity began developing shear instabilities on the mesoscale within the first 0.05 global strain. The global shear band began developing around 0.25 global strain in the case with 8.3% initial porosity and around 0.20 global strain in the sample with zero initial porosity. This behavior is similar to observations in the PTFE-Al-W mixtures and in the experiments with the Al-W powder mixture [11, 12, 16-18]. The global shear localized zones and the subsequent cracks developed at an approximate 45 degree angle but was "kinked" by the rigid W particles resulting in the initial shear band forming in a range of angles from 36 to 50 degrees

(see Figure 4.11). The samples in Figure 4.10 (a) and (b) have a relatively large percentage of small W particles, providing some geometrical "homogenization" of the mixture. As a result, the shear bands do not significantly deviate from this 45 degree angle. In both samples, the mesoscale shear instabilities continue to grow until one begins to dominate (at approximately 0.25 global strain) and a global shear band develops, which in turn leads to the growth of a macro crack. While this simulation only looks at a small representative element along the edge, the experimental CIP+HIP samples exhibit the same behavior (see Figure 4.3 (b)).

The corner samples that have non-bonded particles, simulating the CIPed only material, are presented in Figure 4.10 (c) and (d). These samples do not develop shear instabilities like the bonded samples with identical initial mesostructures. In the non-bonded samples, the Al and W particles rearrange themselves during the dynamic deformation, effectively blocking shear instabilities from forming. Additionally, due to the free boundary on the right hand side, the sample undergoes bulk disintegration. Due to the two-dimensionality of the simulation and the lack of friction in the simulation, the W particles do not offer much resistance to the movement of the Al out of the right boundary. A similar behavior can be seen in the experimental samples where the Al on the edge is ejected from the sample, disintegrating into agglomerates of Al consisting of 5-30 initial sized Al particles. This ejection of the Al particles from the network of the W wires adjacent to the free boundary was observed during the dynamic loading in experiments using a high speed camera (see Figure 4.3 (e)).

Initial variations in porosity (0% or 8.3%) in the bonded sample altered the orientation of the mesoscale shear bands despite the practically identical initial mesostructure of the W particles. In the sample with porosity, the pores are bulk distributed with sizes of approximately 4 microns in diameter. This bulk-distributed porosity allows for small movements of the W particles at the initial stages of deformation due to pore closure. The shear instabilities were observed nucleating during this early stage of the deformation. The small alterations in the W

particle arrangement at this early stage therefore caused a large deviation in shear bands that developed during later stages of the deformation. The non-bonded samples with and without porosity both showed the same characteristic of particle rearrangement blocking shear band formation and bulk disintegration.
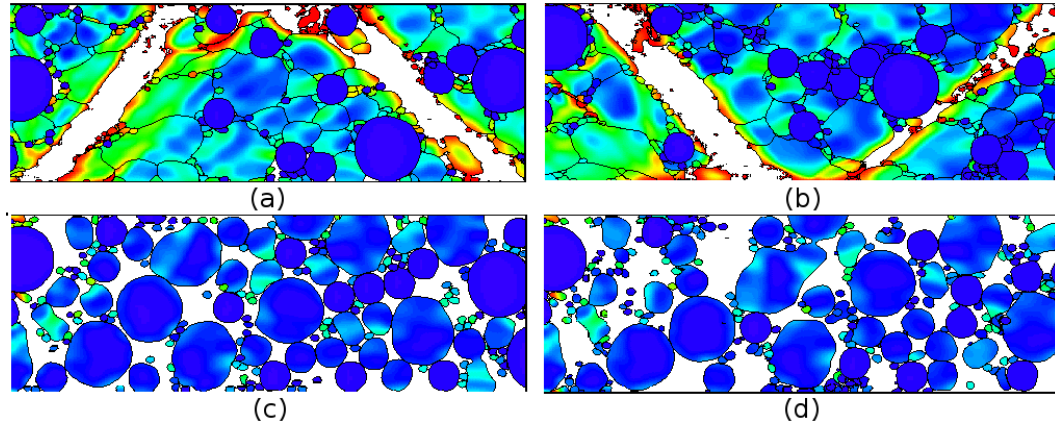
Figure 4.10 - Role of initial porosity and bonding between particles. Deformed mesostructures of -325 mesh Al and W particles with the initial arrangement of Al and W particles shown in Figure 4.6 (a) and (b). Damage is plotted to highlight the shear instability and shear bands in the sample. All samples shown at global strain of 0.45 corresponding to mesostructures presented in:

(a) Figure 4.6 (a) with bonded particles (CIPed + HIPed).

(b) Figure 4.6 (b) with bonded particles (CIPed + HIPed).

(c) Figure 4.6 (a) without bonding between particles (CIPed only).

(d) Figure 4.6 (b) without bonding between particles (CIPed only).
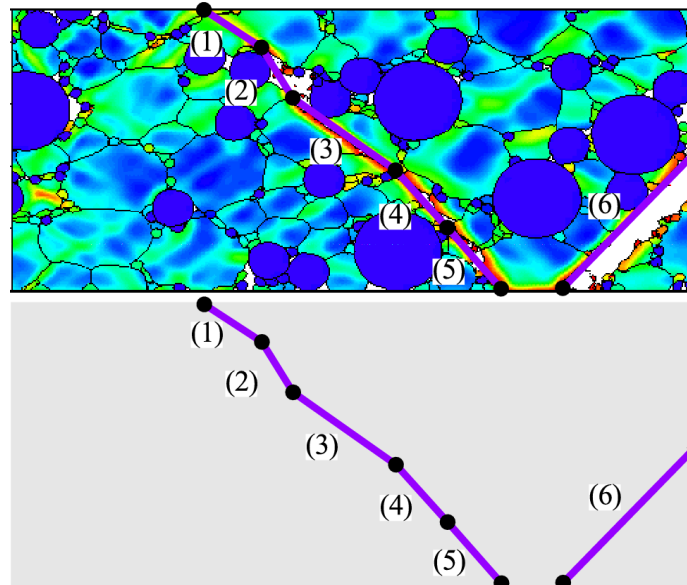
Figure 4.11 -Effect of rigid W particles on the "kinking" of the shear bands in the Al matrix with the W and the Al -325 mesh sized particles with the initial mesostructure illustrated in Figure 4.6 (a). Black dots show the kink locations of the shear bands. The angles of the piecewise shear bands are 32 (1), 58 (2), 34 (3), 47 (4), 48 (5), and 45 (6) degrees.

4.4.2.3 The role of bonding and initial porosity on samples with fine (40 micron) Al and coarse (200 micron) W particles

Numerical calculations exploring how a difference in the relative sizes between the W and Al particles (see the initial mesostructure in Fig. \ref{fig:5}) effect the development of shear instabilities and the formation of shear bands/cracks are shown in Figure 4.12. The W particles in the numerical simulations have a diameter of 200 microns, the same diameter as the W rods used in the experimental samples shown in Figure 4.2 (a) and (b). The Al particles have a diameter of 40 microns, the size of the larger particles in the -325 mesh particle size used in the experimental sample. The boundary conditions are the same as those described in Figure 4.9 (a) with a constant downward velocity of 10 m/s on the top boundary.

In the bonded sample simulating the CIPed+ HIPed material (Figure 4.12 (a) and (b)), shear instabilities begin developing after the pores close like the porous sample with similar sized Al and W particles shown in Figure 4.10 (a). Mesoscale shear bands develop at approximately 0.25 global strain. The shear band that forms is heavily influenced (guided) by the W particles in its path. When comparing the shear bands in Figure 4.12 with those in Figure 4.10, the W particles that are larger relative to the Al have a much greater influence on directing and altering the path of the shear bands. The larger W particles require the shear instability to circumvent a larger radius of the relatively rigid W particle to connect with instabilities that form in the Al on the other side of the W particle. In Figure 4.12 (a) the shear band can be clearly seen circumnavigating the W particle in the upper central region, causing the shear band to turn almost 90 degrees from one side of the particle to the other. The shear band in the lower section of the same figure is directed between two adjacent W particles. Due to the larger relative size of the W to the Al particles, the heterogeneous nature of the sample is increased in comparison to the previous samples in Figure 4.10, where the small W particles homogenized the mesostructure. This heterogeneity creates areas of mostly undeformed Al to appear in regions away from W particles and areas of deformed Al to appear in regions near W particles. Based on the simulations, the path of the shear bands closely follows the W particles in CIPed+HIPed material. This behavior is in agreement with the experiments (see Figure 4.4).

In the non-bonded sample simulating the CIPed only material in Figure 4.12 (c) and (d), the bulk distributed rearrangement of the Al and W particles effectively block the development of shear bands. This rearrangement is similar to that of the particles in Figure 4.10 (c) and (d). Like the previous case due to limitations in the two-dimensionality of the simulations some of the three-dimensional W fiber effects cannot be reproduced. However, the trends seen in this two-dimensional simulation can also be seen at the edge of the experimental sample where the Al is ejected from the edge of the cylinder during the dynamic test as shown in Figure 4.3 (a) and (e).

4.4.2.4 The relationship between sample strength and porosity in corner samples

The engineering stress at the upper and lower boundaries versus the global strain for the simulation of bonded sample described in Figure 4.12 is shown in Figure 4.13. The solid red curve and the dashed black curve show the average engineering stress on the top and bottom boundaries respectively and are nearly identical except for the first 0.04 strain. Based on this, the sample can be seen as undergoing a "quasi-static" deformation. In addition to the stress, the percentage of porosity in the sample was plotted to show the relationship between the porosity and sample strength. It can be seen that stresses in the sample increased until a global strain of 0.12 was reached. The maximum of stress corresponds to the minimum porosity due to in situ densification during the initial stage of deformation. After the densification stage (corresponding to a range of global strain 0.12-0.29), the stress begins to drop as the local shear bands begin forming and the global shear band develops. Later (0.30 global strain) macrocracking occurred resulting in a decrease in strength accompanied by a rapid increase of porosity. This behavior is similar to the behavior observed in [11, 12, 16-18]. The two-dimensional simulation of the non-bonded material, due to the material rearrangement, had near zero engineering stress on the top and bottom boundary and was not included. The comparable strength of bonded and unbounded samples in experiments is mostly due to interconnected W wires that cannot be accounted in these two-dimensional simulations.
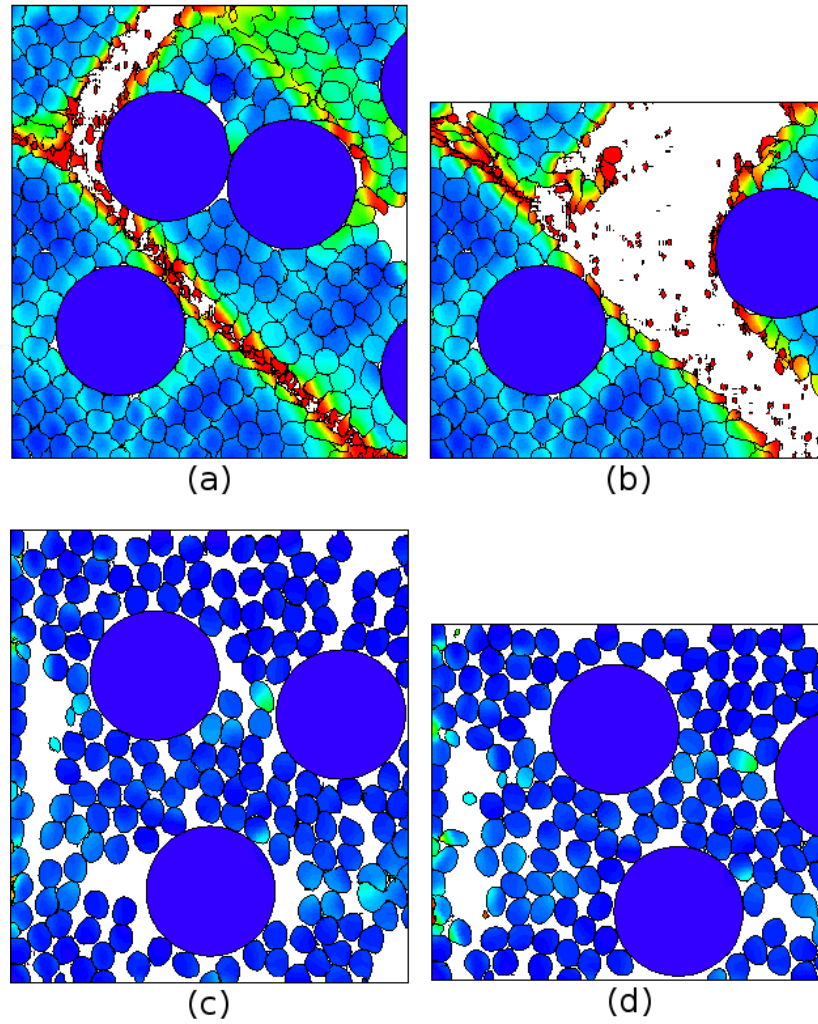
Figure 4.12 - Role of relative particle sizes of W and Al in bonded (a), (b) and unbounded samples (c), (d) at two different global strains of 0.30 (a), (b) and 0.45 (c), (d). The initial mesostucture is shown in Figure 4.7. Damage is plotted to highlight the shear instability and the shear band development.
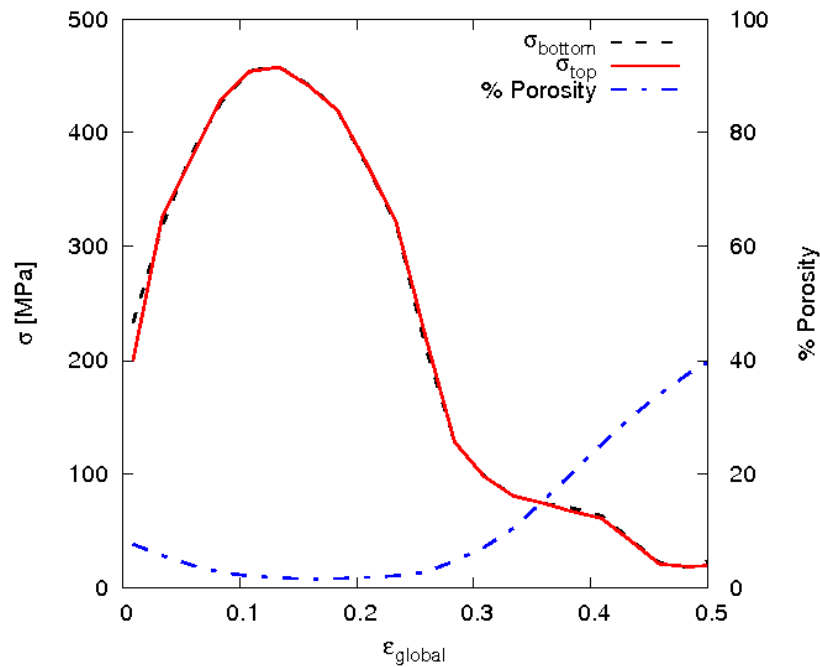
Figure 4.13 - Average engineering stress versus the global strain at the top boundary (solid red line) and at the bottom boundary (dashed black line) of the corner sample corresponding to initial mesostructure presented in Figure 4.7 and velocity of impact 10 m/s. The porosity in the sample versus global strain is also plotted (blue dashed and dotted line).

4.4.2.5 The role of initial arrangement of W particles in CIPed+HIPed samples (bonded) with zero initial porosity

Experimentally tested samples had the W fibers initially placed in a random fashion. Multiple "randomized" samples were created for numerical analysis to understand how different experimental realizations of this randomized W fiber placement effects the formation of shear instabilities during dynamic deformation. In two characteristic samples with initial mesostructure presented in Figure 4.8, the W particles were randomly placed in an Al matrix such that the volume fractions of W and Al in each sample were identical. The samples were then subjected to boundary conditions described in Figure 4.9 (a) with a constant 10 m/s downward velocity. All

samples had zero initial porosity to remove mesostructural changes due to void closure as seen in simulations described in Figure 4.10. Results of the two characteristic simulations are shown in Figure 4.14, demonstrating variations in the shear instabilities and shear band development while highlighting the similarities that the samples share.

Both samples in Figure 4.14 have damage plotted to highlight the shear band formation, with red corresponding to fully damaged Al. It is obvious from the comparison of the deformed samples in Figure 4.14 (a) and (b) that changes in the initial mesostructure (see Figure 4.8 (a) and (b)) greatly alter the location of the shear band despite the same volume content of Al and W and the same size of W particles.

While both samples in Figure 4.14 have very different shear band locations and modes of fracture, there are a number of similar characteristics that the samples exhibit.

First, both samples develop shear instabilities and shear bands at approximately the same global strain of 0.20. It should be mentioned that in these samples with zero initial porosity, the global strains corresponding to well-developed shear localization are similar to the corresponding global strains in the initially porous samples (see Figure 4.10 and Figure 4.12).

Second, numerous local shear instabilities form due to the localized, high strain flow of the softer Al particles around the harder W particles. These local instabilities link with other local shear instabilities in close proximity creating localized shear bands. These bands join with other localized shear bands until one global shear band transverses the entire sample and becomes the dominant macroshear band. This macroshear band has a propensity to form at a 45 degree angle, with its path locally altered by W particles, and spans the entire sample before subsequent global shear bands are able to form. This demonstrates that the relatively rigid W particles initiate the shear instability in these granular composites, enhancing the localized high strain plastic flow of Al around the W particles. Local plastic strain in the Al around the W particles was 3 to 4 times higher than the plastic strain in the surrounding Al thus facilitating localized damage and

subsequent global shear localization within the Al matrix. Separate experiments and numerical simulations with cylindrical samples made of as is Al 6061-T6 and annealed Al 6061-T6 did not reveal shear localization at similar or larger global strains (see Figure 4.3 (c) and (d)).

Third, the W particles are largely responsible in dictating the path of instabilities. This can be seen clearly in the bottom center region of Figure 4.14 (a), where the shear band develops two branches that circumvent a clump of W particles and reconvene on the bottom boundary. Additionally, in the top central region of Figure 4.14 (a), a closely packed clump of W particles block shear instabilities from developing in this region. This may be due to a similar effect as seen in Figure 4.10 (a) and (b) in addition to Figure 4.12 (a), where having the W particles initially aggregated into a close pack causes the shear instability to move around the relatively rigid mass into the softer area of the surrounding composite. The same effect can be seen in areas of the samples in Figure 4.14 where the W particles group in very close proximity to each other.

Finally, due to the random nature of the sample, some of the W particles form angular chains with channels of Al between them facilitating the growth of shear instabilities and shear bands along the channel. The sample in Figure 4.14 (b) exemplifies this with W particles creating a channel structure spanning the entire sample going diagonally from the lower left corner to the upper right corner. This channel created a favorable path for the local instabilities to follow and eventually lead to the formation of the shear band in the sample. W particles "flow" along the shear band to help form these angular chains. Rearrangement of the rigid particles inside high strain shear flow was observed in explosive compaction on interfaces between particles with high strain shear deformation [32]. In Figure 4.14 (a) a distinct global chain structure of W particles is not present like in Figure 4.14 (b), but rather a series of shorter chain structures in the left and the upper right region of the sample. This lack of long chains may be the reason that the sample accumulated more bulk-distributed damage in comparison to Figure 4.14 (b).
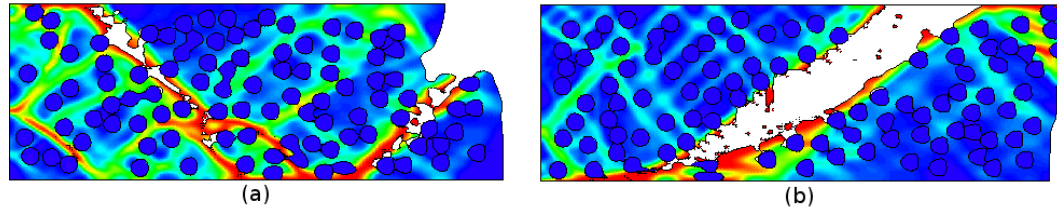
Figure 4.14 – The role of initial mesostructure of the W particles on the shear localization and the subsequent fragmentation with zero initial porosity. The deformed samples at 0.50 global strain shown in (a) and (b) correspond to the initial mesostructures presented in Figure 4.8 (a) and (b) respectively.

4.4.2.6 The role of kinematic confinement conditions

Previous simulations examined small representative elements corresponding to a material on, or very near to, the outer edge of the experimental sample. A small representative element near the central region of the sample interacts with surrounding material which resists movement of material leaving the representative element. To account for this "confinement" from the surrounding material, kinematic boundary conditions using a ramped normal velocity were imposed on the sides. Multiple velocity ramps were explored in an attempt to model the large variance in the local inhomogeneity within the sample, resulting in various local "confinements". The first ramp velocity tested kept the global Poisson ratio of the small representative sample geometrically consistent with that of the experimental sample. Two additional constrained boundary conditions were tested corresponding to 70% and 100% increased horizontal expansion in comparison with the geometrically constrained case. The vertical strain rate was kept identical for all samples. Figure 4.15 shows the simulation results at 0.30 and 0.50 global strains respectively for the samples with the constrained side boundary conditions. Damage is plotted to highlight the shear instabilities.

Shear bands developed in all samples at approximately 0.25 global strain. However, the location and number of shear bands differed in each case. Despite these differences, all the samples share a similar characteristic: areas of heavily deformed Al particles near the W particles,

resulting in local damage accumulation and subsequent shear band formation, while material further away from the W particles is relatively undeformed. This trend seems to be independent of the imposed confinement conditions. Also, samples in Figure 4.15 (b) and (c) exhibit cracks that form between the W particles. The crack locations are very similar to the location of cracks in the large experimental sample (see Figure 4.15 (b)). The cracks span between the W particles in the areas of the heavily deformed Al. In the simulations, the W particles move, squeezing the Al particles between the nearby W particles, acting as "anvils" that facilitate the heterogeneous deformation of the Al particles. A similar effect may occur in the large experimental sample where the Al flows around the W fibers due to the three-dimensional cage like network that the packed network of W fibers create. A similar effect of rigid and heavy W particles is instrumental also in the shock loading of corresponding mixtures allowing tailored redistribution of internal energy between components [11, 12].
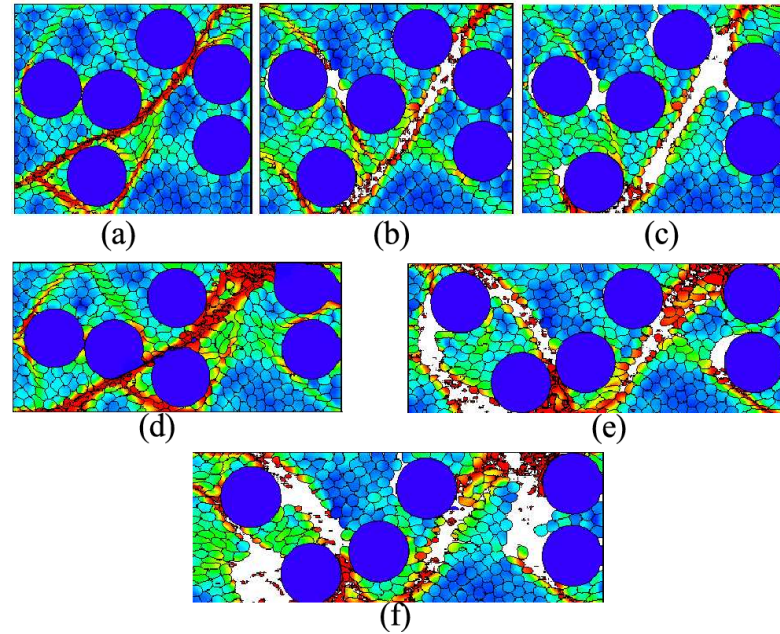
Figure 4.15 - Role of different conditions of confinement on shear localization and subsequent fracture. Three deformed mesostructures at 0.3 and 0.5 global strains with various confinement conditions are presented. All three samples have boundary conditions described in Figure 4.9 (b) with a constant 10 m/s downward velocity imposed on the top boundary. Each sample differs only in the imposed horizontal velocity on the side boundaries (linear ramp as vertical strain goes from 0 to 0.5) in the following way:

(a), (d) A linear ramp from 0 to 7.20 m/s. Corresponding to a final horizontal strain equal to 0.58. This produces the representative element to keep the same geometric proportions as in the experiments. Sample shown at 0.3 (a) and 0.5 (d) vertical strain.

(b), (e) A linear ramp from 0 to 12.24 m/s. This corresponds to a horizontal strain 1.0. Sample shown at 0.3 (b) and 0.5 (e) vertical strain.

(c), (f) A linear ramp from 0 to 14.40 m/s. This corresponds to a horizontal strain of 1.16. Sample shown at 0.3 (c) and 0.5 (f) vertical strain.

4.4.2.7 The role of the constitutive behavior of Al

The constitutive behavior of the Al particles were modified to explore how they influenced the shear instability and the shear band formation in the bonded samples (CIPed plus HIPed samples in experiments). Simulations were carried out with the initial mesostructure shown in Figure 4.7 and the boundary conditions in Figure 4.9 (a) with a constant 10 m/s downward velocity on the top boundary. The initial yield stress of Al was reduced to a very low level 20 MPa from 324 MPa corresponding to all previous simulations and the results are shown

in Figure 4.16. The sensitivity of shear band development to other parameters in the Johnson-Cook model such at temperature softening and strain rate sensitivity were also explored, however, these simulations showed that there were only slight changes in the material response due to these alterations and results are not presented in this paper. This indicates that shear instability in these granular composites is caused by damage accumulation due to the local high strain flow of the Al around the W particles and not due to thermal softening.

The reduction of the initial yield stress in the material from that of Al 6061-T6 (324 MPa) to that of a much softer Al (20 MPa) caused a large change in sample response. The Al particles in Figure 4.16 experiences greater plastic flow and deformation in all areas of the sample, especially in the areas around the W particles (compare to Figure 4.12). Due to the softening of the Al matrix, the development of the global shear band was delayed, allowing for more bulk-distributed plastic flow of the Al. The reduction of initial yield stress in the Al resulted in a shear band developing in a different location. This is likely caused by the greater movement of W particles in the softer Al altering the arrangement of the W altering the mesostructure at the earlier stages of sample deformation.
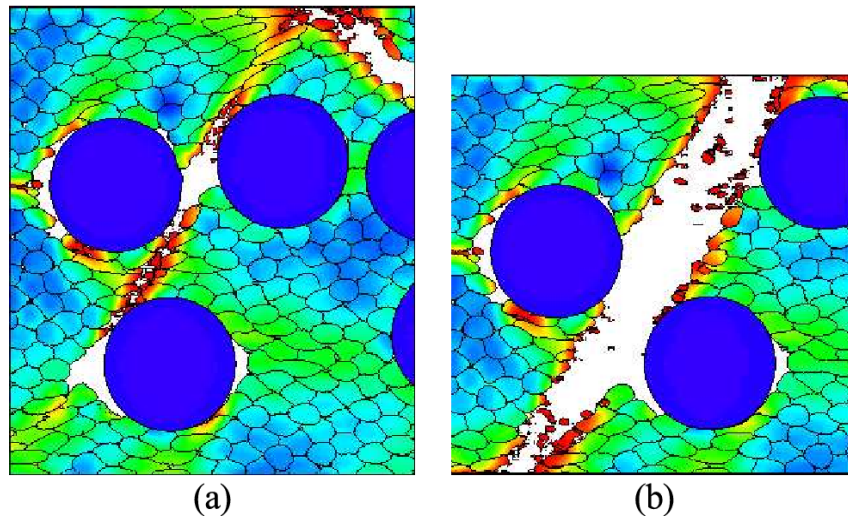
Figure 4.16 - Effect of the initial yield strength on the shear instability in porous granular composites. The initial yield strength of the Al is reduced to that of a softer Al (20 MPa). The sample is presented with global strains of 0.30 (a) and 0.40 (b). The damage is plotted to highlight the shear bands.

4.4.2.8 Modeling and results of the three dimensional mesostructure with W rods

In all previously simulations presented in this chapter, the two dimensional representation of the mesostructure was used. In some instances, the mesostructure may have architecture which has three dimensional features such as rods (see Figure 4.2 (c) and (d)) that may influence the accommodation of plastic strain and may not be captured in the two dimensional model. As such, numerical simulations of a representative element of the mesostructure were conducted to explore the effects of the three dimensional architecture.

The simulated mesostructure was assumed to consist of randomly distributed W cylindrical rods with a length of 4 mm and a diameter of 200 μm in a solid Al matrix (fully bonded) such that the packing fraction of the rods was similar to the experimental value of 0.30. The procedure for placing rods was similar to the procedure for placing the particles in the two dimensional simulations. To reduce the influence of boundary effects when placing the rods, the rod placement algorithm was applied to a cubic space with side length of 2 cm (five times the

length of a single W rod). A central cubic region with side lengths of 0.5 cm was used for the simulations to reduce the effects of rod placement near the boundaries of the placement domain.

During the placement procedure, the rod is defined by two points defining the positions of the top and bottom central axis of the rod and a radius. These three quantities are used by the volume fraction filling procedure performed by LS-DYNA prior to the start of the Eulerian analysis. The placement of rids is done sequentially until the volume fraction of the rods in the placement domain is reached.

The placement of the ith rod is done a 2 step procedure; random placement in the domain and checking for overlap with previously placed rods. First the rod is randomly placed inside the domain by first placing one point (x_{1_i}) of the rod using the following equation:

$$x_{1_i} = rand * (x_{max} - x_{min} - 2 * r_{rod}) + (x_{min} + r_{rod}) \qquad (4.2)$$

where $rand$ is a random real number between 0 and 1, x_{max} and x_{min} are the maximum and minimum coordinates of the domain in the x direction, and r_{rod} is the radius of the rod. This placement is performed for each coordinate direction (x, y, z). After the placement of the first point, the second point is placed in an iterative manner by randomly placing the point on a sphere that is centered at $(x_{1_i}, y_{1_i}, z_{1_i})$ using

$$x_{2_i} = x_{1_i} + \rho \cos \theta \sin \phi \qquad (4.3)$$

$$y_{2_i} = y_{1_i} + \rho \sin \theta \sin \phi \qquad (4.4)$$

$$z_{2_i} = z_{1_i} + \rho \cos \phi \qquad (4.5)$$

where ρ is the length of the rod, θ is the azimuthal coordinate and is a random number between 0 to 2π, and ϕ is the polar coordinate with a value that is randomly picked from 0 to π. If this point falls outside of the domain, the point placement procedure is repeated until the point falls inside the domain.

When the rod is determined to be inside the domain, it is check against all previously placed rods to ensure that there is no overlap. The algorithm used for performing this check first finds the location of the two closest points on the infinite lines defined by the rods axis and is based on the algorithm for finding the distance between lines in Ref. [33]. Then the algorithm checks if the point lies on the rod, or if this point falls on the line outside the rod, the closest end point is used in calculating the distance. To find the closest points between the infinite lines that the ith and jth rods lie on, the lines are defined using parametric equations:

$$L_1(s) = x_{1_i} + s(x_{2_i} - x_{1_i}) = x_{1_i} + su \qquad (4.6)$$

$$L_2(t) = x_{1_j} + t(x_{2_j} - x_{1_j}) = x_{1_j} + tv \qquad (4.7)$$

where s and t are parametric parameters and the $x_{k_\alpha} = [x_{k_\alpha}\ y_{k_\alpha}\ z_{k_\alpha}]$. If s_1 and t_1 are defined as the parametric coordinates at which the distance between the lines is minimized then a vector w can be defined as

$$w = L_1(s_1) - L_2(t_1) = (x_{1_i} - x_{1_j}) + s_1 u - t_1 v$$
$$= w_1 + s_1 u - t_1 v \qquad (4.8)$$

which will be perpendicular to both lines meaning that the dot products between w and u and v will be zero

$$w \cdot u = 0 \text{ and } w \cdot v = 0. \qquad (4.9)$$

Substituting w into these relations the values of s_1 and t_1 to be found as

$$s_1 = \frac{(u \cdot v)(w \cdot v) - (v \cdot v)(w \cdot u)}{(u \cdot u)(v \cdot v) - (u \cdot v)^2} \qquad (4.10)$$

$$t_1 = \frac{(u \cdot u)(w \cdot v) - (u \cdot v)(w \cdot u)}{(u \cdot u)(v \cdot v) - (u \cdot v)^2}. \qquad (4.11)$$

As a result of these equations, if the denominators are zero then the two lines are parallel and the distance between the rods is simply the distance between the end points. If the values of both s_1 and t_1 are between 0 and 1 (i.e. on the rod) then the distance is calculated as $|w|$. However, if

either of the values are greater to 1 or less than zero, the end point associated with the line of the

rod are used to recalculate the minimum distance between the rods. This is done by minimizing

the length of w which is the same as minimizing $|w|^2$ [33]. Setting the first derivatives with

respect to s and t of $|w|^2$ to zero allows relations:

$$\frac{\partial |w|^2}{\partial t} = 0 = -2v \cdot (w_1 + su - tv) \tag{4.12}$$

$$\frac{\partial |w|^2}{\partial s} = 0 = 2u \cdot (w_1 + su - tv). \tag{4.13}$$

From these relations, the minimum point can be found by first seeing if the s coordinate is greater

than one or less than zero. In the former case, s is set to one in the latter, s is set to 0 and the first

relation (Eqn. 4.12) is used to find the new corresponding value of t. Then in a similar manner,

the t value is checked to see if it is greater than one or less than zero. Similarly to s, the value is

set to the appropriate boundary (0 or 1) if it falls outside of this range. If this occurs, then the

second relation is used to see if the s value should change. When using the second equation (Eqn.

4.13), if the value of s is again bounded by zero and one. Once the final values of s and t are

computed, the distance between the rods is calculated by finding the length of the vector **w**. If this

length is less than two times the radius, then the rods are considered to overlap and the rod will

not be placed. A figure showing a generated mesostructure of the entire domain is presented in

Figure 4.17 (a) and the initial mesostructure used in the computational study is shown in Figure

4.17 (b). Using this method of rod placement, a local volume fraction of 0.28 of W rods in the

area where the simulation was conducted was obtained. It should be noted that this procedure

generally results in global mesostructures with 0.20 to 0.25 volume fractions.

The drop weight simulations of the drop weight tests for the three dimensional

mesostructure was conducted using the Eulerian finite element method that was implemented in

LS-DYNA. As with the two dimensional simulations, the materials were modeled using the

Johnson-Cook constitutive model in conjunction with the Grüneisen equation of state. The

Eulerian background mesh size was chosen such that 100 elements spanned each direction of the computational domain. Symmetry boundary conditions were imposed on the bottom and three of the side boundary planes of the mesostructure, the remaining side boundary did not have a constraint on it and allowed material to freely move out of the computational domain. A constant velocity of 10 m/s was imposed on the top boundary to maintain consistency with the previous simulations and experimental test.

(a)   (b)
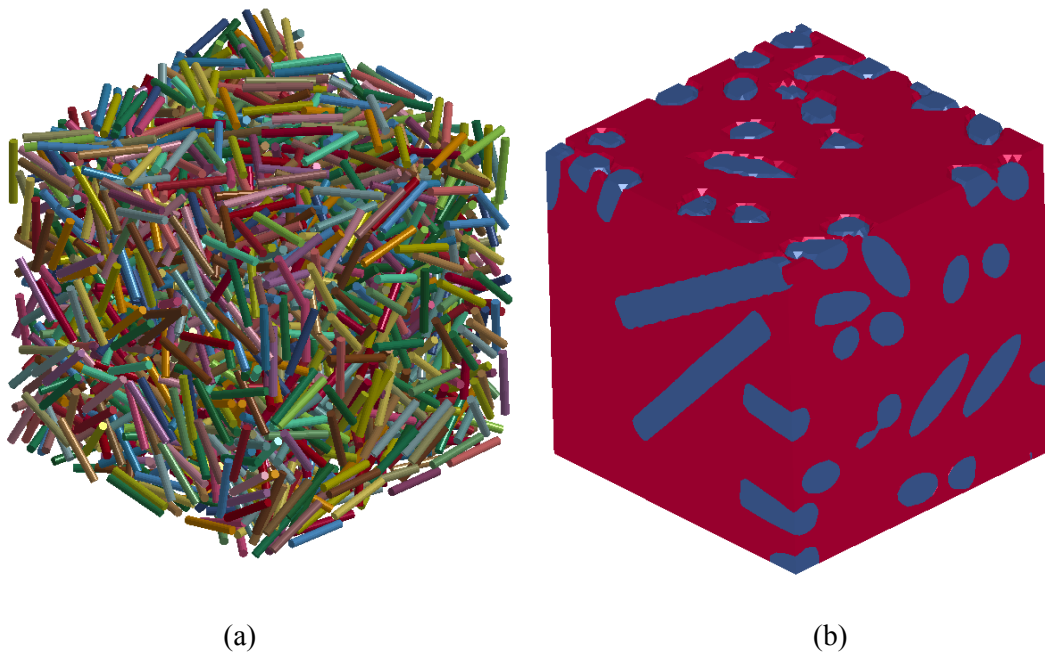
Figure 4.17 – (a) The locations of the W rods generated for the mesostructure used in simulations for the drop weight tests. The generated domain was 2 cm x 2cm x 2cm and the central region of the domain was used for computation of the drop weight test. (b) The initial mesostructure used in the simulation of the drop weight test with W rods (4mm length, 200 micrometer diameter) shown in blue in a solid matrix of Al (red).

The results of the simulation is presented in Figure 4.18 and demonstrate that the rods act to direct the shear band in a similar fashion as the two dimensional simulations. Additionally, as seen in the previous simulations, a single global shear band initially forms with a direction nearly 45 degrees to the loading direction (in the plane of maximum shear) before subsequent shear

bands develop. As with the simulations examining the influence of the mesostructure (see Figure 4.14) there is a slight shifting of the W rods in the early stages of the deformation which may result in the generation of channels that are favorable to the formation of the shear band. It should be noted that the size degree of relative shift between the material regions on either side of the shear band is qualitatively smaller in the three dimensional simulations. This is likely due to the additional geometrical locking or caging that occurs as a result of the interaction of the rods. Finally, due to the similarities between these three dimensional simulations and the analogous simulations, these simulations give additional confidence in the assumptions used in the two dimensional simulations previously conducted in this chapter.

(a)   (b)

(c)   (d)
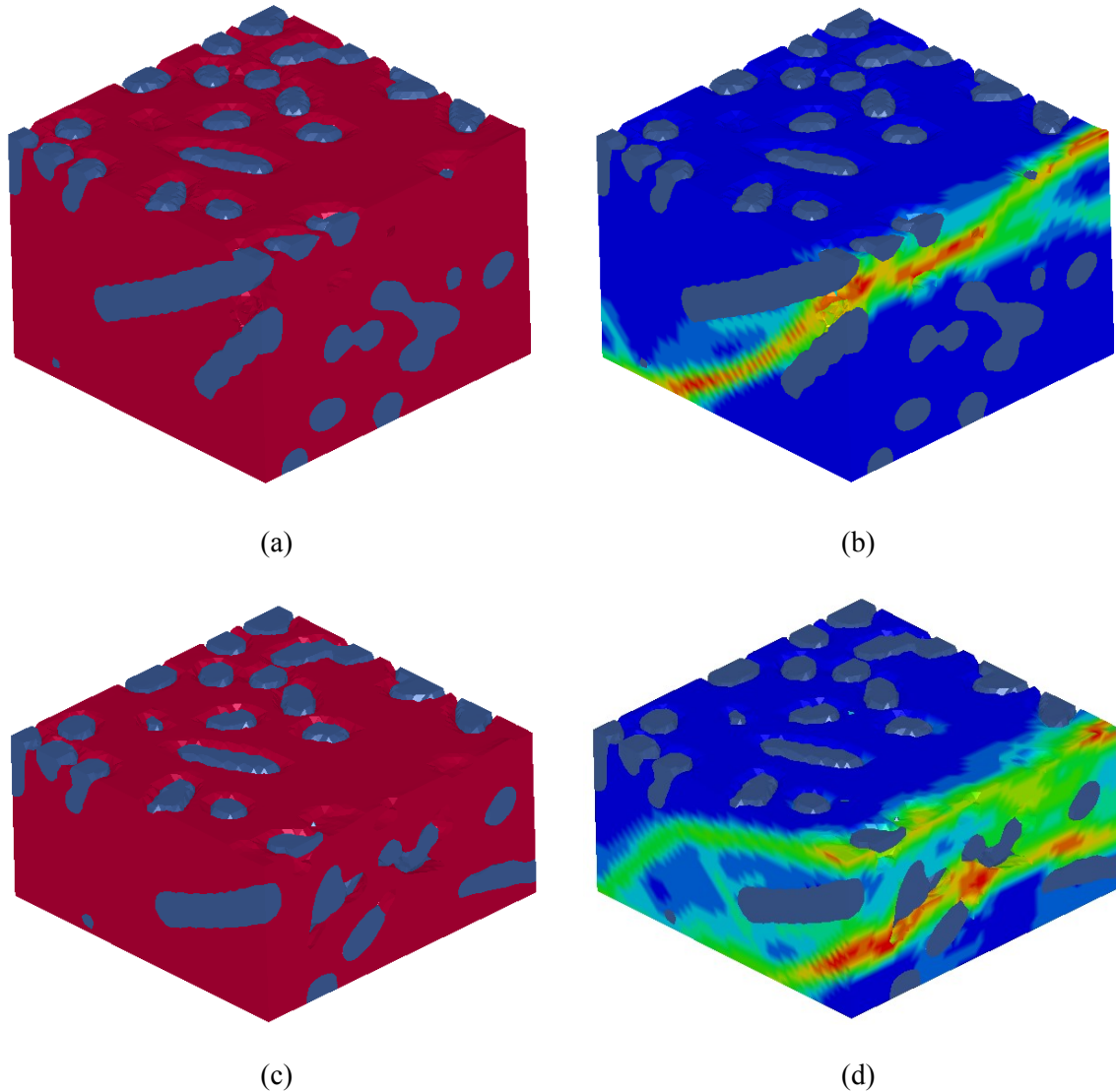
Figure 4.18 – Results of the drop weight simulation with W rods and solid Al matrix at 0.30 (a) and (b) and 0.50 (c) and (d) global strain. The deformed mesostructure is presented in (a) and (c) and the fringe of the damage is plotted in (b) and (d) where areas in red are fully damaged and areas in blue have no damage.

4.5 Chapter conclusions

Dynamic experiments with Al-W granular/porous composites and numerical simulations revealed the characteristics that had the greatest effects on shear instability and shear band formation. It was shown that in simulated CIPed only (non-bonded) samples the Al and W particles rearranged themselves during the dynamic deformation to effectively block shear

localization. This resulted in the subsequent bulk disintegration of the sample in agreement with areas near the outer surface of the samples used in the experiments.

All CIPed+HIPed (bonded) samples exhibited shear localization and shear band formation. The shear bands nucleated during the initial stages of the deformation in Al surrounding the W particles and spread to the nearby W particles at angles close to 45 degrees. The shear band is kinked by W particles causing the shear band path to deviate from the ideal 45 degree angle path dictated by global geometry. In simulations with relatively larger W particles, the path of the shear band was influenced to a greater degree than simulations with the similar sized W and Al particles due to increased heterogeneity of the sample. It was also shown that variations in the initial arrangements of the W particles were the main drivers determining where the global shear bands formed in the sample. Numerical calculations and experiments revealed that the mechanism of shear localization in granular composites is due to a localized high strain flow of Al around rigid W particles, causing local damage accumulation and a subsequent growth of the meso/macro shear bands/cracks.

A variety of constraint boundary conditions were examined to represent the heterogeneous nature of the internal structure in the global sample. Each simulation showed shear localization occurred between the nearby W particles while leaving areas away from the W particles relatively undeformed. This result is supported by the microstructural features observed in the experimental sample.

Finally, the role of the constitutive behavior in the Al was examined in numerical calculations. The results showed that a significant reduction of the initial yield stress from Al 6061-T6 (324 MPa) to a softer Al (20 MPa) increased the amount of bulk distributed damage and plastic strain in the sample in addition to altering the shear band location. Removal of thermal softening in constitutive equation did not significantly change the shear instability in granular

composites pointing to the damage accumulation caused by the local high strain flow of the Al around the W particles as a main softening mechanism triggering shear localization.

This chapter contains material that appears in the Journal of Applied Physics article K.L. Olney, P.-H. Chiu, C.-W. Lee, V.F. Nesterenko, and D.J. Benson, J. Appl. Phys. 110, 114908 (2011). The dissertation author was the primary author of this paper.

4.6 Chapter references

[1] R. Ames, Multi-functional Energetic Materials, *MRS Proc*. **896**, 123 (2006).

[2] J. J. Davis, A. J. Lindfors, P. J. Miller, S. Finnegan, and D. L. Woody, *11th Det. Symp. (Int.)* 1007 (1998).

[3] W. Holt, W. Mock, Jr., and F. Santiago, *J. Appl. Phys*. **88**, 5485 (2000).

[4] C. R. Siviour, M. J. Gifford, S. M. Walley, W. G. Proud, and J. E. Field, *J. Mater. Sci*. **39**, 1255 (2004).

[5] J. E. Balzer, C. .R Siviour, S. M. Walley, W. G. Proud, and J. E. Field, *Proc. R. Soc. London* **781**, 460 (2004).

[6] J. W. Mock and J. Drotar, *AIP Conf. Proc*. **955**, 871 (2007).

[7] J.C. Foster Jr., J. Glenn, and M. Gunger, *AIP Conf. Proc*. **505**, 703 (2000).

[8] S. Bardenhagen and J. Brackbill, *J. Appl. Phys*. **83**, 5732 (1998).

[9] K. Roessig, J. J.C. Foster, and S. Bardenhagen, *Exp. Mech*. **42**, 329 (2002).

[10] J. Cai, S. Walley, R. Hunt, W. Proud, V. Nesterenko, and M. Meyers, *Mat. Sci. Eng. A* **473**, 308 (2008).

[11] J. Cai, V. Nesterenko, K. Vecchio, F. Jiang, E. Herbold, D. Benson, J. W. Addiss, S. M. Walley, and W. G. Proud, *Appl. Phys. Lett*. **92**, 031903 (2008).

[12] E. Herbold, V. Nesterenko, D. Benson, J. Cai, K. Vecchio, F. Jiang, J. W. Addiss, S. M. Walley, and W. G. Proud, *J. Appl. Phys*. **104**, 103903 (2008).

[13] J. Cai and V. F. Nesterenko, *AIP Conf. Proc*. **845**, 793 (2006).

[14] J. Addiss, J. Cai, S.Walley, W. Proud, and V. F. Nesterenko, *AIP Conf. Proc*. **955**, 773 (2008).

[15] J. Cai, F. Jiang, K. Vecchio, M. Meyers, and V. Nesterenko, *AIP Conf. Proc*. **955**, 723 (2008).

[16] E. Herbold, J. Cai, D. J. Benson, and V. Nesterenko, *AIP Conf. Proc.* **955**, 785 (2008).

[17] P-H. Chiu and V. F. Nesterenko, *DYMAT* (EPD Sciences, 2009) pp. 947–953

[18] P-H. Chiu, S. Wang, E. Vitali, E. B. Herbold, D. J. Benson, and V. F. Nesterenko, *AIP Conf. Proc*. **1195**, 1345 (2009)

[19] C. Zener and J. H. Holloman, *J. of Appl. Phys*. **15**, 22 (1944)

[20] J. Lomonds and A. Needleman, *Mech. of Materials* **5**, 339 (1986)

[21] Y. Yang, H.G. Zheng, Z.J. Shi, and Q.M. Zheng, *Mat. Sci. and Eng. A* **528**, 2446 (2011).

[22] Q. Xue, V.F. Nesterenko, and M.A. Meyers, *Mat. Sci. and Eng. A* **384**, 35 (2004)

[23] Q. Xue, V.F. Nesterenko, and M.A. Meyers, *Int. J. Impact Eng***. 28**, 257 (2003)

[24] V. Nesterenko, M. Meyers, and H. Chen, *Acta mater.* **44**, 4037 (1996)

[25] C. Shih, M. Meyers, and V. Nesterenko, *Acta mater.* **46**, 4037 (1998)

[26] D. J. Benson, Comp. Methods in Appl. Mech. and Eng. **99**, 235 (1992)

[27] E. Vitali and D. J. Benson*, Int. J. Numer. Meth. Eng.* **67**, 1420 (2006)

[28] W. H. Cook, G. R. Johnson, *Eng. Frac. Mech*. **21**, 31 (1985)

[29] T. J. Holmquist, D. W. Templeton, and K. D. Bishnoi, *Int. J. Impact Eng*. **25**, 211 (2001)

[30] D. J. Steinberg, *Equation of states and strength properties of selected materials*, Tech. Rep. (Lawrence Livermore National Lab, 1996).

[31] L. Westerling, P. Lundberg, and B. Lundberg, *Int. J. Impact Eng*. **25**, 703 (2001)

[32] V. Nesterenko, *Dynamics of Heterogenous Materials* (Springer, NY, 2001) Chap. 6.

[33] P. Schneider and D. H. Eberly, *Geometric Tools for Computer Graphics* (Elsevier, CA, 2003) Chap. 10.

Chapter 5

Mechanisms of fragmentation and the microstructure of debris generated during explosively expanded Al-W granular composite rings

5.1 Chapter introduction

Control and understanding of the fragmentation processes of granular/porous reactive materials is important for optimizing their performance [1, 2]. Despite having a large combustion energy (7422 cal/g), to attain achieve oxidization on a timescale of approximately 1 millisecond (appropriate for blast loading events in munitions), Al needs to be pulverized into particles with sizes less than 20 microns [3]. Explosively loaded homogeneous materials (such as standard engineering metals like aluminum and steels) demonstrate that the characteristic size of the fragments is much larger (of the order 1-10 mm) due to the nature of the fragmentation mechanisms of homogeneous materials [4, 5]. Using a highly heterogeneous material composed of components with drastically different densities and shock impedances (e.g., Al and W) can provide enhanced pulverization due to addition of mesoscale fragmentation mechanisms [6, 7]. In this research, Al-W granular/porous composite rings with different mesostructures were prepared

and tested in explosively driven expanding ring experiments. Numerical simulations were used to gain an insight into the development of these mesoscale fragmentation mechanisms during dynamic loading.

5.2 Explosively driven fragmentation experiments

Al-W granular/porous composite rings (24% Al and 76% W by weight, and 69% and 31% by volume correspondingly, and a theoretical density of 7.8 g/cm3) with 4 mm height, 30 mm outer diameter and 22 mm inner diameter were prepared by Cold Isostatic Pressing (CIPing) at 345 MPa. The mesostructure of the samples were tailored by using different particle sizes of Al powder (coarse: -325 mesh and fine: 4.5~7 μm, both from Alfa Aesar), and different morphologies of W (powder: -325 mesh with polyhedral particles from Alfa Aesar and W rods: 200 μm diameter with 4 mm length from A-M system). We consider that the elongated geometry of W rods may influence the pulverization process of Al due to differences in the dynamic behavior of rods in comparison to particles during fragmentation process. To investigate the role of bonding between Al particles, half of the samples were Hot Isostatically Pressed (HIPed at pressure 100 MPa and temperature 450C) after CIPing. Samples were pressed to correct dimensions with 8~15% porosity and did not require further machining. Three smaller rings (19 mm outer diameter and 13 mm inner diameter) with the same height were made from a mixture of fine Al and W powders (CIPed only) and were used in pilot experiments. For comparison, solid rings with similar sizes and densities were manufactured from stainless steel 304.

The explosively driven fragmentation tests were conducted in the Cavendish Laboratory, Cambridge University, UK. The samples were placed around a Cu tube. The explosive charge (Primersheet 1000 discs) was placed inside the Cu tube and initiated by either a hollow end Nobel No. 6 detonator or a RP501 detonator made by Teledyne. Photon Doppler Velocimetry (PDV or Het-V) with nominal 140A laser output was used to capture the time-resolved expansion velocity.

Paraffin wax (for homogeneous samples) or polyethylene glycol (for granular/porous samples) was used for the soft capture of fragments. Details regarding the experimental setup can be found in [8]. PDV records corresponding to the small ring samples and results of numerical simulations are shown in Figure 5.1 (a).

PDV records corresponding to samples made with W rods are shown in Figure 5.2 (a). It is difficult to distinguish between the PDV traces of samples with different morphologies of Al and bonding. This suggests that the global response of these composites with W rods under this loading condition is not very sensitive to the Al particle size or their bonding. X-ray Diffraction (XRD) was performed on the recovered fragments (Figure 5.2 (b)) and demonstrated that intermetallic reaction did not occur during the dynamic loading. In all samples, Al particles were stripped from the W rods. The particle size analysis of the recovered fragments excluding the W rods (Figure 5.2 (c) and (d)) showed that nearly all (90-98%) of the fragments were smaller than 100 microns. This is significantly smaller than the fragments generated from solid SS304 samples with similar density [4]. In addition, an increase in the amount of small size fragments in comparison with size distribution in initial powders was observed. For example, the percentage of fragments with a size less than 10 microns in the sample with the coarse Al powder samples grew from 22% (initial) to 28-35% (after test) and the number of fragments with a size smaller than 4.5 microns in the samples with fine Al powder grew from 8% (initial) to 11-15% (after test). This may indicate that some Al particles were fractured during the tests.
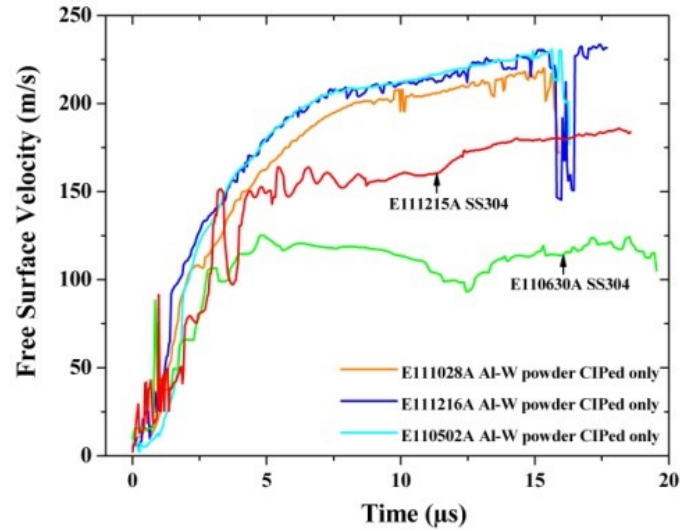
(a)
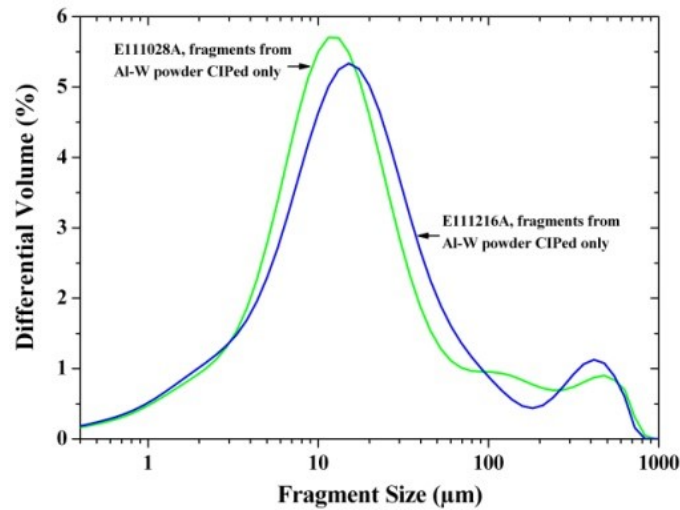
(b)

Figure 5.1 - (a) The PDV records of the small ring tests with SS304 and the CIPed Al-W samples with fine Al/coarse W powder as well as results of numerical simulations of Al/W samples; and (b) the particle size distribution of the recovered fragments from the fine Al/coarse W powder composite samples. The heterogeneous Al-W samples with non-bonded Al particles demonstrated a consistent behavior in expansion velocity. Particle size analysis of the recovered fragments for the small ring Al-W samples was performed using laser diffraction is presented in (b). This showed that about 90% of fragments were smaller than 100 microns compared to the characteristic fragment size of several millimeters in the stainless steel samples.
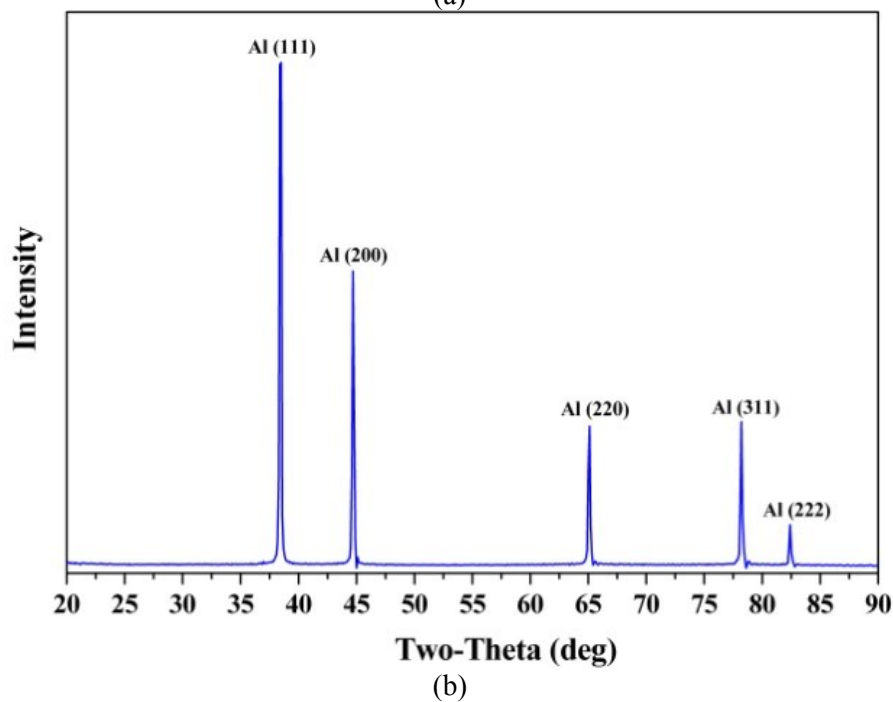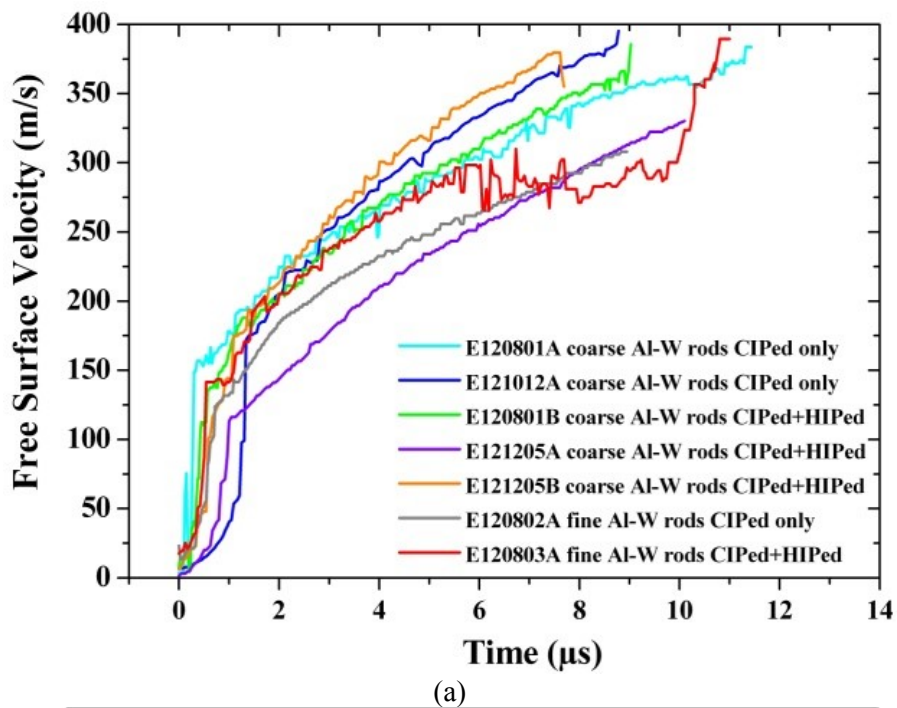
(a)

(b)

Figure 5.2 - (a) The PDV records of samples with Al powder and W rods show similar free surface velocity profiles in all samples. (b) The XRD results of recovered fragments indicated that no intermetallic reaction occurred during tests. The fragment size distribution of the recovered fragments from samples with W rods and (c) coarse (d) fine Al powder (d).
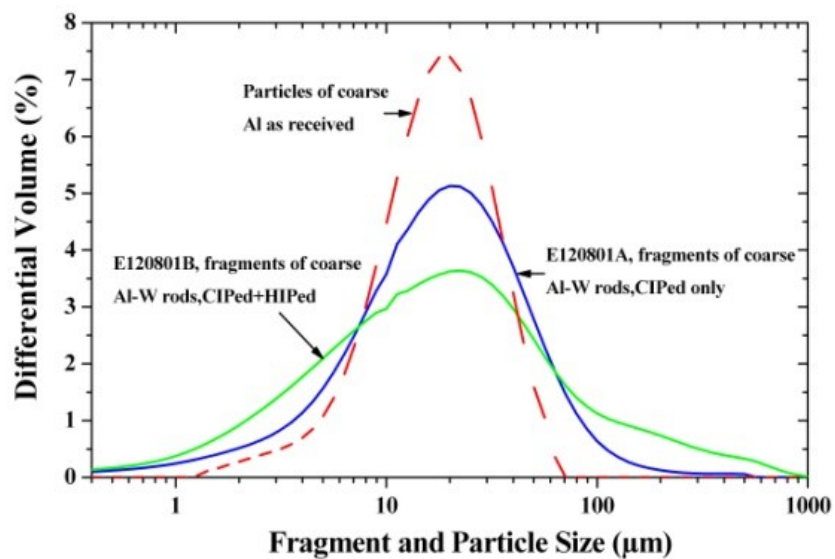
(c)
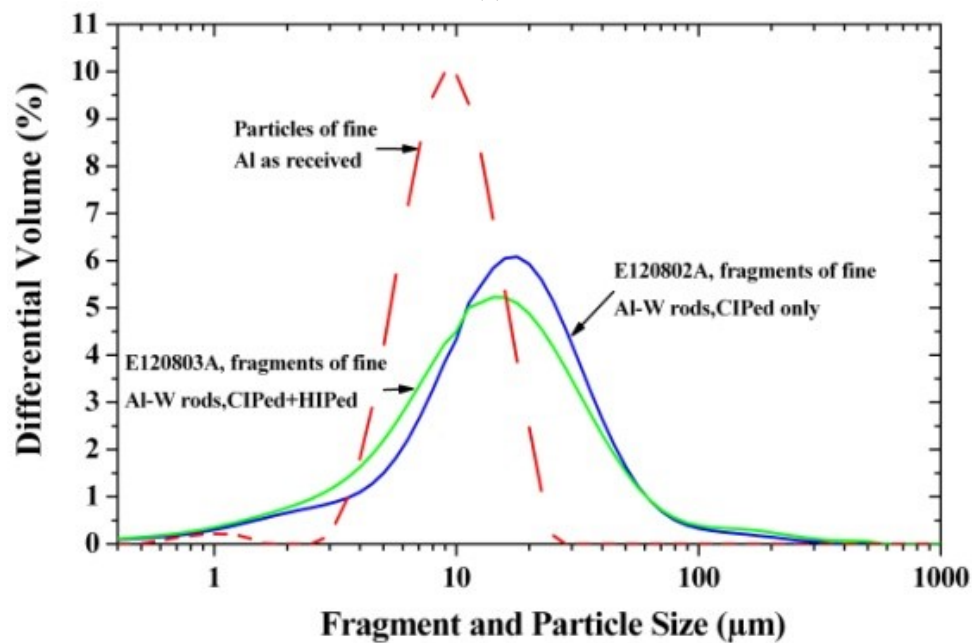
(d)

Figure 5.2 - (a) The PDV records of samples with Al powder and W rods show similar free surface velocity profiles in all samples. (b) The XRD results of recovered fragments indicated that no intermetallic reaction occurred during tests. The fragment size distribution of the recovered fragments from samples with W rods and (c) coarse (d) fine Al powder (d). (Continued from previous page.)

Scanning Electron Microscopy (SEM) was utilized to examine the mesostructure of Al-W granular/porous composite rings before the dynamic test and fragments after the test. Figure 5.3 (a) demonstrates that particles in the fine Al/coarse W powder sample after the CIPing process mostly retained their as-received shape (slightly deformed spheres for Al and polyhedrons for W). Figure 5.3 (b) shows a large recovered fragment polished and mounted in epoxy. Fragments of this size consist of agglomerated Al and W particles. In places there is some elongation of the low strength Al particles between high strength neighbouring W particles. This suggests that the Al particles underwent plastic deformation during the dynamic loading by either the extrusion of Al between the W particles, or the squeezing of the Al by the W particles. In some instances, the elongated Al particles appear far from W particles. A similar phenomenon of localized plastic flow of Al particles was observed in samples with W rods. It should be emphasized that in the samples with Al powders and the W rods, the Al particles did undergo small alterations to their shape after CIPing and HIPing (see Figure 5.3 (c)), but were heavily dynamically deformed locally during the tests as shown in Figure 5.3 (d). The extrusion of the Al matrix between W particles or rods may assist in the creation of fresh surfaces on the Al particles hence improving their oxidation and subsequent combustion efficiency. Recovered fragments from samples with different Al particles sizes and/or bonding conditions in Al matrix were very similar.
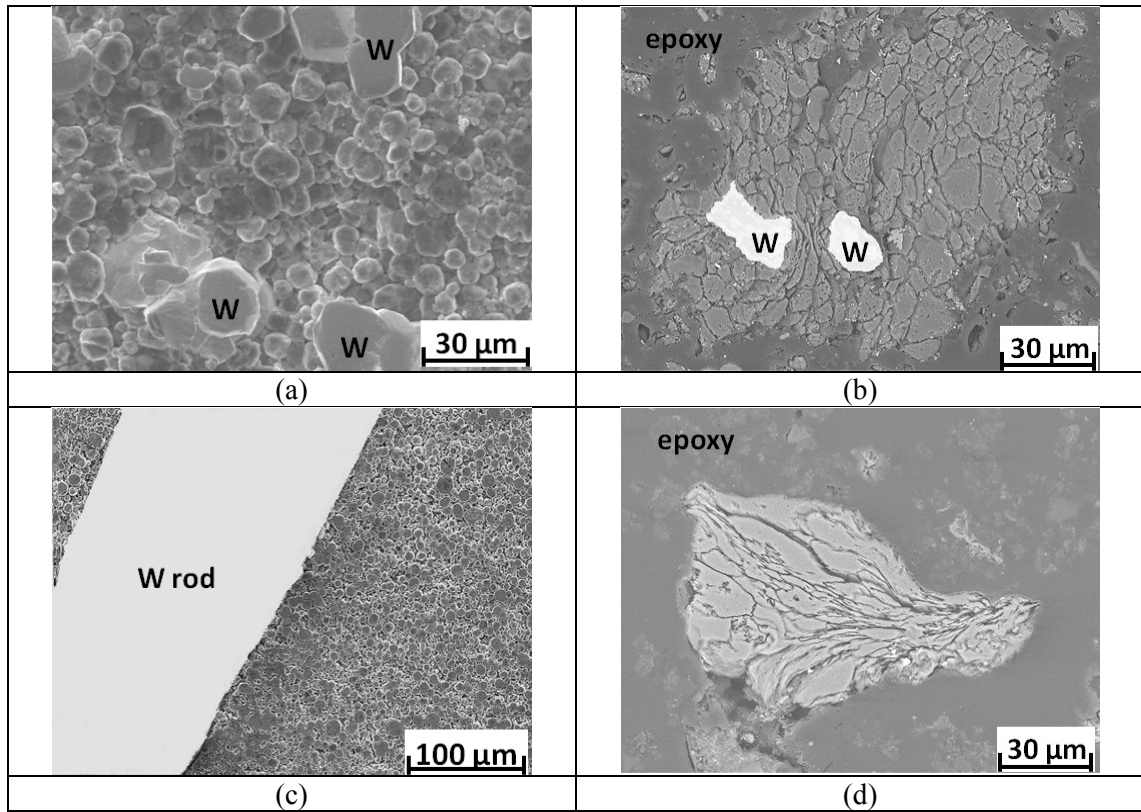
Figure 5.3 - SEM images of CIPed only fine Al/coarse W powder sample (a) and fine Al/W rod sample (c) before the test, and images of corresponding fragments after the dynamic testing of the samples is in (b) and (d) respectively.

5.3 Numerical modeling

Two dimensional finite element simulations using LS-Dyna were performed to examine the mechanisms of fragmentation during the explosively driven expansion of the granular composites. A 10 degree wedge of the sample was simulated under plane strain conditions. The mean size of all of the particles (Al and W) was assumed to be the same, 40 micrometer diameter. These assumptions were imposed due to computational limitations. The individual particles were created by using a Voronoi tessellation of the region. The volume fractions of the components were kept similar to the experiment (30% W, 70% Al). The mesh resolution for the Al and W particles was chosen such that ~5 elements spanned the diameter of the particle to adequately capture the stresses in the particle. The initial mesostructure is presented in figure 4 (a). Since the

experimental samples showed no bonding between the particles after the CIPing processing (particles in the samples were held together due to mechanical interlocking), no metallic bonding was introduced in numerical simulations and the particles were allowed to slip and separate.

The behavior of solid Al, Ni, and Cu was modeled using the Johnson-Cook constitutive model [9] in conjunction with the Grüneisen equation of state. The material parameters were taken from the literature [9,10]. To model the explosive driver, we assumed that the detonation was instantaneous in the plane of interest since detonation speed is much larger than the velocity of expansion. The detonation products were modeled as a polytropic gas with the initial pressures/energies of the detonation products described by conditions at the Chapman-Jouguet point similar to [6]. The corresponding line in the Figure 5.1 (a) shows that the free surface velocity of the expanding ring from the simulation is in good agreement with experimental data. Differences in the initial 3 microseconds of velocity may be accounted for due to the geometry of the experimental setup allowing additional axial expansion of the detonation products "softening" the initial shock loading in comparison to the plane strain conditions. Evolution of sheared zones and generation of fragments with agglomerated Al particles are shown in Figure 5.4 (b), (c) and (d). Sheared zones first initiate at about 45 degrees from radius and are kinked by clusters of W particles (Figure 5.4 (b) and (c)). As the ring expands, tension in the hoop direction causes the sheared zones thicken due to the difference in corresponding particle velocities of neighboring areas (Figure 5.4 (b)). Regions outside of the sheared zones are possible areas where larger size agglomerated fragments are created.
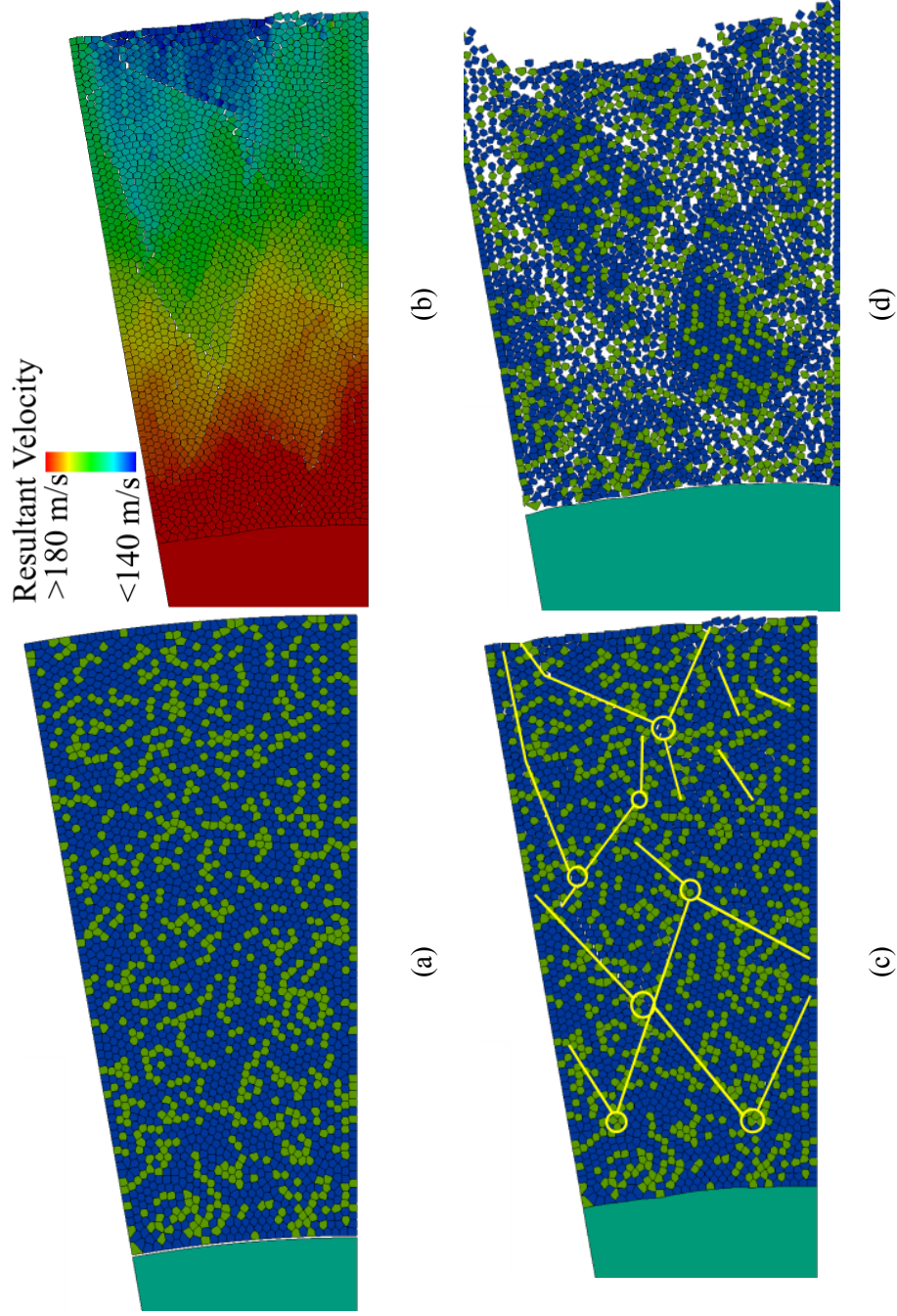
Figure 5.4 - (a) The initial mesostructure used in the finite element simulations with W particles shown in green and Al particles shown in blue. (b) Particle velocity distribution demonstrating the jumps in planes with 45 degrees to radius separating the areas with uniformly distributed particle velocity. (c) The yellow lines identify the jumps in particle velocity shown in (b) kinked by W particle clusters (shown by circles). (d) Tension in hoop direction allows the sheared zones to thicken

5.4 Chapter conclusions

Explosively driven fragmentation experiments were conducted with Al-W porous/granular composite rings with the goal of examining the mechanisms of fragmentation, characteristic fragment sizes and variations of these with respect to the mesostructure (coarse Al vs. fine Al particles, W powder vs. W rods, and bonded vs. unbounded Al particles). The porous/granular samples were mostly pulverized into fragments sizes below 100 micron (above 90%) for all tested mesostructures. A comparison of initial sizes of particles in the powder and post experiment fragment size distributions indicates that some Al particles may have been fractured during the dynamic loading.

Some of the low strength Al particles were deformed between the rigid W particles, but mainly maintained their equiaxed shape in the areas away from W particles. Al particles were heavily deformed in samples with W rods regardless of the Al particle size and bonding between Al particles. The similar behavior in PDV records for the samples with W rods suggests that the global response is insensitive to the mesoscale properties of the Al (particle size, bonding). In all of the dynamic experiments, there was no observable intermetallic reaction between Al and W in the recovered fragments.

Numerical simulations were performed to examine the mechanisms of fragmentation during explosively driven dynamic loading. Qualitative similarities between the simulations and experiments were observed. The simulations revealed that the creation and development of numerous sheared zones in granular Al matrix may allow fracture of initial Al particles and the generation of micron-sized Al fragments inside them. The spacing between these sheared zones is much larger than the size of the Al and W particles suggesting that material between them is shielded from mesoscale pulverization resulting in the generation of the large scale fragments of agglomerated Al and W particles.

This chapter contains material as it appears in the Journal of Physics: Conference series article P.-H Chiu, K.L. Olney, C. Braithwaite, A. Jardine, A. Collins, D.J. Benson, and V.F. Nesterenko, J. Phys.: Conf. Series, 500, 112017 (2014). The dissertation author was an investigator and coauthor of this paper.

5.5 Chapter references

[1] R.G. Ames, *Mat. Research Soc. Symp. Proc*. **123**, 0896-H03-08.1 (2006).

[2] J.P. Hooper, *J. Appl. Phys*. **112**, 043508 (2012).

[3] K.L. Olney, P.H. Chiu, V.F. Nesterenko, D.J. Benson, C. Braithwaite, A. Collins, D. Williamson, and F. McKenzie, *MRS Proc.* **1521** (2013).

[4] V.F. Nesterenko, P.H. Chiu, C. Braithwaite, A. Collins, D. Williamson, K.L. Olney, D.J. Benson, and F. McKenzie, *AIP Conf. Proc.* **1426**, 533 (2012).

[5] D.E. Grady, *Fragmentation of Rings and Shells: The Legacy of N.F. Mott.* Springer, New York (2007).

[6] K.L. Olney, V.F. Nesterenko, and D.J. Benson, *Appl. Phys. Lett.* **100**, 191910 (2012).

[7] K.L. Olney, P.H. Chiu, C.W. Lee, V.F. Nesterenko, and D.J. Benson, *J. Appl. Phys.* **110**, 114908 (2011).

[8] C. Braithwaite, A. Collins, B. Aydelotte, F. McKenzie, P.H. Chiu, N.N. Thadhani, and V.F. Nesterenko, *Advances in the study of novel energetic materials Proc. 15th Seminar New Trends in Research of Energetic Materials*, Univ. of Pardubice, Czech Republic 93-9 (2012).

[9] G.R. Johnson and W.H. Cook, *Eng. Fract. Mech.* **21**, 31 (1985).

[10] G.R. Johnson and W.H. Cook, *Proc. 7th Int. Symp. on Ballistics* 541 (1983).

Chapter 6

Mechanisms of fragmentation of Al-W granular composites under dynamic loading

6.1 Chapter introduction

Granular materials are used to enhance the release of energy by mixing metal particles, e.g., Aluminum (Al), with traditional energetic materials [1] or by surrounding traditional energetic materials with a granular "shell" [2]. The performance of these composite energetic materials is heavily influenced by the particle size of the metal powder which dictates the speed at which these particles can be oxidized by the detonation products or by the surrounding air [1-3]. It has been shown that small sized suspended Al particles (40 μm) in air can sustain a detonation wave caused by the fast energy release due to the oxidization of these Al particles [4]. Impact-initiated energetic materials (metal powders in a polymer binder, consolidated powders, or mixtures of powders) are non-energetic under static or quasi-static loading but release energy under high strain, high strain rate deformations [5-7]. In these materials, the material properties such as the mesostructure and the individual constituents' strength are instrumental in determining the performance characteristics [5].

Another interesting class of reactive materials is granular composite materials that are able to carry a structural load under quasi-static loading combined with the ability to undergo rapid bulk distributed pulverization under dynamic loading, releasing a large amount of usable chemical energy. The performance of these materials is determined by the properties of the individual components and the mesostructure. For example, Al-Tungsten (W) granular composites with an Al matrix are comparable in strength to solid Al and have demonstrated an ability to undergo bulk distributed fragmentation under dynamic loading [8, 9]. The post critical behavior of these Al-W granular composite materials was examined showing that the mesostructure of the W particles was the main factor influencing the fragment size [10-12].

For explosively driven homogeneous expanding rings, the mechanism of fragmentation is determined by the development of macrocracks [13] with a fragment size distribution that can be estimated using the Grady-Kipp equations [14]. The typical fragment sizes for an explosively driven expanding ring made from Al 6061-T6 is on the order of a few mm [11]. Small scale experiments with explosively driven Al-W granular composite rings processed from -325 mesh Al and W particles by Cold Isostatic Pressing (CIPing) were conducted [11]. The recovered fragments demonstrated that the mesostructure of the Al-W composite allowed for the generation of fragments with a size scale on the order of 100 μm. This reduction in the order of magnitude in fragment size suggested that there is a shift in the fragmentation mechanism from the continuum scale to that of the mesoscale determined by the mesostructure of the composite material. This mesoscale mechanism of fragmentation was attributed to the development of gradients in the particle velocities between the Al and the W constituents due to the significant difference between the shock impedances of Al and W.

In this paper, numerical simulations were performed to elucidate the shift in the mechanism from the continuum level determined by the nucleation, propagation and interaction of the macrocracks [13] seen in the homogeneous samples to the generation of fragments which

size is controlled by the mesoscale. The understanding of this mesosclae mechanism may allow for the tailoring of the size of fragments and the reactivity by selecting an appropriate initial mesostructure.

6.2 Description of the simulations

While this system has a 3D architecture, 2D models were used since the trends observed in the 2D simulations that preserve the volume content of the components reflects the dynamic behavior of the 3D heterogeneous materials [15-18]. The mesostructures in the numerical simulations were randomly generated such that the volume content of W (30%) in the composite corresponded to the mesostructures used in previous experiments for Al-W granular composites [8-12]. The shock pressure and temperature seen in the simulations performed in this paper reach conditions [19] that facilitate the bonding between the Al/Al interfaces during shock consolidation. However, the conditions attained during the shock loading do not cause bonding between the Al/W interfaces. As such, the Al particles are assumed to be fully bonded together creating a solid fully dense Al matrix. W particles are embedded into this matrix and are allowed to separate from the surrounding Al matrix. This mesostructure corresponds to a sample that has been processed by CIPing followed by Hot Isostatic Pressing (HIPing) of the granular composite [8-12].

A two-dimensional Eulerian hydrocode [29] that allows for bonding/debonding [21] was used to model the explosively driven granular composite ring during expansion. Each material (Al, W, copper (Cu), and the detonation products) in the sample used separate equations of state and mechanical properties. For Al, Cu, and W, the Johnson-Cook [22] material model with failure was used (equations of this constitutive model are presented in Section 3.2.1 with the material parameters taken from [22-24] and presented in Table 6.1. This material model was used in conjunction with the Mie-Grüneisen equation of state. The explosive was assumed to have an

instantaneous detonation converting the explosive into detonation products. We used this approximation because the focus of our research was on the mechanism of fragmentation of the composite material under similar conditions of loading. The detonation products were modeled as an ideal gas using the Chapman-Jouguet relations for the stationary detonation to obtain the initial conditions as detailed in Section 3.2.3. The initial pressure of the detonation products correspond to the Chapman-Jouguet detonation pressure. The parameters used in this model were calibrated by simulating an explosively driven expanding Cu ring and comparing the free surface velocity with experiments.

Table 6.1 - Constitutive model and equation of state material properties used in the numerical simulations for the Al and W components.

Material parameter	Al 6061-T6 [22, 24]	W[23, 24]	Cu [22, 24]
Johnson-Cook			
ρ_0 [gm cm^{-1}]	2.7	16.98	8.96
G [Mbar]	26.0	1.24	48.0
A [Mbar]	224.0	1506	90.0
B [Mbar]	111.4	176.5	292.0
n	0.42	0.12	0.31
C	0.002	0.0016	0.25
m	1.34	1	1.09
C_p [J kg-1 K-1]	890	130	383
T_{melt} [K]	930	1728	1356
T_{room} [K]	300	300	300
D1	-0.77	0	0.54
D2	1.45	0.33	4.89
D3	-0.47	-1.5	-3.03
D4	0	0	0.014
D5	1.6	0	1.12
Mie-Grüneisen			
C_0 [cm µs^{-1}]	0.52	0.40	0.394
s_1	1.4	1.24	1.489
s_2	0	0	0
s_3	0	0	0
γ_0	1.97	1.67	2.02

The initial mesostructure of the Al-W composite used in the simulations is presented in Figure 6.1. In this paper, four variations of this initial setup were examined to elucidate the influence shock amplitude on the mechanisms of fragmentation. The Cu liner dimensions were identical to the dimensions of the Cu liner used in the experiments presented in [11]. The calculations were performed at two initial pressures of detonation products with parameters corresponding to Primasheet 1000 (a "weak" explosive, used in experiments in [11]): D_{CJ}=0.68 cm/μs, γ_{CJ}= 3, and ρ_{CJ} = 1.46 g/cm^3 resulting in P_1 = 0.168 Mbar and LX-14 (a "strong" explosive): D_{CJ} =0.88 cm/μs, γ_{CJ} = 2.84, and ρ_{CJ} = 1.835 g/cm^3 resulting in P_2 = 0.37 Mbar. The parameters used in this model were calibrated by simulating an explosively (LX-14) driven expanding Cu ring and comparing the free surface velocity with the experiments in [25]. The influence of the Cu inner liner on the mechanisms of fragmentation was also examined.
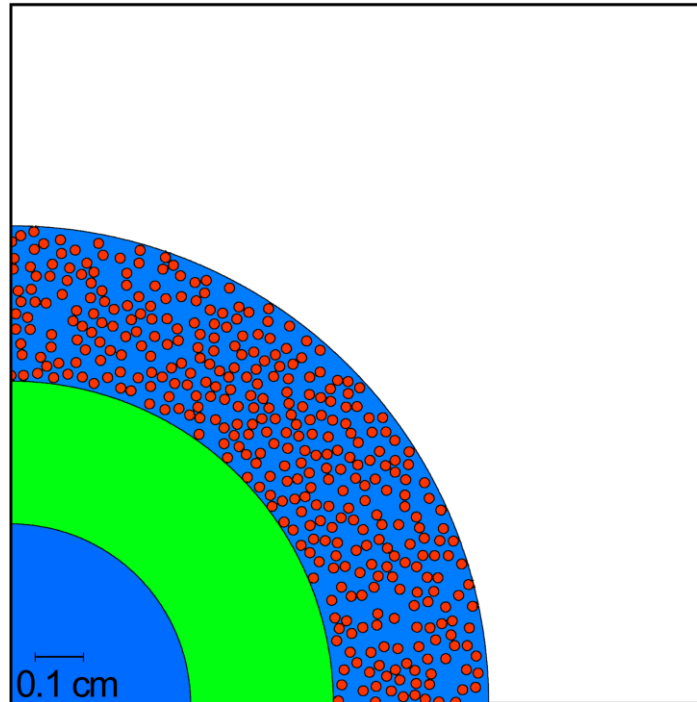
Figure 6.1 – The initial mesostructure for the CIPed+HIPed Al-W granular composite ring with a Cu inner liner. The central blue area represents the detonation products, the second layer (green) is the Cu inner liner, and the outer layer is the granular composite composed of 200 μm diameter W particles (red) embedded in a solid Al matrix (blue). The W particles were randomly placed such that the volume content of W in the composite was 30%. The mesostructure shown for the Al-W composite was used for all of the simulations presented in this paper. For the simulations where the detonation products are in direct contact with the composite ring, the inner Cu liner was removed and replaced with the detonation products.

6.3 Results and discussion of the simulations

Results of the numerical simulations are presented in Figure 6.2 and Figure 6.3. These figures show the fracture patterns in the composite for four configurations that will be referred to as Cases 1-4. The odd numbered cases have the detonation pressure of P_1 and the even cases have a detonation pressure of P_2. Cases 1 and 2 have a Cu inner liner while in Cases 3 and 4 the Cu inner liner replaced with detonation products. Due to the variations in the initial detonation pressures and differences in the subsequent expansion rates, all samples depicted in Figure 6.2

and Figure 6.3 are compared at the same radial expansion (10% and 50% increase in the initial radius).

At 10% radial expansion, velocity gradients between the lighter Al matrix and the heavier W particles have formed due to the initial shock loading and subsequent pressure release from the free surface. The magnitude of the particle velocity gradient shows a strong dependency on the amplitude of the shock loading. This is clearly seen by comparing Case 1 and Case 2: the velocity gradients between the Al and W components are negligible in Case 1 while they are significant in Case 2. In Cases 2-4, the velocity gradients between the Al and W were large enough to cause microjetting to occur within the composite and facilitate the formation of microjets near the vicinity of the free surface. The addition of the Cu inner liner significantly reduced the magnitude of the velocity gradients by reducing the amplitude of the initial shock wave. This is especially dramatic when comparing Case 1 with Case 3 where the addition of the Cu inner liner reduced the velocity gradients between the Al and W such that microjetting did not occur. In Case 2, the added Cu inner liner reduces the magnitude of the velocity gradients by about 20% in comparison to Case 4. This suggests that the addition of the Cu inner liner reduces the effectiveness of the microjetting mechanism and in the cases with weak detonation pressures, causes this mechanism to be inactive. In Cases 2 and 4, these microjets eject approximately 30% of the Al from the composite while no Al ejection was seen in Cases 1 or 3.
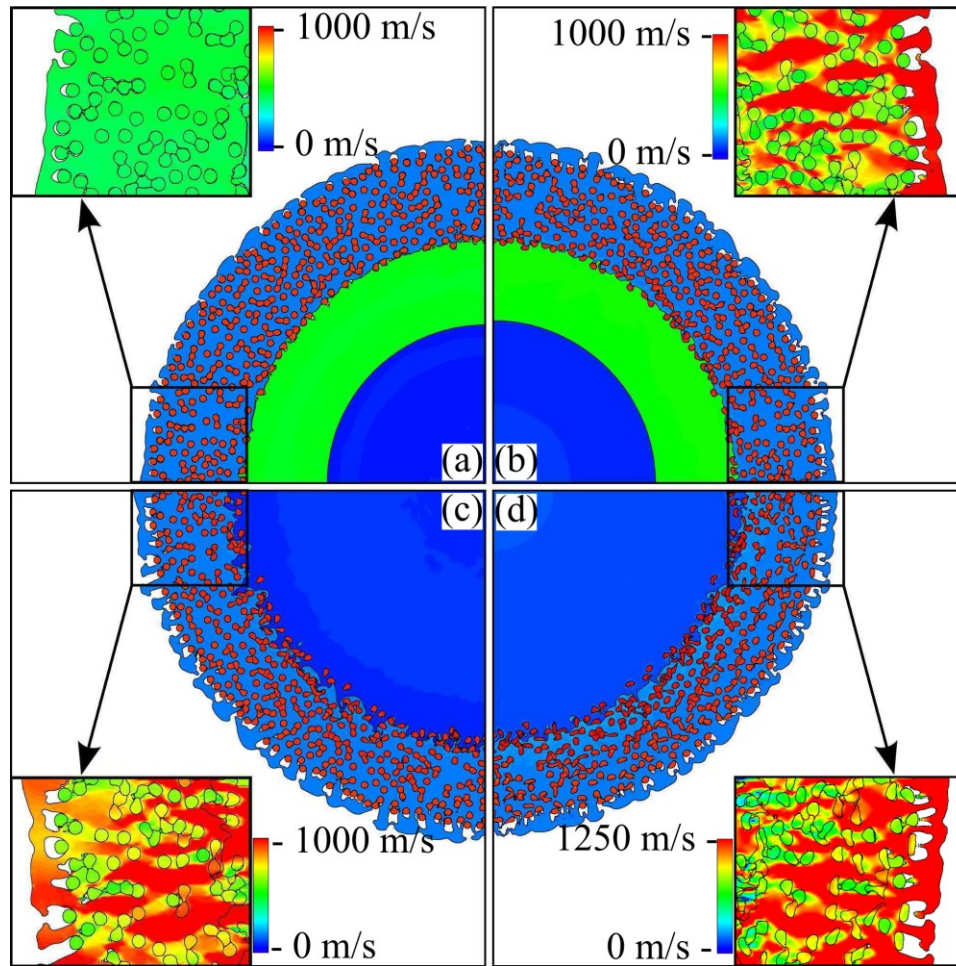
Figure 6.2 - Patterns of mesoscale fragmentation after the granular composite ring has radially expanded by 10% for different initial geometries and detonation product pressures: (a) Case 1, PCJ=0.168 Mbar with a Cu inner liner, (b) Case 2, PCJ=0.37 Mbar with a Cu inner liner, (c) Case 3, PCJ=0.168 Mbar with detonation products in direct contact with the granular composite, and (d) Case 4, PCJ=0.37 Mbar with detonation products in direct contact with the granular composite. Detailed views of the radial velocity in the granular composites are plotted to show the velocity gradients between W particles and the surrounding Al. These velocity gradients are a driving force for mesoscale fragmentation at later stages of expansion.
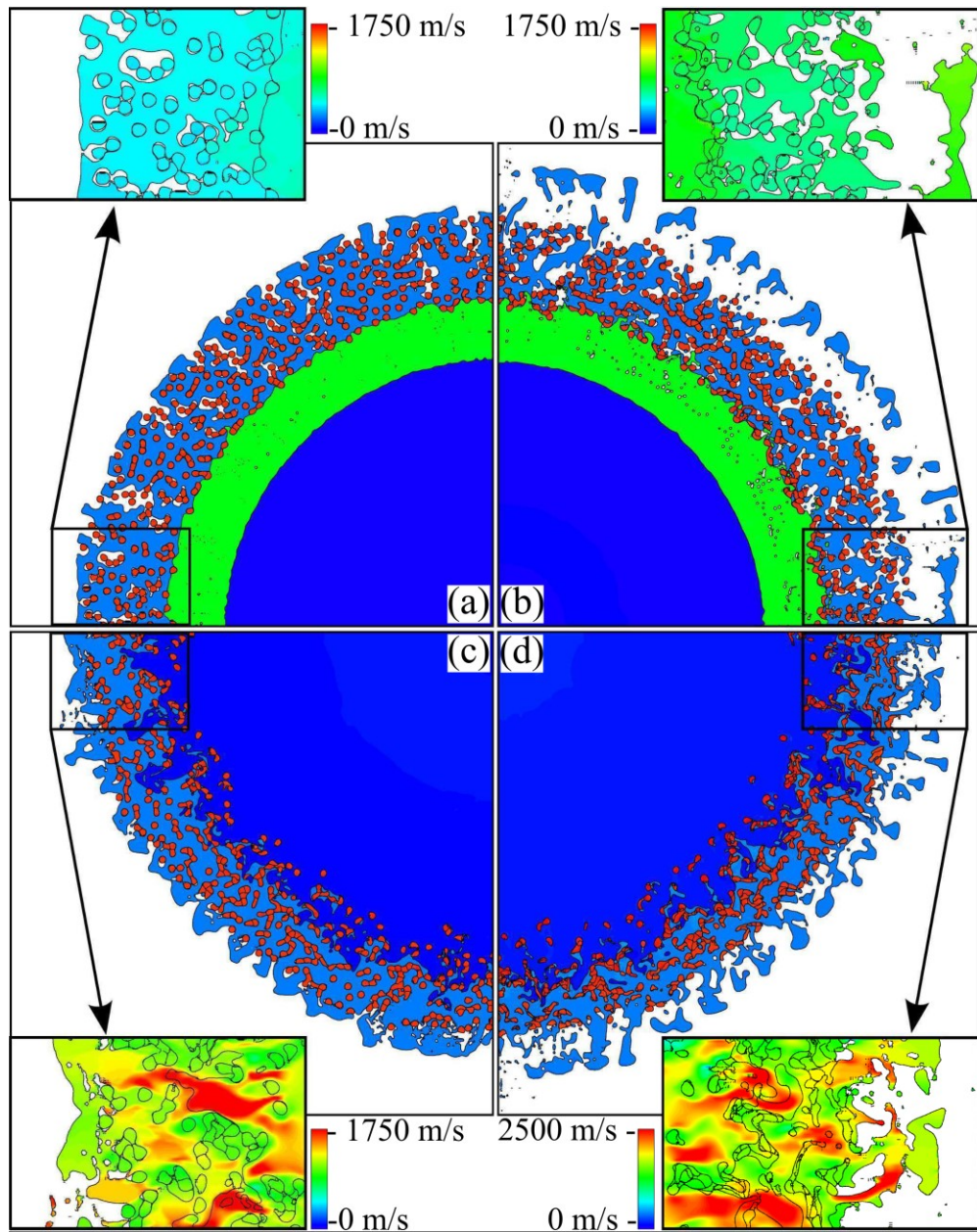
Figure 6.3 - Patterns of fragmentation in the granular composite rings at 50% radial expansion. A previous stage of expansion was presented in Figure 6.2 (a), (b), (c), and (d) corresponding to Cases 1-4 respectively. Detailed views of the radial velocity in the granular composite are plotted to show the equilibration of the velocities between the Al and W constituents at this stage of expansion.

As the ring expands in all cases, the velocity gradients begin to diminish due to shock wave equilibration and dissipation. The rate at which this equilibration occurs is largely dependent on the shock amplitude and the shock impedances of the components. As the particle velocity gradients diminish, the mesoscale microjets cease to exist. This results in a shift in the mechanism of fragmentation from the ejection of Al due to gradients in the particle velocity to the competition between the continuum scale development of macrocracks and the networks of microcracks developing on the mesoscale between neighboring W particles and in heavily damaged areas where Al flows around the relatively rigid W particles [12].

Figure 6.3 depicts the samples after expanding 50% of the initial radius. It is clear from this figure that the differences in the detonation products create qualitatively different fracture patterns in the composite material. In Case 1, potential fragments are forming with a similar size scale as those predicted by the Grady-Kipp equations. In Case 2, the composite shows a large number of mesoscale voids opening around the W particles and their coalescence with nearby voids. The W particles in these regions exhibit a tendency to form clumps of 5-10 particles. This suggests that a subsequent fragments will be generated on a smaller size scale containing about 5-10 W particles.

In the simulations without the Cu inner liner, the W particles were heavily deformed. Furthermore, in the regions of the composite near the detonation product interface, the Al matrix was stripped from the W particles leaving free W particles behind. In these cases, the detonation products penetrate into the composite where the Al material is fully damaged, resulting in a Rayleigh-Taylor type instability. These instabilities grow into the composite, channeled by clumps or short chains of W particles, creating "fingers" of detonation products that introduce an additional size scale of fragmentation based on the mesoscale. The paths of these "fingers" start in the same location on the inner Al-W composite ring but the penetration depth at a given radial expansion is determined by the detonation pressure.

The amplitude of the initial shock wave, dictated by the pressure of the detonation products, determines the mechanism of pulverization for the Al in the granular composite. At low detonation pressures, generating relatively low amplitude shock waves, the disintegration is mainly determined by the competition between the continuum Grady-Kipp mechanism of macrocracking and the opening of mesoscale voids due to the Al/W interfaces that are initially not bonded due to local tensile strains when the composite radially expands. The continuum type of spall in the radial direction is mitigated by the complex pattern of shock interactions resulting in a desirable mesoscale type of spalling/jetting. At higher detonation pressures that generate larger amplitude shock waves, a third fragmentation mechanism develops; the mesoscale jetting due to the large gradient of particle velocities between the W and Al in the regions adjacent to the free surface. This mechanism is responsible for the pulverization of approximately of 30% of Al. The remainder of the composite is pulverized at later stages of expansion when the gradients in the velocity between the Al and the W vanish due to wave equilibration. This pulverization is based on the competition between the mechanisms of macrocracking and the opening of the mesoscale voids at the Al/W interfaces. In the cases where the Cu inner liner was not present, the detonation products penetrated into the composite generating an additional mesoscale mechanism of fragmentation based on the mesostructure. The scale of the fragments come from the self-organization of macrocracks starting with an opening of the existing microcracks and damage localization of Al due to the complex strain and strain rate fields caused by the random distribution of W particles [12]. These mesoscale mechanisms can be used to tailor the size of the fragments (macro to mesoscale) by selecting the appropriate initial mesostructure. At relatively low shock pressures, the initially non-bonded interfaces between particles may be the most important mesostructural factor governing the size of the fragments while at higher detonation pressures, the mesoscale jetting can be the most important factor for pulverization.

6.4 Chapter conclusions

Numerical simulations of Aluminum (Al) and Tungsten (W) granular composite rings under various dynamic loading conditions due to explosive loading were performed. Three competing mechanisms of fragmentation were observed: a continuum level mechanism generating macrocracks with a size scale comparable to the case width, a mesoscale mechanism generating voids and microcracks at the non-bonded Al/W interfaces due to tensile strains, and mesoscale jetting due to the development of large velocity gradients between the W particles and surrounding Al. These mesoscale mechanisms can be used to tailor the size of the fragments (macro to mesoscale) by selecting an appropriate initial mesostructure for a given loading condition.

This chapter contains material that appears in Applied Physics Letters journal article K.L. Olney, V.F. Nesterenko, and D.J. Benson, Appl. Phys. Lett. 100, 191910 (2012). The dissertation author was the primary investigator and author of this paper.

6.5 Chapter references

[1] J.J. Davis and P.J. Miller, *AIP Conf. Proc.* **620**, 950 (2002).

[2] F. Zhang, K.B. Gerrard, R.C. Ripley, and V. Tanguay, *Shock Waves: 26th Int. Symp. on Shock Waves* , 395 (2009).

[3] M. Becksead, *Combustion, Explosion and Shock Waves* **41**, 533 (2005).

[4] F. Zhang, S.B. Murray, and K.B. Gerrard, *Shock Waves* **15**, 313 (2006).

[5] R. Ames, *Multi-functional Energetic Materials* **123**, 896 (2006).

[6] W. Mock, Jr. and J.T. Drotar, *AIP Conf. Proc.* **955**, 871 (2007).

[7] F.-X. Jette, A.J. Higgins, S. Goroshin, D.L. Frost, Y. Charron-Tousignant, M.I. Radulescu, and J.J. Lee, *J. Appl. Phys.* **109**, 084905 (2011).

[8] P.-H. Chiu and V.F. Nesterenko, *DYMAT* **2**, 947 (2009).

[9] P.-H. Chiu, C.-W. Lee, and V.F. Nesterenko, *AIP Conf. Proc.* **1426**, 737 (2012).

[10] K.L. Olney, D.J. Benson, and V.F. Nesterenko, *AIP Conf. Proc.* **1426**, 729 (2012).

[11] V.F. Nesterenko, P.-H. Chiu, C. Braithwaite, A. Collins, D. Williamson, K.L. Olney, D.J. Benson, and F. McKenzie, *AIP Conf. Proc.* **1426**, 533 (2012).

[12] K.L. Olney, P.-H. Chiu, C.-W. Lee, V.F. Nesterenko, and D.J. Benson, *J. Appl. Phys.* **110**, 114908 (2011).

[13] N.F. Mott, *Proc. of the Royal Soc. of London, A (Mathematical and Physical Sciences)* **189**, 300 (1947).

[14] D.E. Grady, *Fragmentation of Rings and Shells, the Legacy of N.F. Mott* (Springer, NY, 2006).

[15] D.J. Benson, V.F. Nesterenko, F. Jonsdottir, M.A. Meyers, *J. of the Mech. and Phys. of Solids* **45**, 1955 (1997).

[16] O.E. Patel, D.L. Frost, A.J. Higgens, *Phys. Rev.* **85**, 021401 (2012).

[17] J. Cai, V.F. Nesterenko, K.S. Vecchio, F. Jiang, E.B. Herbold, D.J. Benson, J.W. Addiss, S.M. Walley, W.G. Proud, *Appl. Phys. Lett.* **92**, 031903 (2008).

[18] E.B Herbold, V.F. Nesterenko, D.J. Benson, J. Cai, K.S. Vecchio,F. Jiang, J.W. Addiss,S.M. Walley, W.G. Proud, *J. Appl. Phys.* **104**, 103903 (2008).

[19] V.F. Nesterenko, *Dynamics of Heterogeneous Materials* (Springer, NY, 2001) Chap. 6.

[20] D.J. Benson, *Comp. Meth. Appl. Mech. and Eng.* **99**, 235 (1992).

[21] E. Vitali and D.J. Benson, *Int. J. Numer. Meth. Eng.* **67**, 1420 (2006).

[22] G.R. Johnson and W.H. Cook, *Eng. Frac. Mech*. **21**, 31 (1985).

[23] T.J. Holmquist, D.W. Templton, and K.D. Bishnoi, *Int. J. Impact Eng.* **25**, 211 (2001).

[24] D.J. Steinberg, *Equation of states and strength properties of selected materials*, Tech. Rep. (Lawrence Livermore National Lab, 1996).

[25] H. Hornberg, *Prop., Exp., Pyro*. **11**, 23 (1986).

Chapter 7

The mechanism of instability and localized reaction in the explosively driven collapse of thick walled concentric Ni-Al laminate cylinders

7.1 Chapter introduction

During the explosively- or magnetically-driven radial collapse of thin-walled metal cylinders, the geometric instabilities lead to the development of buckling [1, 2]. This type of instability is prohibited in the collapse of thick-walled cylinders. Instead, a material instability may develop due to the presence of softening mechanisms that initiate shear localization leading to the formation of multiple shear bands. Due to this property, the explosively- [3] or magnetically-driven [4, 5] collapse of thick-walled cylinders has been used to investigate the high strain/strain-rate deformation of various materials under plane strain conditions. To avoid spallation and minimize the shock induced effects, powder explosives with low densities, low detonation velocities, and sizes close to critical were used. All previously investigated materials in the thick-walled cylindrical geometry: solid monocrystalline and polycrystalline metals;

polymers [3, 6-9]; solid and granular ceramics (SiC and Al_2O_3) [10-12]; and reactive granular materials [13-15], accommodate the high strain/strain-rate global plane strain deformation by developing multiple shear bands. In some cases, these shear bands can number in the hundreds as in SS T-304L [9]. The mechanisms of plastic flow instability triggering the spontaneous shear localization and subsequent pattern of shear bands are different for various classes of materials. For example, in solid homogeneous metals, the thermal softening triggers the shear instability at a very modest increase in the uniform temperature caused by plastic deformation (~30 K) [9]. In the case of granular materials, it is microfracture of grains due to the high stresses localized at the contact interfaces [10-12].

Reactive Ni-Al laminates with different layer thicknesses and interface characteristics have been fabricated using various techniques such as physical vapor deposition [16, 17] or cold rolling/swaging [18, 19]. These reactive laminates have generated great interest due to their wide variety of applications requiring a controlled local heat source such as soldering [20, 21]. The chemical reaction in these laminates can be initiated by local heating [16-18] or by a shock-induced deformation with the subsequent influence of post-shock phenomena [22-27]. In reactive materials, the shear bands act as planar hot spots where reaction may occur and serve as an ignition source for the reaction in the bulk material [13-15]. In metal-based reactive materials, the intermetallic reaction may be triggered in zones of highly developed localized plastic deformation where the local temperature can be approximately an order of magnitude higher than the temperatures generated during the onset of the localized plastic flow. To improve the reactivity of these materials under conditions of dynamic high strain/strain-rate plastic deformation, the mesostructure should be designed to promote the localized plastic flow and the formation of hot spots necessary for the initiation of the reaction. Conversely, if it is necessary to prevent reaction until some critical strain, the mesostructure should be designed to block shear localization.

Since the mesostructure of the Ni-Al laminate materials can be viewed as an assembly of thin layers, it is interesting from both a fundamental and practical viewpoint to investigate the competing mechanisms of instability (geometric versus material) in the collapse of laminate thick-walled cylinders. It is not apparent if the geometric instability (buckling) or the material instability (shear localization) will be the dominant factor in the accommodation of plastic strain during the collapse. Furthermore, it is not clear if the instability will be sufficient to generate the local conditions that are suitable for the initiation of reaction between the Al and Ni layers. It has not been investigated if a buckling instability during dynamic plane strain loading can serve as an effective means to develop local hot spots and provide conditions that are necessary for the initiation of a reaction.

In this chapter, the Thick-Walled Cylinder (TWC) method [3] is applied with an improved explosive driver that ensured a better uniformity of explosive charge and enhanced tunability in comparison to the previously used powder explosives. The TWC method was used to examine the mechanisms of instability under the high strain/strain-rate deformation of Ni-Al laminates composed of concentric thin foil layers and to see if it is possible, under dynamic plane strain conditions, to initiate a chemical reaction between the Al and Ni.

7.2 Sample processing

Ni and Al laminate thick-walled cylinders were assembled from alternating concentric thin foil layers of pure Al (McMaster, annealed, Vickers microhardness HV= 251±4 MPa, purity at least 98%, initial thickness = 38.1 μm) and Ni (Alfa Aesar, annealed and soft tempered, HV= 898±9 MPa, purity 99%, initial thickness = 25.4 μm). The layer thicknesses were selected such that a 1:1 atomic ratio of Ni/Al was maintained. The concentric mesostructure was created one layer at a time starting with the outermost layer. Each layer was prepared by cutting a length of foil equal to the approximate circumference of its corresponding position in the final assembly.

The foil was cleaned with acetone, loosely rolled and inserted into the cylinder. A copper tube with an inner radius equal to the desired composite outer radius was used to encase the laminate. After each layer was inserted, a balloon was placed into the center cavity and inflated, causing the inner foil layer to unroll such that it was snug against its neighboring layer. A total of 24 bilayers were used to construct the sample. The composite was then encapsulated in a rubber jacket and processed using cold isostatic pressing (CIPing) by applying pressure, 345 MPa, on the interior surface of the laminate to increase stacking density and prevent the sample from buckling during preparation. After CIPing, the Al and Ni foils were densely packed, but the layers were not bonded. The overall density of the sample was (4.85 g/cc), corresponding to a porosity of 6%.
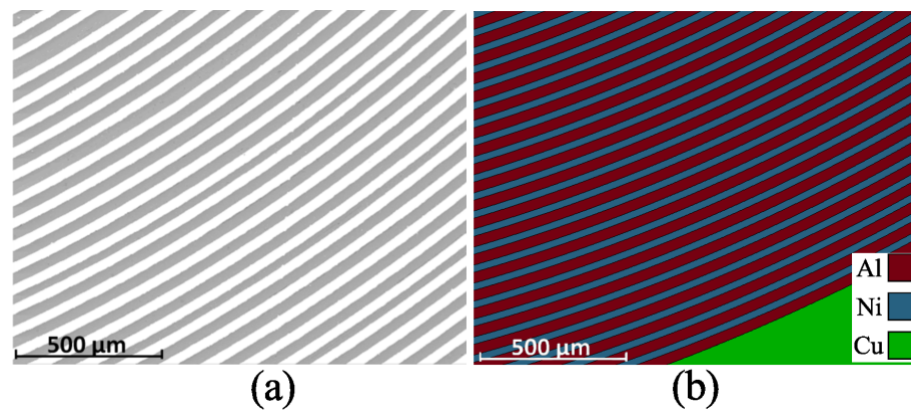
Figure 7.1 - (a) SEM of cross-sectional image of concentric Ni-Al sample after CIPing, Ni (white) and Al (gray) layers aligned alternatively and concentrically. (b) A detailed view of the Al (red) Ni (blue) laminate composite mesostructure with the inner Cu stopper tube (green) used in the numerical simulations. The thicknesses of Ni and Al foils used in the simulations were identical to the initial nominal thicknesses of their corresponding counterparts in the experimental samples.

The processed concentric thick-walled cylinder laminate samples had an outer diameter of 17 mm, an inner diameter of 12.1 mm, and a length of 30 mm. An image of the laminate mesostructure after processing taken by using Scanning Electron Microscopy (SEM) is shown in Figure 7.1 (a). The sample was enclosed in a copper assembly (see Figure 7.2) for the TWC test.

The copper stopper tube had an inner diameter of 10 mm and an outer diameter of 12 mm. The copper driver tube had an inner diameter of 17.1 mm and an outer diameter of 30 mm. The explosive driver for the TWC test was a gelled nitromethane (96% nitromethane, 4% PMMA) diluted 5% by mass with glass microballoons that allowed for the fine tuning of the dynamic loading (explosive density=0.82 g/cc, detonation velocity = 4.8 mm/μs). The diameter of the explosive charge was equal to 58 mm and thickness of the PVC container was 7.4 mm. The behavior of a laminate casing made from concentric Ni and Al layers under inner explosive loading was investigated in [28].
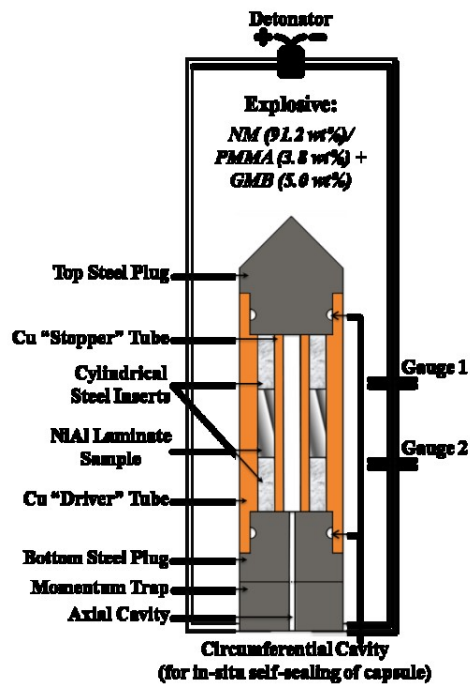
Figure 7.2 - Experimental setup for Thick Walled Cylinder Method.

7.3 Experimental results

Examination of the Ni-Al laminate material after the TWC test showed that the dominant mechanism of plastic strain accommodation in the experiments was the cooperative buckling of Ni and Al layers (see Figure 7.3 (a)). There were no observable shear bands in the sample. Based on the pattern of radially-aligned peaks and troughs of the buckles (apices), it may be concluded that the cooperative buckling of individual layers originated in the inner layers (due to higher strains) and propagated outward as the cylinder collapsed. Thus the instability mode of the outmost layers is dictated by the buckling mode of the inner layers. This mechanism of plastic strain accommodation in the laminate material is qualitatively different than found in previously investigated homogeneous materials (solid and granular, inert and reactive) subjected to similar loading conditions in the same geometry [3-15].
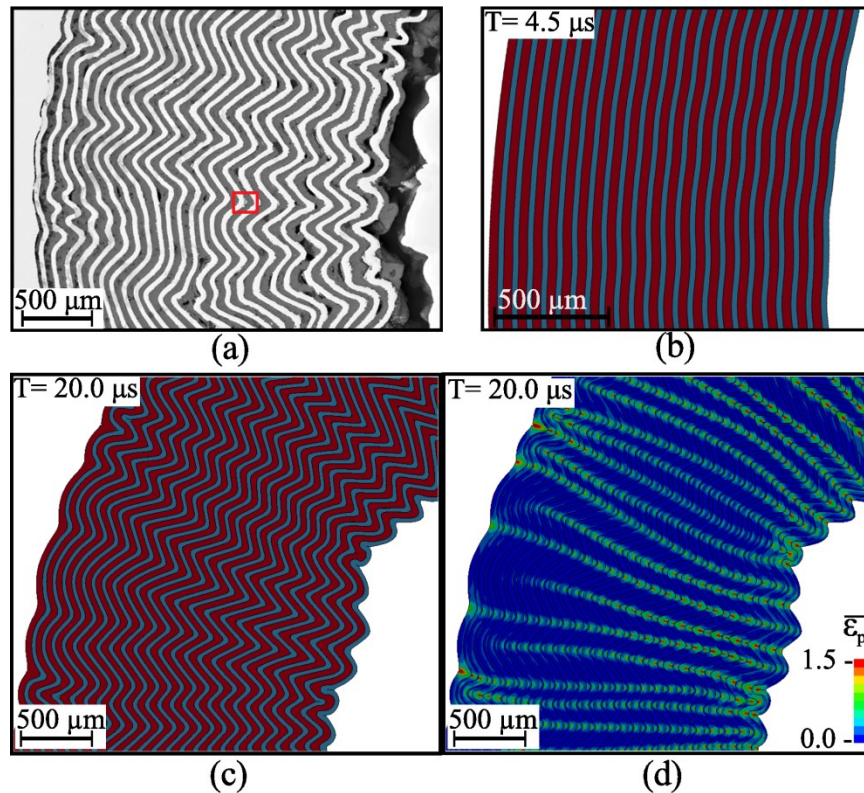
Figure 7.3 - (a) SEM image of the cross-sectional cut of the concentric Ni-Al sample after the explosive collapse, Ni (white) and Al (gray), the red square indicates the area with local reaction shown at larger magnification in Fig. 4; (b) the mesostructure of the simulated partially collapsed TWC sample (Al (red) and Ni (blue)) demonstrating the development of instability in the inner layers; (c) the mesostructure of the laminated fully collapsed TWC sample in the numerical simulations; (d) the effective plastic strain of the same view shown in (c).

7.4 Numerical modeling

Numerical simulations were used to elucidate the mechanism of buckling during the TWC experiments. They were conducted under plane strain conditions using LS-DYNA, a finite-element software. The similar conditions in previous numerical calculations [5, 29-32] adequately described experimental results; including the pattern of shear bands/cracks in uniform solid metals, solid ceramics, granular ceramics, and the complex shapes of monocrystals generated during collapse. Additionally, the collapsed stainless steel inserts above and below Ni-Al samples in this TWC test (Figure 7.2) exhibit nearly vertical shear bands indicating plane strain conditions.

A quarter of the sample was simulated using symmetry boundary conditions. The number of layers, layer thickness, and copper tube dimensions were consistent with the experiment. The mesh resolution was chosen such that the 8 rectangular elements spanned each layer to ensure that stresses and bending through the thickness would be captured. The simulation allowed for the layers to slip and separate. Friction was not included in the model. A detailed view of the geometry used in the simulations is presented in Figure 7.1 (b).

The modified nitromethane explosive was modeled using a JWL equation of state of the form

$$P = A\left(1 - \frac{\omega}{R_1 V}\right)e^{-R_1 V} + B\left(1 - \frac{\omega}{R_2 V}\right)e^{-R_2 V} + \frac{\omega E}{V} \tag{7.1}$$

where $A = 78.69$ GPa, $B = 1.92$ GPa, $\omega = 0.36$, $R_1 = 4.61$, and $R_2 = 1.06$ are constants obtained from Cheetah calculations [33]. Because the velocity of collapse is significantly smaller than the detonation speed, we assume that the explosive in the plane of interest detonates instantaneously. The material properties of Cu, Al, and Ni were modeled using the standard Johnson-Cook plasticity model [34] in conjunction with the Mie-Grüniesen equation of state. The constitutive parameters were taken from the [34-36] and are presented in Table 7.1 and Table 7.2.

Table 7.1 - Parameters for the Johnson-Cook constitutive model used in the simulations.

Material	P_0 [g cm^{-3}]	G [GPa]	A [MPa]	B [MPa]	n	c	m	T_m [K]
Al	2.77	26.2	84.21	426.0	0.34	0.015	1.0	773
Ni	8.902	74.45	297.2	648.1	0.33	0.006	1.44	1725
Cu	8.96	48.0	90.0	292.0	0.31	0.025	1.09	1356

Table 7.2- Parameters for the Grüneisen equation of state used in the simulations

Material	C [m s^{-1}]	S_1	S_2	S_3	γ_0	a
Al	5328	1.338	0.0	0.0	2.0	0.48
Ni	4650	1.445	0.0	0.0	1.93	0.50
Cu	3940	1.489	0.0	0.0	2.02	0.47

7.5 Discussion of the numerical modeling results

7.5.1 Mechanism of cooperative buckling

The geometry of the cylinder at the initial stage of instability demonstrating the initiation of cooperative buckling originating in the inner layers is presented in Figure 7.3 (b). The collapsed laminate sample with the fully developed instability is presented in Fig. 3(c) and the plastic strain distribution in the composite is shown in Figure 7.3(d). It is clear from comparing these results with the experiment (Figure 7.3 (a)) that the simulation of the instability at the final stage of collapse shows good agreement with the experiment. The number of apices in a single layer in the experiment was 148 while the simulation had 164, a 10.8% difference. Defining a characteristic amplitude of waviness, $\bar{A}_w$, as the average of the differences in the radius of all neighboring apices in the same layer yields an $\bar{A}_w$ of 155.7 µm (about 6 times Ni layer thickness) for 5th Ni layer in the experimental sample while the simulation predicts an $\bar{A}_w$ of 144.2 µm. Simulations with different strain rates of collapse were conducted by altering the explosive properties and demonstrated that increasing strain rate results in an increasing number of apices. The differences between the number of apices and the $\bar{A}_w$ in simulations and experiment is probably due to the difference in the high strain, high strain rate material behavior and the role of friction between layers in experiments.

The simulations and experiments both clearly demonstrate that the cooperative buckling of the layers was the dominant mechanism of plastic strain accommodation in the Ni-Al laminate

thick-walled cylinder during collapse. The simulations demonstrated that as the cylinder initially collapses, the individual layers experience compression in the hoop direction with the interior layers experiencing a larger hoop strain than the exterior layers. At first, the spontaneous buckling of the inner layers occurs and quasi-sinusoidal distortions develop. This initial buckling in the inner layers triggers the cascading geometric instability of neighboring layers extending all the way to the outermost layers. The amplitude of waviness of each layer increases to accommodate the change in circumference length with further collapse of the cylinder. The simulations show that this amplitude change is non-symmetric despite the initial symmetric geometry and that additional buckling does not occur on later stages of collapse. This suggests that the increase in amplitude of the initially buckled shape is the favorable mode of plastic accommodation. At the same time, we observed some secondary buckling (Figure 7.3 (a) and (c)), demonstrating that the instability in the outer foil layers may not be completely controlled by buckling in the innermost layers. In this case local conditions in the outer layers may also influence the instability.

The simulations show that prior to the instability initiation, the layers experience a ~5-6% increase in layer thickness. This plastic flow within the individual layers is a secondary mechanism of global plastic strain accommodation. However, this effect is minor in comparison with ~45% increase of the sample thickness during the collapse due to the cooperative buckling of layers which have an amplitude of waviness about 6 times the layer thickness.

Dramatic changes in the accommodation of global plastic strain were observed in numerical calculations if the layers were bonded. In this case, the prevailing mechanism was shifted from cooperative buckling to shear localization generating trans-layer shear bands. The resulting response is similar to that of homogeneous materials [3-15] under similar loading conditions. This suggests that the laminate mesostructure can be tailored to either allow or prevent shear band formation by altering the level of bonding and interface characteristics such as roughness. Additional simulations with both bonded and non-bonded Ni-Al layers constructed

with a brittle material having material properties similar to Ni and a ductile Al material demonstrated that the prevalent mode of large plastic accommodation is shear localization. The subsequent shear bands that were developed in these simulations had an angle of about 45° to the radius and spanned the entire thickness of the sample. Additionally, a dependence of the number of apices on the layer thickness was observed, which may be used to tune the reactivity of these materials.

7.5.2 Intermetallic reaction

Numerous areas of reaction were observed in the collapsed sample in areas adjacent to the apices (see Figure 7.4). Based on Energy Dispersive X-ray Spectroscopy (EDX) analysis, two types of reaction products were observed, Ni-rich and Al-rich, which were similar to the reaction products observed in [16-18]. Simulations also demonstrated that the areas near the apices, approximately the size of the layer thickness, were the areas of maximum local strains and temperatures. The typical level of effective plastic strains observed in these areas were about 1.5 corresponding to peak temperatures 823 K for Al and 873 K for Ni. The start of reaction in Ni-Al laminates [18, 37] was observed under static conditions at temperatures 473 - 873 K. This indicates that local plastic strains inside apex areas are sufficient to explain the observed localized reaction. The ignition temperature for nanolaminates is in the range of 450-900 K [16, 38], indicating that ignition in these materials can be attained in dynamic conditions similar to our experiments.

In addition to the local plastic deformation increase of interface temperatures also can be caused by friction. The role of friction is supported by the smaller localized spots of reaction observed at Ni-Al interfaces away from the apices.
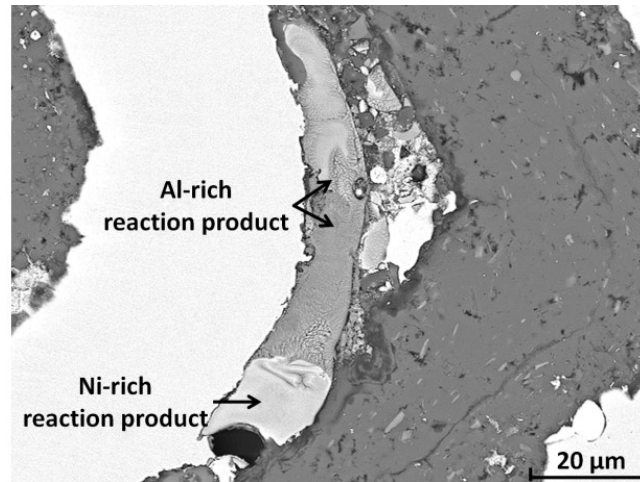
Figure 7.4 - An example of the intermetallic reactions observed at the Ni and Al interface at the inner apex region of the buckled Ni foil. EDX results showed two types of reaction products: Ni-rich and Al-rich.

7.6 Chapter conclusions

The TWC experiments and simulations of dynamic collapse of Ni-Al concentric laminate cylinders demonstrated a new phenomenon of the cooperative buckling originating in the innermost layers. The instability of all layers is dictated by the buckling mode of the inner layers. The laminate geometry resulted in the cooperative buckling of layers which is different from independent buckling of single thin walled cylinders. The investigated non-bonded laminate mesostructure blocked the development of localized shear bands, the major mechanism of large plastic strain accommodation observed in homogeneous materials under similar conditions. This buckling mechanism supported numerous localized reaction zones in the areas near the apices, but global ignition was not observed. Numerical simulations showed that it is possible to tailor the behavior of laminates by altering their mesostructural properties, e.g., bonding at the interfaces of Ni and Al, critical strain of fracture, and layer thicknesses.

This chapter contains material that appears in Applied Physics Letters journal article P.H. Chiu, K.L. Olney, A. Higgins, M. Serge, D.J. Benson, and V.F. Nesterenko, Appl. Phys. Lett., 102, 241912 (2013). The dissertation author was an investigator and author of this paper.

7.7 Chapter references

[1] A. L. Florence and G. R. Abrahamson, *J. Appl. Mech.-T Asme* **44**, 89 (1977).

[2] T.A. Duffey, R.H. Warnes, and J.M. Greene, *Growth of buckling instabilities during radial collapse of an impulsively-loaded cylindrical shell.* LANL report LA-UR-86-3852, 1987.

[3] V.F. Nesterenko, *Dynamics of Heterogeneous Materials* (Springer, New York, 2001) p.307.

[4] J.L. Stokes, V.F. Nesterenko, J.S. Shlachter, R.D. Fulton, S.S. Indrakanti, and Ya Bei Gu, i*n Proceedings of International Conference on Fundamental Issues and Applications of Shock-Wave and High-Strain-Rate Phenomena*, edited by K.P. Staudhammer, L.E. Murr, and M.A. Meyers, (2001, Elsevier, Amsterdam, 2011), pp. 585-592.

[5] Z. Lovinger, A. Rikanati, Z. Rosenberg, and D. Rittel, *Int. J. Impact Eng.* **38**, 918 (2011).

[6] Y. J. Chen, M. A. Meyers, and V. F. Nesterenko, *Mat. Sci. Eng. A-Struct.* **268**, 70 (1999).

[7] V. F. Nesterenko, M. A. Meyers, and T. W. Wright, *Acta Mater.* **46**, 327 (1998).

[8] M. A. Meyers, V. F. Nesterenko, J. C. LaSalvia, and Q. Xue, *Mat. Sci. Eng. A-Struct.* **317**, 204 (2001).

[9] Q. Xue, V. F. Nesterenko, and M. A. Meyers, *Int. J. Impact Eng.* **28**, 257 (2003).

[10] C. J. Shih, V. F. Nesterenko, and M. A. Meyers, *J. Appl. Phys.* **83**, 4660 (1998).

[11] C. J. Shih, M. A. Meyers, and V. F. Nesterenko, *Acta. Mater.* **46**, 4037 (1998).

[12] V. F. Nesterenko, M. A. Meyers, and H. C. Chen, *Acta. Mater.* **44**, 2017 (1996).

[13] V. F. Nesterenko, M. A. Meyers, H. C. Chen, and J. C. Lasalvia, *Appl. Phys. Lett.* **65**, 3069 (1994).

[14] V. F. Nesterenko, M. A. Meyers, H. C. Chen, and J. C. Lasalvia, *Metall. Mater. Trans. A* **26**, 2511 (1995).

[15] H. C. Chen, V. F. Nesterenko, and M. A. Meyers, *J. Appl. Phys.* **84**, 3098 (1998).

[16] E. Ma, C. V. Thompson, and L. A. Clevenger, *J. Appl. Phys.* **69**, 2211 (1991).

[17] K. Barmak, C. Michaelsen, and G. Lucadamo, *J. Mater. Res.* **12**, 133 (1997).

[18] L. Battezzati, P. Pappalepore, F. Durbiano, and I. Gallino, *Acta Mater.* **47**, 1901 (1999).

[19] T. P. Weihs, *Handbook of Thin Film Process Technology.* (Institute of Physics, Bristol, UK, 1998), pp. F7:1.

[20] J. Wang, E. Besnoin, A. Duckham, S. J. Spey, M. E. Reiss, O. M. Knio, M. Powers, M. Whitener, and T. P. Weihs, *Appl. Phys. Lett.* **83**, 3987 (2003).

[21] J. Wang, E. Besnoin, O. M. Knio, and T. P. Weihs, *J. Appl. Phys.* **97**, 114307 (2005).

[22] N. N. Thadhani, *Prog. Mat. Sci.* **37**, 117 (1993).

[23] I. Song and N. N. Thadhani, *Metall. Trans. A* **23**, 41 (1992).

[24] D. Eakins and N. N. Thadhani, *J. Appl. Phys.* **101**,043508 (2007).

[25] Y. Horie, R. A. Graham, and I. K. Simonsen, *Mater. Lett.* **3**, 354 (1985).

[26] I. K. Simonsen, Y. Horie, R. A. Graham, and M. Carr, *Mater. Lett.* **5**, 75 (1987).

[27] F. X. Jette, A. J. Higgins, S. Goroshin, D. L. Frost, Y. Charron-Tousignant, M. I. Radulescu, and J. J. Lee, *J. Appl. Phys.* **109**, 084905 (2011).

[28] Fan Zhang, Robert Ripley, and William Wilson, *AIP Conf. Proc.* **1426**, 275 (2012).

[29] S. Nemat-Nasser, T. Okinaka, V. Nesterenko, and M. Q. Liu, *Philos. Mag. A* **78**, 1151 (1998).

[30] T. Rabczuk, P. M. A. Areias, and T. Belytschko, *Int. J. Numer. Meth. Eng.* **69**, 993 (2007).

[31] K. Solanki, M. F. Horstemeyer, M. I. Baskes, and H. Fang, *Mech. Mater.* **37**, 317 (2005).

[32] E. Vitali and D. J. Benson, *Comput. Mech.* **49**, 197 (2012).

[33] L.E. Fried, W.M. Howard, and P.C. Souers, CHEETAH 2.0 User's Manual , URCL-MA-117541 Rev. 5 ed. (Lawrence Livermore National Laboratory, Livermore, CA 1998).

[34] G. R. Johnson and W. H. Cook, *Eng. Fract. Mech.* **21**, 31 (1985).

[35] D. J. Steinberg, *Equation of states and strength properties of selected materials*, Technical Report Number: UCRL-MA-106439 (Lawrence Livermore National Lab, 1996).

[36] E. Vitali, C. T. Wei, D. J. Benson, and M. A. Meyers*, Acta Mater.* **59**, 5869 (2011).

[37] F. Cardellini, G. Mazzone, A. Montone, and M. V. Antisari, *Acta Metall. Mater.* **42**, 2445 (1994).

[38] R. Knepper, M. R. Snyder, G. Fritz, K. Fisher, O. M. Knio, and T. P. Weihs, *J. Appl. Phys.* **105**, 083504 (2009).

Chapter 8

Mechanisms of plastic strain accommodation in corrugated Ni-Al laminates

8.1 Chapter introduction

Reactive materials (e.g., Al-PTFE, Ti-Si, Ti-B) have shown promise for various applications due to their high energy density that can be released during extreme dynamic deformation [1-3]. Ni-Al laminate materials are a well investigated system with respect to the kinetics of reaction initiation and propagation depending on mesostructure [4]. In addition to the traditional ignition methods (direct heating or spark ignition [5]) the intermetallic reaction can be initiated during dynamic mechanical loading, for example, during impact or rapid launch of a projectile. It has been shown that strong shock loading and subsequent post-shock mechanochemical processes can result in the ignition of Ni-Al mixtures [6-8].

Ignition may also occur at relatively weak shock pressures and high strain plastic flow where ignition occurs in the hot spots formed in zones of shear localization. These are inevitably present in most materials accommodating high strain, high strain rate plastic flow as observed in inert granular materials [9-11], solid metals [12-14] and reactive powder based mixtures [15-17]. The rate of complete reaction in the material is determined by the heat of reaction and the spacing

between the shear bands that serve as local hot spots. As such, an understanding of how and where these hot spots form is an important step in tailoring the material system performance to either hasten or delay the ignition and reaction rate.

The Thick Walled Cylinder (TWC) method [18] was proposed to examine the development of material instabilities during the high strain rate, large strain deformations in plane strain conditions. It uses an explosive to collapse a cylindrical tube of the sample placed between two copper tubes. The interior copper tube (stopper tube) controls the total final maximum strain in the sample while the outer copper tube (driver tube), which is accelerated by an explosive charge and axisymmetrically drives the radial collapse. Because the mass of the driver copper tube is significantly larger than the mass of the TWC sample, the kinetics of the collapse are determined mainly by the thickness of the outer copper tube, allowing the testing of materials with different properties at similar strains and strain rates.

In most materials, the material instability generated during the TWC test generally is manifested by the formation of multiple, periodic, self-organized shear localization zones originating in the interior of the sample and propagating radially outward at an angle close to 45° to the radius. In the case of Ni-Al laminates composed of alternating non-bonded concentric Ni and Al thin foils with low initial porosity [19], this pattern of shear bands was completely blocked. Instead, the large plastic strain was accommodated by the cooperative buckling of the layers where the wavelength of the buckling was dictated during the initial stages of the collapse by the layers in the interior region of the sample. Numerous reaction spots formed in the apex areas during the collapse of these concentric Ni-Al laminates.

The mesostructure of the Ni-Al laminate (e.g., bilayer thickness) may be controlled via swaging. This large strain processing of laminates forms a corrugated pattern of layers. The degree of corrugation is controlled by the number of swaging cycles such that fewer swaging cycles result in a mesostructure that is locally closer to the concentric laminate while a larger

number of swaging cycles results in a sample with more/larger wrinkled layers. As such, it is important to understand how these laminate materials with two different spatial features (bilayer thickness and corrugation scale) behave during high strain, high strain rate deformation. Of specific importance is their effect on the development of, or the blocking of, shear localization during plastic deformation and the formation of hot spots and subsequent reaction zones. It is not clear if the laminate materials with corrugated mesostructure will behave like the concentric laminates, blocking shear localization via cooperative buckling with the apex locations promoting the local high straining and reaction initiation during the collapse, or if the anisotropic mesostructure will lend itself to increasing the shear band density.

In this chapter, the TWC method was used to test two corrugated Ni-Al laminates SW-6 and SW-7, created by the swaging process. To examine the mechanisms of plastic strain accommodation of the corrugated laminate during the collapse, a numerical simulation was conducted using the real geometry extrapolated from a characteristic micrograph of the plane perpendicular to the sample axis.

8.2 Sample processing

The corrugated mesostructures were processed from alternating layers of Al (30 micron nominal thickness) and Ni (20 micron nominal thickness) that were stacked, rolled into a cylinder and then placed into a tubular steel jacket. This jacketed assembly was then swaged using mating tapered dies resulting in cylindrical shaped rods with a corrugated mesostructure. The two rods that underwent 6 and 7 swaging cycles were used to prepare samples tested in this paper, SW-6 and SW-7, respectively. Additional details of the swaging process can be found in [20].

Each of the swaged rods (SW-6 and SW-7) was cut into three 30 mm long segments and labeled A, B, and C. Electrical Discharge Machining (EDM) was used to remove the central core of each rod segment to create the hollow cylinders used as samples in the dynamic tests and to

ensure that no reaction occurred during the machining of the samples. The initial, corrugated, as-processed Al-Ni samples are presented in Figure 8.1 (a) and Figure 8.1 (b) and high magnification scanning electron micrographs for these samples are presented in Figure 8.1 (c) and Figure 8.1 (d). Due to the processing technique used to create the samples, their mesostructures are highly heterogeneous on two different spatial scales – the size of the layers and the size of the corrugation. In most places in the samples the thicknesses of Al and Ni layers are similar and can be characterized by a nominal thickness. Variations in swaging and machining processes resulted in slightly different inner and outer diameters of the samples (see Table 8.1).
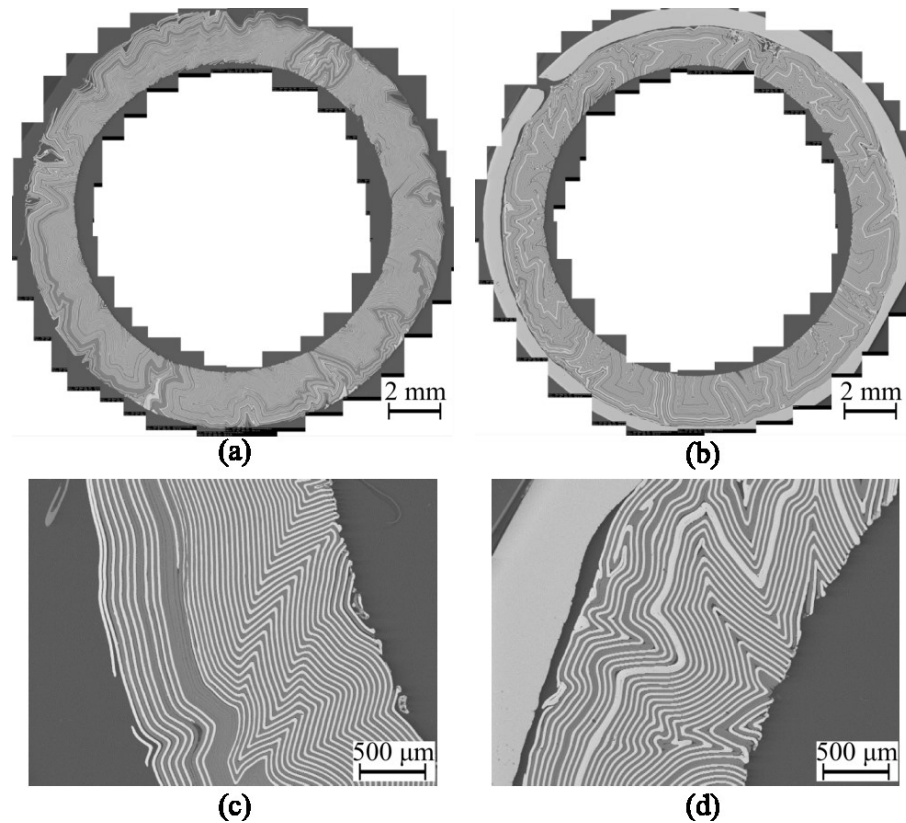
Figure 8.1 - Cross-sectional micrographs of the swaged Ni-Al laminate tubes (a) SW-6A and (b) SW-7A before the TWC test. The higher magnification images, (c) and (d), correspond to SW-6A and SW-7A, respectively. The Ni and Al layers had a nominal thickness of 20 and 30 microns, respectively, in each sample and appear as white and dark grey, respectively. Samples SW-7A, B, and C have a thin steel jacket on the exterior of the sample.

Table 8.1 - Dimensions of the TWC samples before the TWC experiments.

Sample		SW-6A	SW-6B	SW-6C	SW-7A	SW-7B	SW-7C
Inner sample diameter before TWC	(mm)	12.08	12.21	12.25	12.20	12.20	12.23
Outer sample diameter before TWC	(mm)	16.21	17.41	17.38	17.06	16.74	16.78
Inner diameter of copper stopper tube before TWC	(mm)	10.00	10.00	10.00	10.00	10.00	10.00
Outer diameter of copper stopper before TWC	(mm)	12.00	12.00	12.00	12.00	12.00	12.00

Sample SW-7 retained a thin steel jacket (400-700 μm thickness), which was left on for convenience of sample handling, and did not significantly affect the behavior of collapse during the dynamic deformation because the copper driver tube dominates the dynamic collapse, irrespective of the sample's mesostructure.

The hollow Ni-Al laminate cylinder samples were placed in the TWC assembly shown in Figure 2 (a). The inner diameter and outer diameter of the copper stopper tube in all experiments was 10.0 mm and 12.0 mm, respectively. The dimensions of the copper stopper tube allowed for the precise control of the dynamic global strain imparted to the sample due to the complete collapse of the TWC assembly (see Figure 2.4). The outer diameter of the copper driver tube was 31.8 mm for all experiments; the inner diameter of the copper driver tube (16.8 - 17.5 mm) was customized for each sample. The top and bottom steel plugs in the TWC assembly had grooves (depth and radius equal to 5 mm). They served for *in situ* sealing of the TWC assembly (see Figure 2.4) during the test to ensure the complete recovery of the test specimen and to prevent the penetration of the detonation products.

The TWC assembly was placed in a PVC container with an inner diameter of 58.0 mm and a wall thickness of 7.4 mm. The container was filled with a gelled Nitromethane (96% Nitromethane, 4% PMMA) explosive to drive the collapse of the TWC assembly. Glass microballoons (3M™ Glass Bubbles K1) were used to dilute the explosive 5% by mass, allowing the fine-tuning of the dynamic loading [19]. The detonation velocities in the experiments were measured to be 4.80 ± 0.05 km/s and exhibited good reproducibility.

8.3 Experimental results

The recovered self-sealed samples were along planes perpendicular to their axes after the TWC experiments with EDM to prevent any incidental reaction event from occurring during the post-TWC examination process. The dimensions of the samples and the effective strains on the interface with the copper stopper tube are presented in Table 8.2.

Microstructural analyses of the cross-sectional axial cuts were performed by using scanning electron microscopy (SEM). The composite images of the medial cuts from all of the tested samples are presented in Figure 8.2. It should be noted that there are variations of the mesostructure through the axial direction of the sample due to the swaging processing. As such, the composite images of the mesostructures for the collapsed samples SW-6A and SW-7A, presented in Figure 8.2, do not exactly correspond to the initial mesostructures presented in Figure 8.1, as they are cut from different axial locations. High magnification images of representative areas of the collapsed mesostructures are presented in Figure 8.3, illustrating that local trans-layer shear bands were common in all samples and generally are located in the interior regions of the sample. Additionally, this figure shows a unique mesostructual behavior - the extrusion of wedge-shaped regions on the inner surface of the cylinder towards the inner copper

stopper tube. These wedge-shaped regions directly correspond to the initial corrugation in the mesostructure generated during the swaging processing.

Table 8.2 - Dimensions of the TWC samples and effective strains after the TWC experiments

Sample		SW-6A	SW-6B	SW-6C	SW-7A	SW-7B	SW-7C
Mean sample inner diameter after TWC	(mm)	6.58	7.12	6.82	6.66	6.86	6.62
Mean sample outer diameter after TWC	(mm)	13.02	14.54	14.32	14.28	13.22	13.40
Calculated diameter of fully collapsed copper stopper tube based on mass conservation	(mm)	6.63	6.63	6.63	6.63	6.63	6.63
Calculated effective strains (ε_{ef}) of the inner sample based on mass conservation of inner copper stopper tube		0.69	0.70	0.71	0.70	0.70	0.71
Measured effective strain (ε_{ef}) of the outer surface of the sample		0.25	0.21	0.22	0.21	0.27	0.26

The local trans-layer shear bands (see Figure 8.3), observed in all samples, were limited to the inner areas of the sample and did not create a periodic pattern as in all previously investigated granular and solid materials [9-17]. In general, the local trans-layer shear bands spanned ~3-10 layers in the areas where the Ni and Al layers were approximately radially aligned. This radial alignment obstructed the accommodation of large strain by other mechanisms. For example, the formation of shear localization in the soft Al layers or sliding along non-bonded Ni-Al interfaces, as well as the development of cooperative buckling [19], were less favorable than trans-layer shear localization. These trans-layer shear bands were oriented approximately 45° from the radial direction corresponding to the maximum global stress. Within these shear band zones, the Ni and Al layers were elongated and fragmented as shown in

Figure 8.5 (c). This elongation resulted in a decrease in the layer size in the shear band by nearly

an order of magnitude (from approximately 12 microns to approximately 1.2 microns).

By comparing the mesostructure before and after the TWC test, it is apparent that there are more

radially aligned apexes and less locally coaxial areas in the post-experimental samples,

suggesting that the mechanism of cooperative buckling, similar to that observed in the concentric

mesostructure in [19], is active in regions where the layers are locally concentric. The generation

of the apexes in the locally coaxial areas is likely influenced by the initial corrugation of the areas

interior to these regions.

The final mean inner diameter of the Al-Ni samples are presented in Table 8.2. The
maximum effective global strains [18]

$$\varepsilon_{\text{ef}} = \frac{2}{\sqrt{3}} \ln\left(\frac{r_0}{r_f}\right) \tag{8.1}$$

at a material point in the sample were calculated using the initial radius of this point (r_0) and the

radius after the collapse (r_f). Due to the highly irregular interior surface of the collapsed TWC

samples, the corresponding value of r_f was calculated based on the conservation of mass of the

copper stopper tube, assuming a perfect cylindrical geometry of collapse. The mass of a central

copper rod with a height 7.8 mm is equal to 2.21 gram and the initial mass of the corresponding

segment of copper stopper tube with the same height was 2.32 gram. This suggests that only 0.11

gram was removed from the inside surface of the collapsed copper stopper tube due to axial

jetting or due to axial plastic flow of the sample. This translates to a difference of 7.8x10^{-2} mm

(2.4%) for the outside diameter of the collapsed copper stopper tube if we assume that this mass

difference is due solely to the removal of central part of copper stopper tube by jetting. If we

attribute this difference in mass to axial elongation due to plastic flow of the sample, the upper

estimate of axial strain will be 0.047. The global effective strain in all of the samples on the inner

surface was between 0.69 and 0.71 while on the outer surface, the strains were between 0.21 and

0.27. The corresponding final inner and outer calculated radii are shown in Figure 8.2 as blue lines imposed over the collapsed samples. The cylindrical geometry of the outside surface of the sample (deformed by a copper driver) was preserved during the collapse process, allowing us to model the heterogeneous deformation of the interior areas assuming a cylindrical exterior geometry, as in the other cases of collapsing cylinders with a complex inner cavity shape [21, 22]
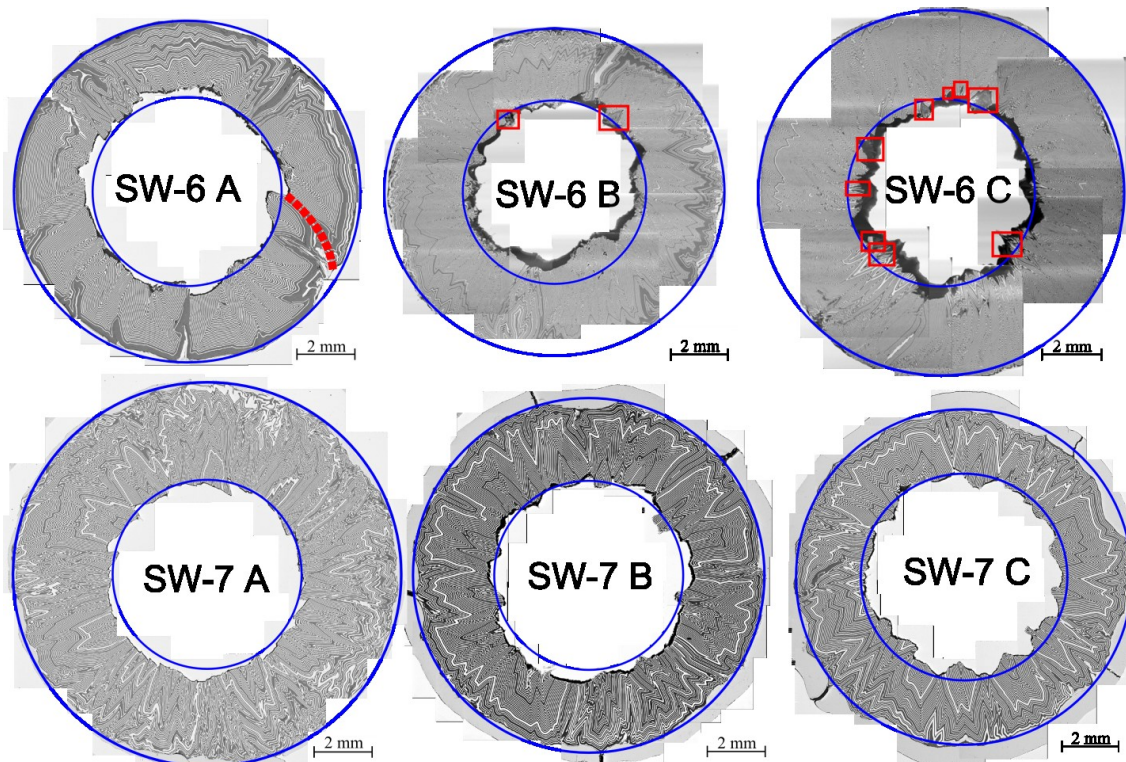
Figure 8.2 - Axial slices of the collapsed samples showing axial symmetry of the outside surface of deformed samples, similar maximum strains (0.69-0.71), and similar features on the inner surface (wedge extrusion). The inner blue circles in each of the samples represent the calculated mean inner diameter of the sample based on the mass conservation of the inner copper stopper tube, assuming plane strain geometry of deformation for the copper driver and stopper tubes during the collapse. A global shear band is shown in SW-6A by a dashed line; areas of extruded and reacted wedges in SW-6B and SW-6C are shown by red squares.
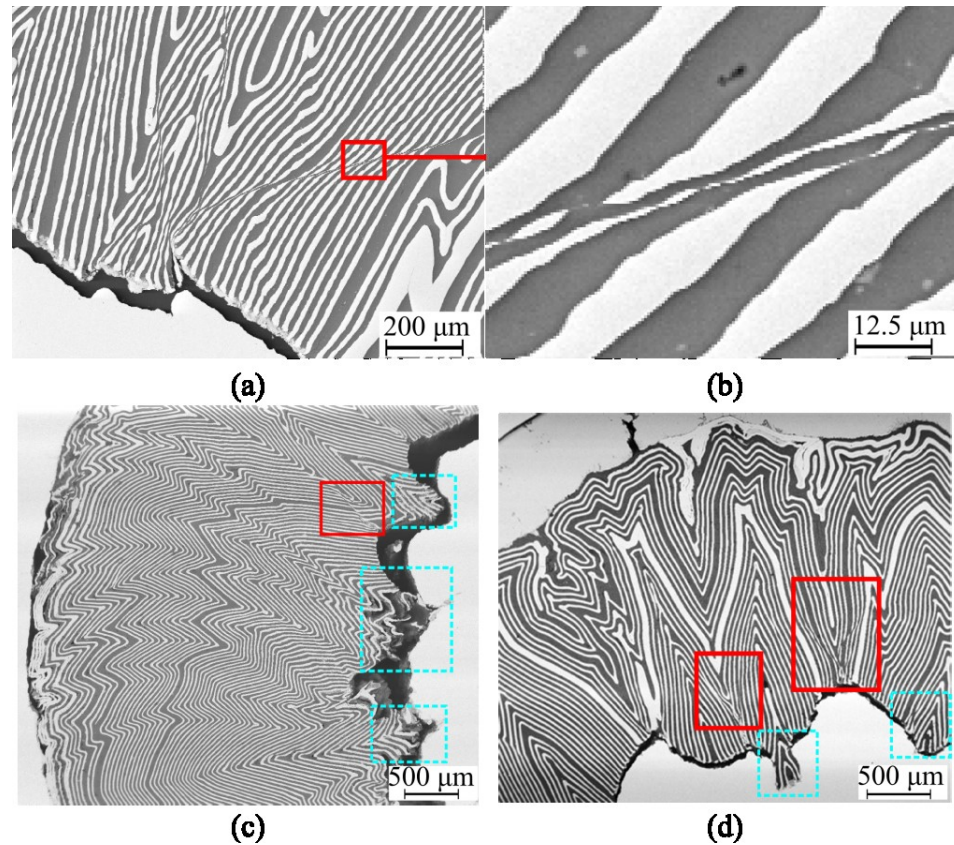
Figure 8.3 - Two mesoscale mechanisms of the deformation accommodation in collapsed laminates samples – wedge extrusions and trans-layer shear bands spanning only a few layers are shown in (a), SW-6B and (b), SW-7C; a detailed view of the trans-layer shear band in SW-7A is shown in (c) and (d) and demonstrates the dramatic elongation and subsequent fracture of the Ni and Al layers within the shear zone. The Ni layers appear white and the Al layers appear dark grey.

Intermetallic reaction caused by the high strain plastic flow of Ni and Al within some of the trans-layer shear bands was observed in the areas away from the interface with the copper stopper tube, as in the sample SW6-B (see Figure 8.4). The possible mechanism of reaction within these trans-layer shear bands consists of several steps. First, the localized high strain shearing within the trans-layer shear band elongates the Ni and Al layers (see Figure 8.3 (c)) resulting in a reduction in the layer thicknesses by an order of magnitude. At some shear strain, the instability of the elongation process causes the layers to fragment. This provides a region in these shear zones where a mixture of small, sub-micron fragments of Ni and Al exist which, due

to the reduction in bi-layer size, have a significantly lower temperature of ignition, approaching a minimum of 490 K [23, 24]. Second, the localized heating caused by the high strain plastic flow inside the shear band allows for the reaction to develop. Third, because the Al and Ni layers outside the shear bands are significantly thicker than the elongated and fragmented layers inside the shear band, and since they are relatively cold due to a small strain plastic deformation, the reaction is quickly quenched and does not extend outside of the shear zone.

We did not observe propagation of reaction into the bulk of the laminate, however this dynamic plastic deformation can be used as preconditioning making Ni-Al laminates more susceptible for the bulk reaction initiation by subsequent shock loading.

In addition to the high strain shear induced reaction observed in the trans-layer shear bands, the tips of Ni layers along the sample interface with the stopper tube showed signs of bending and mushrooming from initially blunt tips with some degree of reaction (see Figure 8.5). This may be due to the presence of the initial gap between the sample and the copper stopper tube. At the initial stage of collapse, the sample closes the small air gap, colliding with the copper stopper tube, and the tips of the layers deformed during this impact in a fashion similar to Taylor bar samples [23, 24], developing localized plastic strain and increasing the local temperatures at the tips. Axial shearing at the sample-copper stopper tube interface may also contribute to the reaction initiation. Lastly, due to the small gap between the sample and the copper stopper tube, a high velocity jet of metals/air could develop, providing additional heating which is favorable for reaction initiation.

These mechanisms of reaction at the sample-copper stopper tube interface are the probable causes of full reaction in some of the wedge shaped regions (see Figure 8.6). It is interesting that the quenched reaction front in the wedges were contained within the very specific corrugated mesostructure of each wedge. This suggests that reactions were initiated in the wedges, after they were extruded by plastic flow, and then they were rapidly quenched by

adjacent, cold material. However, this mechanism of reaction initiation in the wedge shaped regions is beyond the scope of this paper, which focuses on deformation induced reaction.

The reactions in the Al-Ni system have been extensively investigated both theoretically and experimentally. Depending on the stoichiometry and morphology of Ni/Al reactants, fabrication methods, and ignition processes and conditions, the first phase to form in Ni-Al reaction has been reported to be Al_3Ni [23, 24, 27-31], AlNi [32-34], Al_9Ni_2 [35, 36], or Ni_3Al [37, 38]. Energy-dispersive X-Ray spectroscopy (EDX) analysis was performed in the reacted trans-layer shear bands and the reacted wedges to determine the composition of the reaction products (locations examined are shown in Figure 8.4 (b) and Figure 8.6 (b)). It revealed that the atomic ratio of Al/Ni varies from 0.3 to 6 in the reaction products. This shows that both Ni-rich and Al-rich products exist in the reacted areas. In addition to the Al/Ni reaction products, the presence of a small amount of Cu was detected in some of the spots in the reacted wedges. This is likely due to the contact of the sample with the copper stopper tube. In the reacted shear band, significant amounts of oxygen were detected suggesting that an oxide layer formed.
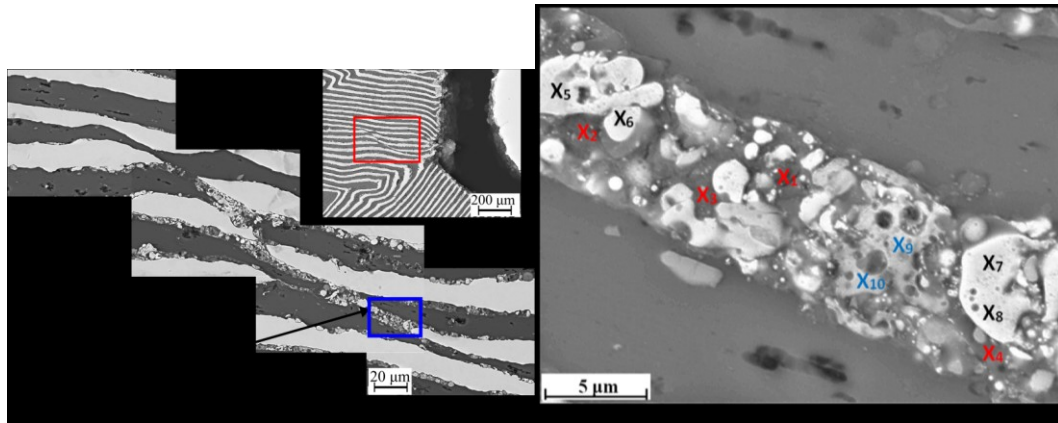
Figure 8.4 - (a) A detailed view of a local reacted trans-layer shear band in sample SW-6B (location is boxed in red). (b) A detailed view of the locations X1-X10 in the sample SW-6B (blue boxed region) where the EDX analysis was conducted showing Al-rich (X1-X4), Ni-rich (X5-X8), and Ni-Al (X9-X10) reaction products.
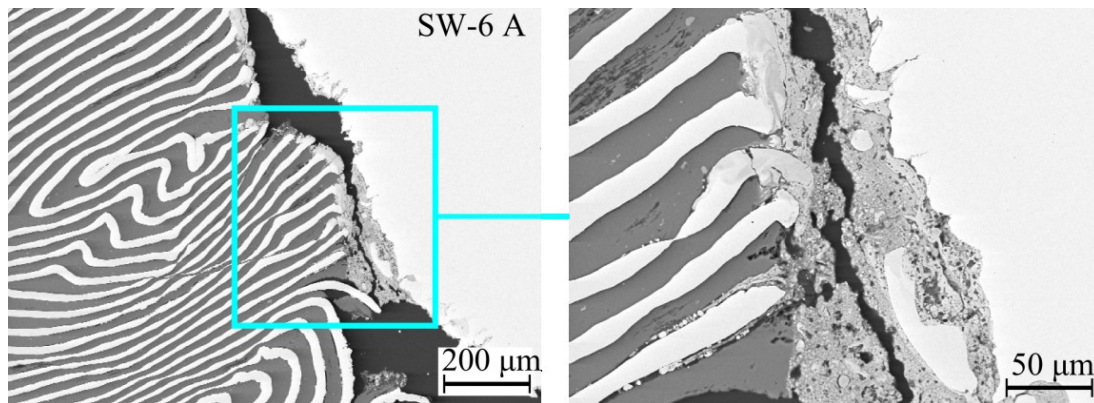
Figure 8.5 - Bent and deformed Ni layers (compare the geometry of Ni layers in the initial sample in Figure 8.1 (b)), showing melting and localized reaction at the interface with copper stopper tube.
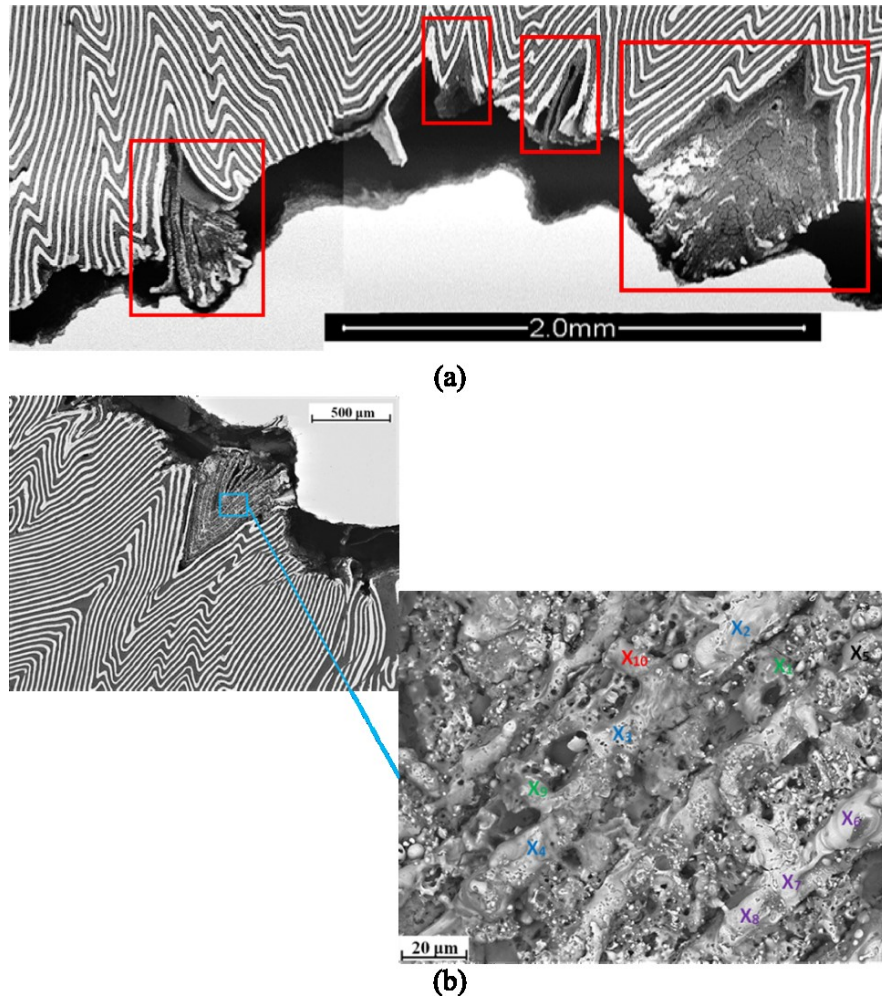
Figure 8.6 - (a) Examples of localized reaction in some of the extruded wedge-shaped regions in SW-6 C (regions in the red boxes) showing the presence of an intermetallic reaction and (b) a reacted wedge in SW-6B with locations for EDX analysis identified.

8.4 Numerical modeling

Numerical simulations were performed using LS-DYNA [39], a general-purpose finite element program, under plane strain conditions. For the TWC experiments, plane strain conditions have been shown to provide good agreement with complex patterns of deformation (e.g., as in granular SiC [11] stainless steel [14], monocrystal copper [21, 22] and in coaxial Ni-Al laminates [19]) under similar testing conditions [18]. This is due to the explosive driver,

nitromethane, having a significantly faster detonation velocity than the velocity of collapse and the deformation of the sample being mainly radial in nature. No significant axial deformation of samples was detected, as mentioned above, based on mass conservation of the segments of the copper stopper tube. The axial direction of plane shear bands in stainless steel samples also supports this assumption. Additionally, the axial orientation of the grooves on the outer surface of the copper stopper tube corresponds to kinks where shear bands originated and wedges are extruded in the Ni-Al samples.

8.4.1 Generation of the mesostructure

Since the mesostructure of the corrugated sample is highly anisotropic, contains non-uniform layers, and does not contain regular repeatable mesostructural features, a process was developed to extract the mesostrutural geometry from images of axial slices of the sample.

First an optical microscope image of a section of the mesostructure was obtained using an optical microscope such that a view of ~15-20 degree wedge of the sample is in the entire field of view. This is done to ensure that at least one initial wedge shaped region is in the field of view. Additionally, using a single image of the area ensures that there are no artifacts in the image due to image stitching that may be present when connecting multiple higher resolution images. This image was then imported into GIMP ver. 2.7, an open source photo editing software, and the interfaces of the Al layers were traced. These interfaces were then filled with a solid color. The traced layers were then saved as a .jpg file. The images were converted into a binary matrix using the image processing toolbox in Octave [40], an open source high-level interactive programming language for numerical computations, such that pixels in associated with Al layers would be designated with a value of 1 while pixels outside of these layers would be designated a value of 0. The optical microscope image of the section of the corrugated sample used to generate the mesostructure and the corresponding extracted Al layers are presented in Figure 8.7.

| (a) | (b) |
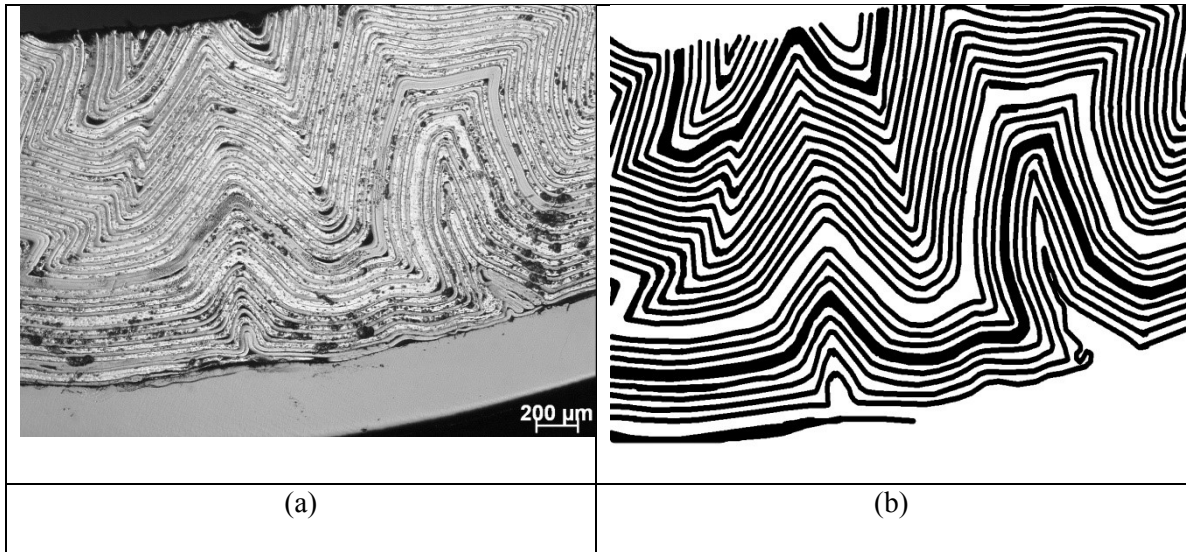
Figure 8.7 – The optical microscope image (a) and the corresponding image of the extracted layers (b) used for the section of the corrugated laminate simulations. This section of the laminate was chosen as it contained many of the representative mesoscale features associated with the corrugation (e.g. interior wedge shaped regions).

The edges of the layers were found by removing all pixels that do not neighbor a pixel with a zero value above, below or to the sides. An algorithm was developed and then used to separate all of the pixels associated with the individual layers into individual arrays. This algorithm began by incrementing along the horizontal and then vertical coordinate of the image matrix until an edge pixel was encountered. After encountering the pixel, the algorithm performed a recursive search where the pixels in the 3x3 neighborhood were searched for other edge nodes. Once all of the edge nodes associated with the layer was identified, they were placed into an array and the pixels were set to zero in the image matrix. This process continued until all of the edge pixels were placed into the appropriate layer array. The lines were then smoothed using a simple moving average algorithm with the window size of 4 to reduce the noise associated with the pixilation process.

The pixel locations were transformed into x-y location data by a scale factor of 2.26×10^{-4} which was determined by the measuring the scale on the SEM image in pixels. The x-y

location was shifted in the x-direction such that the innermost layer at y=0 is equal to the experimental inner radius of the corrugated sample. Since the field of view in the SEM image only has a small portion of the entire sample in view, a 15 degree wedge of the sample was modeled. Pixels that fell outside of this region were cropped from the layer arrays. The remaining arrays were exported as lists of x-y coordinates.

The lines were then imported into LS-Prepost [39], and smoothed via the b-spline smoothing tool. A mesh size was chosen such that a minimum of 8 elements spanned the thickness of each layer. This process is illustrated in Figure 8.8. Once the Al layers were generated, the process was repeated with the Ni layers. The initial mesostructure of the corrugated sample is presented in Figure 8.9.

The Al, Ni, Cu, and stainless steel used in the simulation were modeled using the Johnson-Cook [41] constitutive model (see Section 3.2) in conjunction with the Grüneisen equation of state. The initial yield strength, A, of the Ni and Al was calculated using the microhardness values of the Al and Ni foils. The other material parameters were taken from the literature [41-43] and are presented in Table 8.3 and Table 8.4.
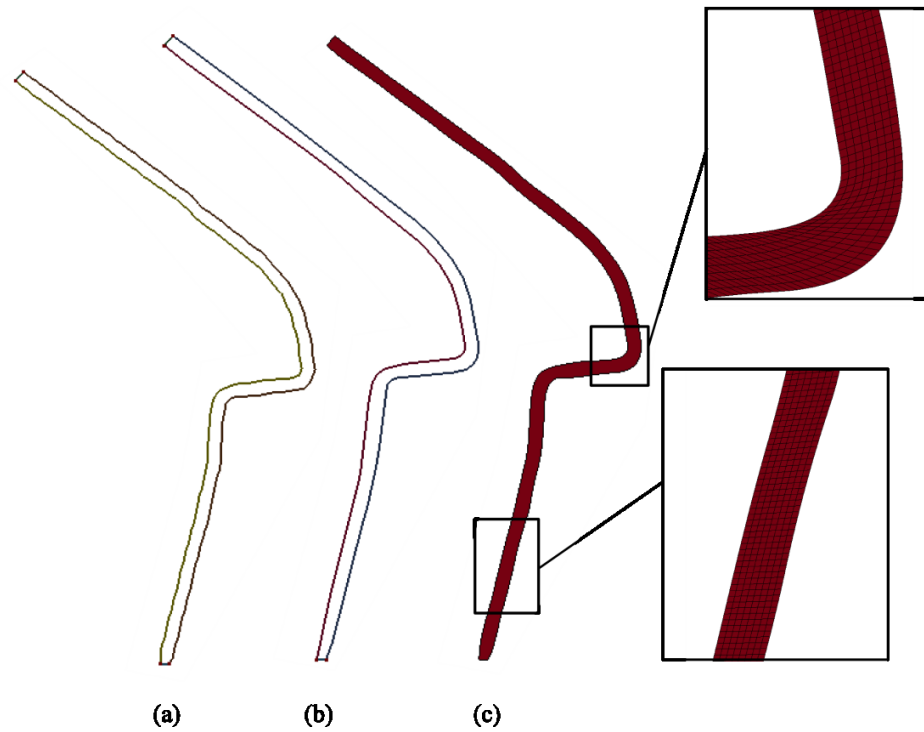
Figure 8.8 – The process of mesh generation in one of the layers in the corrugated Ni-Al laminate. (a) The x-y coordinates were extracted from the pixel information and imported into LS-Prepost. (b) The lines were smoothed using b-splines to reduce the noise on the layer interfaces. (c) The generated mesh of the layer with 8 elements spanning the thickness. The inserts on the right of (c) show the mesh resolution at two sections of the layer.
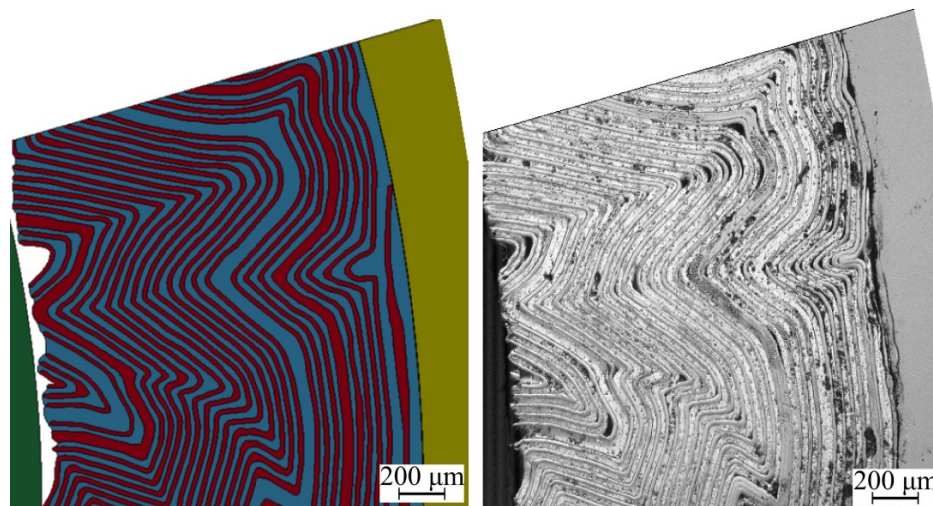
Figure 8.9 - The mesostructure used for the simulations (a) was extracted from an image of an area in SW-7A (b) that is characteristic of the experimental mesostructure. The red layers are aluminum, the blue layers are nickel, the yellow layer is the stainless steel jacket, and the green material is the copper inner stopper

tube. The outer copper driver tube and the explosive are not shown in this figure, but have dimensions that are consistent with the experiment.

Table 8.3 - Parameters for the Johnson-Cook constitutive model used in the simulations.

Material	P_0 [g cm^{-3}]	G [GPa]	A [MPa]	B [MPa]	n	c	m	T_m [K]
Al	2.77	26.2	84.21	426.0	0.34	0.015	1.0	773
Ni	8.902	74.45	297.2	648.1	0.33	0.006	1.44	1725
Cu	8.96	48.0	90.0	292.0	0.31	0.025	1.09	1356
SS 304	7.90	71.5	100.0	1072.0	0.34	0.005	1.0	1670

Table 8.4 - Parameters for the Grüneisen equation of state used in the simulations

Material	C [m s^{-1}]	S_1	S_2	S_3	γ_0	a
Al	5328	1.338	0.0	0.0	2.0	0.48
Ni	4650	1.445	0.0	0.0	1.93	0.50
Cu	3940	1.489	0.0	0.0	2.02	0.47
SS 304	4570	1.48	0.0	0.0	1.75	0.50

The modified nitromethane explosive was modeled with the Jones-Wilkins-Lee (JWL) equation of state (see Section 3.2) where the JWL constants $A = 78.69$ GPa, $B = 1.92$ GPa, $\omega = 0.36$, $R_1 = 4.61$, and $R_2 = 1.06$ ware obtained from calculations performed using Cheetah [44]. Since the velocity of collapse is significantly smaller than the detonation speed, we assume that the explosive in the plane of interest detonates instantaneously.

The maximum radial velocity of the interior surface of the Ni-Al laminate was 200-250 m/s. This shows that the strain rates in the sample were on the order of 10^4 s^{-1}, which is consistent with the strain rates observed in experiments using the TWC method [18] and is similar to the conditions in Taylor rod tests [25, 26]. The deformed geometry and the temperatures of the

simulated Ni-Al corrugated laminate at the moment of complete collapse are presented in Figure 8.10. The simulation captures the main features of plastic strain accommodation - wedge extrusion, trans-layer shear bands, and cooperative buckling (see Figure 8.10).

8.5 Discussion of results

Examination of the experimental specimens shown in Figure 8.2 and Figure 8.3 and the simulation results shown in Figure 8.10 and Figure 8.11 identified three major mechanisms of plastic strain accommodation – (1) the extrusion of interior facing wedge-shaped regions on the interior surface of the laminate, (2) local/global trans-layer shear bands mainly in areas where the layers were oriented in the radial direction, and (3) the cooperative buckling of layers in layers that were locally concentric. This behavior is dramatically different in comparison with plastic strain accommodation during dynamic deformation of coaxial Ni-Al layers in identical conditions of loading [19].

In the area where the layers on the interior of the sample are oriented more steeply towards the radial direction, a trans-layer shear band forms in numerical calculations. The detailed view of this shear band in Figure 8.11 (a) shows a reduction of the layer thickness inside the trans-layer shear band similar to the one observed in the experimental sample (Figure 8.11 (b)). In addition, the temperatures in the shear band in the simulation are greater than 550 K. In nano-sized Ni-Al laminates, reaction has been observed over a temperature range of 490 - 900 K [23, 24] and calculated temperatures in the simulated shear bands are inside this range. Thus, we may assume that reaction initiation inside the shear band was deformation induced.
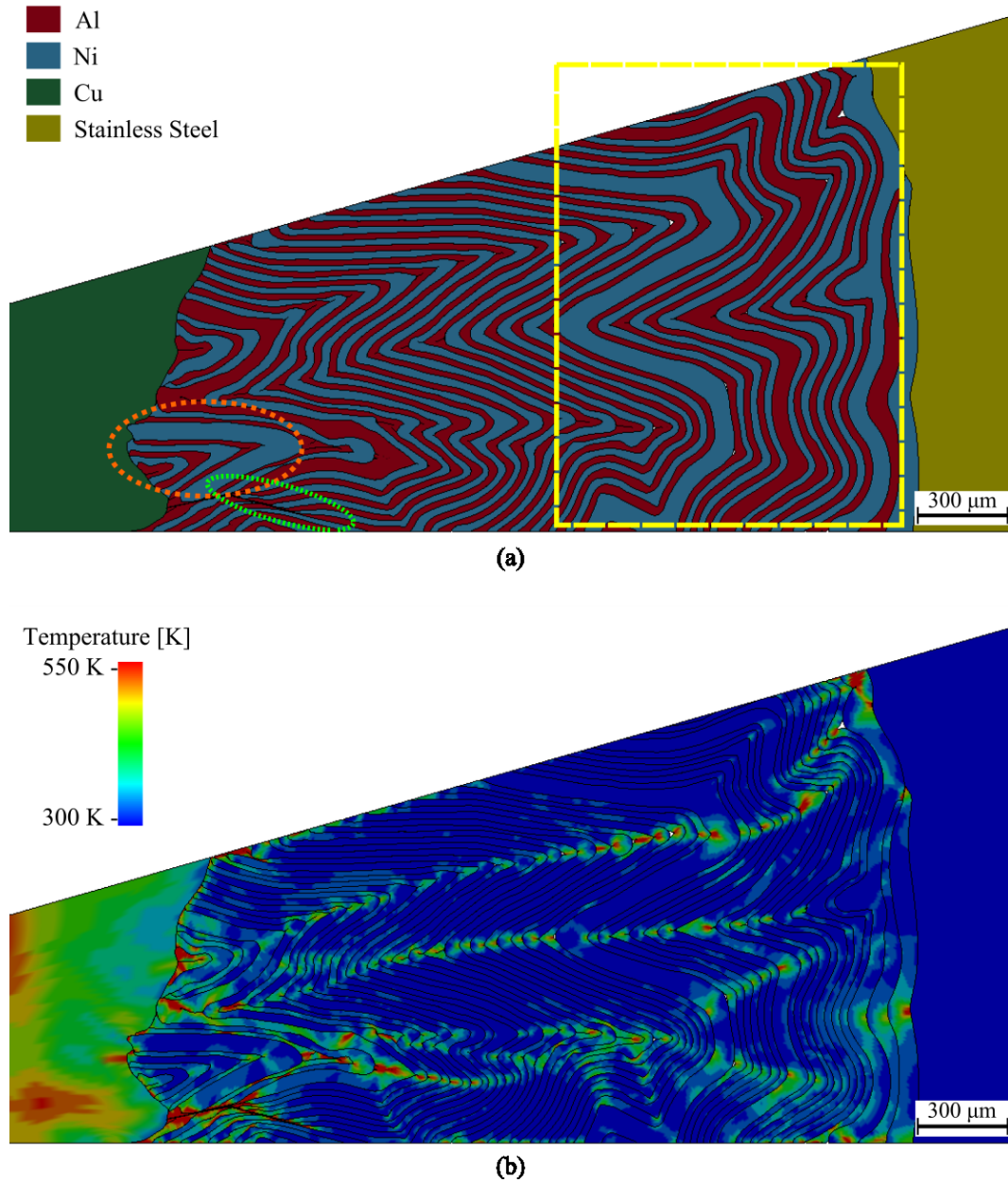
Figure 8.10 - The deformed mesostructure (a) showing the three major mechanisms of plastic strain accommodation: (1) the extrusion of wedged shaped regions outlined by the orange dashed line, (2) the development of trans-layer shear bands outlined by the green dashed line, and (3) the cooperative buckling shown in the area outlined by the yellow dashed box. The temperatures at the moment of complete collapse are shown in (b). Elevated temperatures were observed in the apex regions throughout the sample and in the shear band at the bottom of the figure.
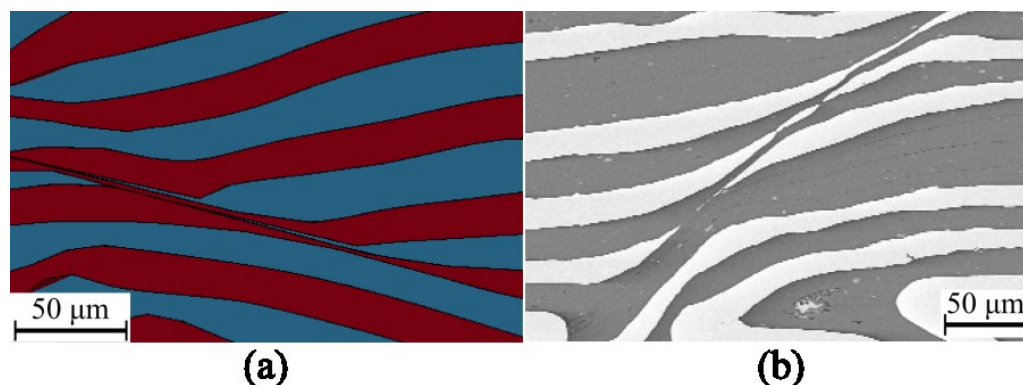
Figure 8.11 - Comparison of elongated Al and Ni layers observed inside the trans-layer shear bands in the numerical simulation (a) and the experimental result corresponding to sample SW-7A (b). This elongation process may be the initial stage in the initiation of reaction within the shear bands shown in Figure 8.3 and Figure 8.4 (b).

The development of the trans-layer shear bands was observed mainly in the exterior facing wedge-shaped regions or in areas where the layers were more parallel to the radius (Figure 8.3). Within the trans-layer shear bands, Ni and Al layers were elongated, reducing their thickness by an order of magnitude (from approximately 15-20 microns to 0.75-1.5 microns), creating localized, fine, micro-laminates. Additionally, in areas near the interior of the sample where the strains are large, some of these elongated layers fragment into sub-micron fragments. Both the elongation and fragmentation of the Ni and Al layers inside the shear bands provide favorable conditions for reactivity inside the shear bands. The thickness of the shear band is approximately 10 microns with a shear displacement of approximately 200 microns, thus the shear strain is about 20.

In addition to the local trans-layer shear bands, sample SW-6A contains a global shear band, defined as a shear band that traverses the entire width of the sample (Figure 3). In the global shear band, we do not observe any layer elongation or thinning. This global shear band radiates from the interior of the sample with an angle of ~45° with the radial direction. This

orientation is similar to the global shear bands observed in homogeneous and granular materials [9-18].

The simulations provided insight into the other details of the development of the plastic strain accommodation during the TWC tests. As the sample initially collapses, the porosity is squeezed from the sample and the gap between its inner surface and the copper stopper tube is closed. As the collapse progresses, the increase in the compressive hoop strains in the interior of the sample causes the wedge shaped regions, that are oriented at a slanted angle from the radial direction, to become extruded into the inner copper tube due to the slipping of the Ni-Al interfaces and also due to the localized plastic shearing of the Al in the slanted layers.

The extrusion of the interior facing wedges appears to be a unique mesoscale mechanism that accommodates plastic strain in these corrugated laminates. This mechanism of high strain plastic flow accommodation observed in the corrugated laminates is qualitatively analogous to the plastic flow of monocrystals [22, 23]. In both cases, the planes of easy slip were activated first, controlling the overall flow of the material. In the case of Al-Ni laminates these planes of easy slip were the Al layers and the Al-Ni interfaces that were at an angle to the radius at a 45^0 inclination, serving as the boundaries of the extruded wedges.

The temperatures observed in the simulations (Figure 8.10 (b)) showed that the layers in the interior wedges adjacent to the inner copper stopper tube had a temperature range of 320-500 K for the Ni, for the Al, and the maximum temperature on the outside surface of the copper stopper tube was 350-450 K. These deformation-induced temperatures due to radial collapse are small in comparison to the temperatures required for the initiation of intermetallic reactions in laminates with similar bi-layer thicknesses under static conditions, 500-900 K [4, 45]. As we mentioned above, one of the reasons for this localized reaction may be the interaction of Ni-Al laminates with the copper stopper interface during high strain, high strain rate plastic flow which is suggested by the presence of thin, reacted layers on this interface, as presented in Figure 8.5.

Simulations showed that in layers oriented nearly perpendicular to the radius (locally coaxial geometry), cooperative buckling appears to have been the prevalent mode of plastic strain accommodation, which was the dominant mode during the collapse of coaxial laminates [19]. This mode of deformation was difficult to characterize in the experimental samples due to the variation in the mesostructure in the axial direction, making it impossible to view the initial and corresponding final mesostructure at the same axial locations. However, we did observe some areas of locally coaxial layers in the initial mesostructures while we did not see any locally concentric areas in the collapsed mesostructures. Also, we observed that most of the apices in the collapsed sample were radially aligned similar to the radial alignment observed in the concentric samples [19] with no evidence of random buckling of individual layers. This suggests that the cooperative buckling mechanism was also active in the corrugated samples. The outer regions of the simulated segment of the laminate sample showed that the dominant mechanism of plastic strain accommodation was similar to the cooperative buckling observed in the concentric laminate composites [19]. The pattern of buckling was heavily influenced by the corrugated mesostructure on the interior of the sample. Like the samples with concentrically aligned layers, the buckles that were generated were nearly radial in nature. In addition, the apex areas of the buckles showed similar increases in localized temperature as in the concentric samples. However, the observed temperatures were less than those observed in the simulations with concentric layers of similar nominal size, probably due to additional mechanisms of plastic strain accommodation present in corrugated laminates.

8.6 Chapter conclusions

Explosively driven Thick Walled Cylinder experiments and their corresponding numerical simulations demonstrate that three main mechanisms of plastic strain accommodation triggered by instabilities, additionally to bulk distributed plastic flow, were active during the

collapse of the Ni-Al corrugated laminate composite – (1) the extrusion of interior facing wedge-shaped regions on the interior surface of the laminate, (2) a small number of non-uniformly distributed local/global trans-layer shear bands, and (3) the cooperative buckling of layers that were initially locally concentric. These mechanisms compete with each other in accommodation of high strain, high strain rate plastic flow and are dependent on the initial mesostructure of the corrugated samples. These mechanisms acted to block the development of multiple uniformly distributed global shear bands that have been observed in all previously examined solid homogeneous materials and granular materials. The observed mesoscale mechanisms of plastic strain accommodation in corrugated laminates are qualitatively different in comparison with behavior of Ni-Al laminates with coaxial symmetrical layers and showed a correlation with the orientation of layers relative to the sample's radius. Some of the local trans-layer shear bands showed reaction between the Ni and Al enhanced by dramatic elongation and fragmentation of Ni and Al layers and temperature increases due to deformation. A few of the extruded wedge-shaped regions demonstrated reaction between the Ni and Al layers, forming Ni-rich and Al-rich reaction products. The reaction inside extruded wedge-shaped regions with geometry of reaction products coinciding with the geometry of deformed wedges possibly enhanced by a high velocity metals/air jet moving in the gap between copper stopper tube and the sample. The reaction initiated in these spots did not ignite the bulk of material demonstrating that these mesostructured Ni-Al laminates are able to withstand high strain, high strain rate deformation without reaction. Thus the dynamic plastic deformation can be used as preconditioning making Ni-Al laminates more susceptible for subsequent bulk reaction initiated by shock.

This chapter contains material that appears in the Philosophical Magazine journal article K.L. Olney, P.H. Chiu, A. Higgins, M. Serge, T. P. Weihs, G. M. Fritz, A. K. Stover, D.J. Benson, and V.F. Nesterenko (2014) and is currently in press as of the writing of this dissertation. The dissertation author was an investigator and author of this paper.

8.7 Chapter references

[1] R. Ames, *MRS Symposia Proc.* **896**, 123 (2006).

[2] F.-X. Jette, S. Goroshin, D.L. Frost, A.J. Higgins and J.J. Lee, *Propellants, Explosives, Pyrotechnics* **37**, 345 (2012).

[3] T.E. Royal, S. Namjoshi, and N.N. Thadhani, *Metall. Mater. Trans. A* **27**, 1761 (1996).

[4] L. Battezzati, P. Pappalepore, F. Durbiano and I. Gallino, *Acta Mater.* **47**, 1901 (1999).

[5] J. Wang, E. Besnoin, A. Duckham, S.J. Spey, M.E. Reiss, O.M. Knio, M. Powers, M. Whitener, and T.P. Weihs, *Appl. Phys. Lett.* **83**, 3987 (2003).

[6] N.N. Thadhani, *Prog. in Mater. Sci.* **37**, 117 (1993).

[7] F. Zhang, R. Ripley and W. Wilson, *AIP Conf. Proc.* **1426**, 275 (2012).

[8] I. Song and N.N. Thadhani, *Metall. Trans. A* **23**, 41 (1992).

[9] V.F. Nesterenko, M.A. Meyers and H.C. Chen, *Acta Mater.* **44**, 2017 (1996).

[10] C.J. Shih, M.A. Meyers and V.F. Nesterenko, *Acta Mater.* **46**, 4037 (1998).

[11] H.D. Espinosa and B.A. Gailly, *Acta. Mater.* **49**, 4135 (2001).

[12] Y.J. Chen, M.A. Meyers and V.F. Nesterenko, *Mater. Sci. and Eng. A* **268**, 70 (1999).

[13] Q. Xue, V.F. Nesterenko and M.A. Meyers, *Int. J. Impact Eng.* **28**, 257 (2003).

[14] Z. Lovinger, A. Rikanati, Z. Rosenberg and D. Rittel, *Int. J. Impact Eng.* **38**, 918 (2011).

[15] V.F. Nesterenko, M.A. Meyers, H.C. Chen and J.C. Lasalvia, *Appl. Phys. Lett.* **65**, 3069 (1994).

[16] V.F. Nesterenko, M.A. Meyers, H.C. Chen and J.C. Lasalvia, *Metall. Mater. Trans. A* **26**, 2511 (1995).

[17] H.C. Chen, V.F. Nesterenko, and M.A. Meyers, *J. Appl. Phys.* **84**, 3098 (1998).

[18] V.F. Nesterenko, *Dynamics of Heterogeneous Materials, 1st ed.,* Springer, New York, 2001.

[19] P.H. Chiu, K.L. Olney, A. Higgins, M. Sege, D.J. Benson and V.F. Neterenko, *Appl. Phys. Lett.* **102**, 241912 (2013).

[20] E.P. Degarmo, J.T. Black and R.A. Kohser, *Materials and Processes in Manufacturing, 9th ed.,* Wiley Hobokin, 2003.

[21] S. Nemat-Nasser, T. Okinaka and V.F. Nesterenko, *Mater. Sci. and Eng. A* **249**, 22 (1998).

[22] S. Nemat-Nasser, T. Okinaka, V.F. Nesterenko and M. Liu, *Philos. Mag.* **78**, 1151 (1998).

[23] E. Ma, C.V. Thompson and L.A. Clevenger, *J. Appl. Phys.* **69**, 2211 (1991).

[24] G.M. Fritz, S.J. Spey, M.D. Grapes and T.P. Weihs, *J. Appl. Phys.* **113**, 014901 (2013).

[25] A.C. Whiffin, *Proc. Roy. Soc. London A* **194**, 300 (1948).

[26] G.I. Taylor, *Proc. Roy. Soc. London A*, **194**, 289 (1948).

[27] L. Battezzati, P. Pappalepore, F. Durbiano and I. Gallino, *Acta Mater.* **47**, 1901 (1999).

[28] A.S. Edelstein, R.K. Everet, G.Y. Richardson, S.B. Qadri, E.I. Altman, J.C. Foley and J.H. Perepezko, *J. Appl. Phys.* **76**, 7850 (1994).

[29] K. Barmak, C. Michaelsen and G. Lucadamo, *J. Mater. Res.* **12**, 133 (1997).

[30] H. Sieber, J.S. Park, J. Weissmuller and J.H. Perepezko, *Acta Mater.* **49**, 1139 (2001).

[31] X. Qiu and J. Wang, *Scripta Mater.* **56**, 1055 (2007).

[32] C.T. Wei, V.F. Nesterenko, T.P. Weihs, B.A. Remington, H.S. Park and M.A. Meyers, *Acta Mater.* **60**, 3929 (2012).

[33] C. Michaelsen, G. Lucadamo and K. Barmak, *J. Appl. Phys.* **80**, 6689 (1996).

[34] C.T. Wei, B.R. Maddox, A.K. Stover, T.P. Weihs, V.F. Nesterenko and M.A. Meyers, *Acta Mater.* **59**, 5276 (2001).

[35] K.J. Blobaum, D. Van Heerden, A.J. Gavens and T.P. Weihs, *Acta Mater.* **51**, 3871 (2003).

[36] M.H.D. Bassani, J.H. Perepezko, A.S. Edelstein and R.K. Everett, *Scripta Mater.* **37**, 227 (1997).

[37] I. Song and N.N. Thadhani, *Metall. Trans. A* **23**, 41 (1992).

[38] O. Arkens, L. Delaey, J. De Tavernier, B. Huybrechts, L. Buekenhout and J.C. Libouton, *MRS Proc.* **133**, 493 (1988).

[39] Livermore Software Technology Corperation, *LS-DYNA User's Manual, Volume I Revison 7* Livermore Software Technology Corperation, Livermore, 2013.

[40] J. W. Eaton, D. Bateman and S. Hauberg, *GNU Octave version 3.0.1 manual: a high-level interactive language for numerical computations*, CreateSpace Independent Publishing Platform, 2009.

[41] G.R. Johnson and W.H. Cook, *Eng. Fract. Mech.* **21**, 31 (1985).

[42] D.J. Steinberg, Equations of states and strength properties of selected materials, Report UCRL-MA-106439, Livermore, CA: Lawrence Livermore National Lab: 1996.

[43] E. Vitali, C.T. Wei, D.J. Benson and M.A. Meyers, *Acta. Mater.* **59**, 5869 (2011).

[44] L.F. Fried and P.C. Souers, *CHEETAH 2.0 User's Manual* Lawrence Livermore National Laboratory, Livermore, 1998.

[45] F. Cardellini, G. Mazzone, A. Montone and M.V. Antisari, *Acta Metall. Mater.* **42**, 2445 (1994).

Chapter 9

Conclusions

Numerical simulations of dynamic behavior of heterogeneous Al-W granular and Al-Ni laminate materials were conducted for three different experimental testing environments; the drop weight test, the explosively driven expanding ring, and the thick walled cylinder. These experiments and simulations revealed the mechanisms of plastic strain accommodation and post critical behavior experienced by these heterogeneous materials with mesostructures that are characteristic of other reactive material systems.

The drop weight experiments and simulations of the Al-W granular material revealed that the main mechanism of plastic strain accommodation was primarily influenced by (a) the degree of bonding between the Al determined by the processing and (b) the geometry of the mesotrucutre (i.e. particle size and arrangement). It was shown that in simulated CIPed only (non-bonded) samples, the Al and W particles rearranged themselves during the dynamic deformation to effectively block shear localization. This resulted in the subsequent bulk disintegration of the sample in agreement with areas near the outer surface of the samples used in the experiments. The CIPed+HIPed (bonded) samples exhibited shear localization and subsequent shear band formation. The shear bands nucleated during the initial stages of the deformation in Al surrounding the W particles and spread to the nearby W particles at angles close to 45 degrees. The shear band is kinked by W particles causing the shear band path to deviate from the ideal 45 degree angle path dictated by global geometry. In simulations with relatively larger W particles, the path of the shear band was influenced to a greater degree than simulations with the similar sized W and Al particles due to increased heterogeneity of the sample. It was also shown that

variations in the initial arrangements of the W particles were the main drivers determining where the global shear bands formed in the sample. Numerical calculations and experiments revealed that the mechanism of shear localization in granular composites is due to a localized high strain flow of Al around rigid W particles, causing local damage accumulation and a subsequent growth of the meso/macro shear bands/cracks.

Explosively driven fragmentation experiments of Al-W porous/granular composite rings showed that the samples were mostly pulverized into fragments sizes below 100 micron (above 90%) for all tested mesostructures. A comparison of initial sizes of particles in the powder and post experiment fragment size distributions indicates that some of the low strength Al particles were deformed between the rigid W particles, but mainly maintained their equiaxed shape in the areas away from W particles. Numerical simulations were performed of these experiments with an artificial mesostructure generated from a Voronoi tessellation procedure. The simulations showed good agreement with the final free surface measurements. Qualitative similarities between the simulations and experiments were observed. The simulations revealed that the creation and development of numerous sheared zones in granular Al matrix may allow fracture of initial Al particles and the generation of micron-sized Al fragments inside them. The spacing between these sheared zones is much larger than the size of the Al and W particles suggesting that material between them is shielded from mesoscale pulverization resulting in the generation of the large scale fragments of agglomerated Al and W particles.

Numerical simulations of Al-W granular composite rings under various dynamic loading conditions due to explosive loading were performed. Three competing mechanisms of fragmentation were observed: a continuum level mechanism generating macrocracks with a size scale comparable to the case width, a mesoscale mechanism generating voids and microcracks at the non-bonded Al/W interfaces due to tensile strains, and mesoscale jetting due to the development of large velocity gradients between the W particles and surrounding Al. These

mesoscale mechanisms may be used to tailor the size of the fragments (macro to mesoscale) by selecting an appropriate initial mesostructure for a given loading condition.

The TWC experiments and simulations of dynamic collapse of Ni-Al concentric laminate cylinders demonstrated a new phenomenon of the cooperative buckling originating in the innermost layers. The instability of all layers is dictated by the buckling mode of the inner layers. The laminate geometry resulted in the cooperative buckling of layers which is different from independent buckling of single thin walled cylinders. The investigated non-bonded laminate mesostructure blocked the development of localized shear bands, the major mechanism of large plastic strain accommodation observed in homogeneous materials under similar conditions. This buckling mechanism supported numerous localized reaction zones in the areas near the apices, but global ignition was not observed.

In the TWC experiments and simulations of the corrugated Ni-Al laminates, three main mechanisms of plastic strain accommodation triggered by instabilities were active during the collapse of the Ni-Al corrugated laminate composite; (1) the extrusion of interior facing wedge-shaped regions on the interior surface of the laminate, (2) a small number of non-uniformly distributed local/global trans-layer shear bands, and (3) the cooperative buckling of layers that were initially locally concentric. These mechanisms compete with each other in accommodation of high strain, high strain rate plastic flow and are dependent on the initial mesostructure of the corrugated samples. These mechanisms acted to block the development of multiple uniformly distributed global shear bands that have been observed in all previously examined solid homogeneous materials and granular materials. The observed mesoscale mechanisms of plastic strain accommodation in corrugated laminates are qualitatively different in comparison with behavior of Ni-Al laminates with coaxial symmetrical layers and showed a correlation with the orientation of layers relative to the sample's radius. Some of the local trans-layer shear bands showed reaction between the Ni and Al enhanced by dramatic elongation and fragmentation of Ni

and Al layers and temperature increases due to deformation. A few of the extruded wedge-shaped regions demonstrated reaction between the Ni and Al layers, forming Ni-rich and Al-rich reaction products. The reaction inside extruded wedge-shaped regions with geometry of reaction products coinciding with the geometry of deformed wedges possibly enhanced by a high velocity metals/air jet moving in the gap between copper stopper tube and the sample. The reaction initiated in these spots did not ignite the bulk of material demonstrating that these mesostructured Ni-Al laminates are able to withstand high strain, high strain rate deformation without reaction.